YAP engages RIF1 to dampen replication stress in squamous cell carcinoma.

Jodie Bojko[1], Benjamin Flynn[1,2,3], Alexander Howard[1], Bertram Aschenbrenner[4], Emily Lay[1], Natalia Krajic[4], Emma Bailey[3,5], Sandra Catalan[1], Kelli Gallacher[1], Elodie Sins[2,3], Jun Wang[3,5], Ute Jungwirth[1,6], Beate M. Lichtenberger[4], Gernot Walko[1,2,3,*]

[1]Department of Life Sciences, University of Bath, Bath, UK.

[2]Centre for Oral Immunobiology and Regenerative Medicine, Institute of Dentistry, Queen Mary University of London, London, UK.

[3]Barts Centre for Squamous Cancer, Institute of Dentistry, Queen Mary University of London, London, UK.

[4]Department of Dermatology, Medical University of Vienna, Vienna, Austria.

[5]Barts Cancer Institute, Queen Mary University of London, London, UK.

[6]Cancer Research Horizons Therapeutic Innovation, Newcastle Drug Discovery Group, Translational and Clinical Research Institute, Newcastle University, Newcastle, UK.

Abstract

Squamous cancers are the most frequently diagnosed solid tumours world-wide. The closely related transcriptional co-regulators YAP and TAZ (WWTR1) have emerged as important drivers of tumour initiation and progression in various types of squamous cell carcinoma. How YAP and TAZ execute their oncogenic functions in squamous cancers is still not fully understood. Here, we report that in addition to controlling transcriptional programmes that determine the balance between proliferation and terminal differentiation, YAP also engages with RIF1, a key regulator of DNA replication timing and protector of stalled replication forks under replication stress. YAP modulates gene expression of RIF1 via TEAD transcription factors, and also stabilizes RIF1 protein on the chromatin. YAP-RIF1 complex formation increases in response to exogenous replication stress, and treatment with hydroxyurea to induce replication fork stalling acts synergistically with YAP depletion to impair cell proliferation. Our results thus demonstrate that YAP's oncogenic functions in squamous cell carcinoma involve both transcriptional and non-transcriptional mechanisms, and that RIF1 is key for squamous cell carcinoma cells to survive with their high levels of endogenous replication stress.

Introduction

Squamous cancers develop in squamous (also called 'stratified') epithelia and are by far the most frequently diagnosed solid tumours globally, with incidences continuing to rise (1). Common risk factors for developing squamous cell carcinoma (SCC) are smoking, alcohol, and viral infections (human papilloma virus and Epstein-Barr virus)(1). SCC of the skin epidermis (cutaneous SCC; cSCC) is the most common type of squamous cancer, and a significant burden to health care systems world-wide due to its very high incidence (2). The major risk factor for cSCC development is life-long chronic exposure to UV radiation in sunlight (1, 2). In contrast,

46 SCCs originating in the head and neck region (HNSCC), which include squamous cancers of the
47 oral cavity, oropharynx, nasopharynx, hypopharynx, and larynx, are less common, but are
48 associated with a far higher mortality rate (3). This is due to their aggressiveness and high risk
49 of progression to metastatic disease (3). There is ample evidence that the cells of origin of
50 SCCs are the stem and progenitor cells which are located in the deepest tissue layers and
51 maintain and repair squamous epithelia during the life course (4). Tissue homeostasis of the
52 highly proliferative squamous epithelial tissues is maintained by a tightly controlled balance
53 of cell proliferation and terminal differentiation (5). Proliferating cells that have committed to
54 undergoing terminal differentiation withdraw from the cell cycle and undergo a programmed
55 series of biochemical and morphological changes whilst moving towards the epithelial surface
56 (6). In well differentiated SCCs the terminal differentiation programme continues to be
57 executed to some extent, often giving rise to regions with concentric layers of differentiated
58 cancer cells called 'keratin pearls' (1, 7). It is widely understood that the ability of SCC cells to
59 undergo terminal differentiation acts as a 'brake' to tumour progression (1-3). Accordingly, in
60 poorly differentiated SCCs the cancer cells have lost the ability to undergo terminal
61 differentiation, which contributes to the rapid growth and increased aggressiveness of such
62 tumours (2, 3). Lung squamous cell carcinoma (LUSC) is a form of non-small cell lung cancer,
63 and contrary to other types of SCC, develops through acquisition of a squamous differentiation
64 programme of the basal stem/progenitor cells in the otherwise pseudo-stratified epithelium
65 covering the trachea and the airways, or by trans-differentiation of a lung adenocarcinoma
66 into a LUSC (8, 9).

67 Like other cancers, SCC arises from genetic alterations that invariably lead to dysregulated
68 transcriptional programmes (1-3, 10). These dysregulated programmes can cause cancer cells
69 to become highly dependent on certain regulators of gene expression (11). Such

70 transcriptional dependencies are not typically identified by cancer genome sequencing but
71 arise through focused mechanistic studies of gene control programmes operating in both
72 normal and neoplastic cells (11). The closely related transcriptional co-regulators Yes-
73 associated protein (YAP; gene symbol: *YAP1*) and transcriptional co-activator with PDZ-
74 binding motif (TAZ, also called WW Domain Containing Transcription Regulator 1 (*WWTR1*))
75 have surfaced as essential drivers of cancer initiation, progression and metastasis in many
76 tumour types, including SCC (12-15). YAP/TAZ do not bind DNA directly, but rely on the
77 interaction with different transcription factors (TFs; predominantly those of the TEAD family
78 (12, 13, 16)) and associated cofactors (e.g. bromodomain-containing protein 4 (BRD4) (17)
79 and the BRG1- or BRM-associated factors (BAF)-type SWItch/Sucrose Non-Fermentable
80 (SWI/SNF) chromatin regulation complex (18)) to bind to enhancer and super-enhancer
81 elements (large chromatin domains bountiful in cell-type specific TF binding motifs that
82 enable cooperative binding of TFs) to drive the execution of transcriptional programmes that
83 promote proliferation, chemoresistance, epithelial-to-mesenchymal transition (EMT), and
84 metastasis (12, 13, 19). YAP/TAZ can operate as both transcriptional co-activators and co-
85 repressors (20). Although YAP/TAZ are classified as oncoproteins (http://ongene.bioinfo-
86 minzhao.org/browse_gene.html), activating mutations of YAP/TAZ are rarely identified (21).
87 Instead, activation of YAP/TAZ occurs through de-regulation of upstream inhibitory signalling
88 pathways, leading to increased nuclear YAP/TAZ accumulation and consequently, chromatin
89 binding and downstream signalling (12, 13, 16, 19). In addition to the well documented
90 transcriptional functions of YAP/TAZ, evidence for non-transcriptional roles has also begun to
91 emerge (22, 23). Intriguingly, a recent study demonstrated that YAP regulates DNA replication
92 during early stages of *Xenopus* development, when transcription is still largely absent (24).
93 Studies in mice have demonstrated an absolute requirement of YAP/TAZ for initiation and

94 progression of both cSCC and HNSCC (25-28), while YAP/TAZ appear to be largely dispensable
95 for normal squamous epithelial tissue homeostasis (26, 28, 29). This highlights the possibility
96 that targeting YAP/TAZ in SCC may display a large therapeutic window (14, 15).

97 One of the hallmarks of cancer cells is their ability to sustain chronic proliferation (30). Since
98 oncogene expression drives cancer cell proliferation by interfering with the regulatory
99 pathways of cell cycle progression control, cancer cells usually experience replication stress,
100 which occurs when DNA replication fork progression in S phase slows or stalls (31, 32). This
101 leads to the collapse of forks into DNA double-strand breaks (DSBs), as well as incomplete
102 sister chromatid separation in the following mitosis, and ultimately genomic instability (31,
103 32). In addition to de-regulated cell cycle control, another source of replication stress is the
104 upregulation of transcription, which can cause direct collisions or torsional stress between the
105 transcriptional and replication machineries as well as collisions with RNA-DNA hybrids (R
106 loops) (32, 33). As endogenous replication stress is higher in cancer cells, they depend on
107 replication stress response and DNA damage response (DDR) pathways for survival (31, 34,
108 35). Markers of endogenous replication stress have been found in tumour samples and cells
109 expressing active oncogenes (36-38). Of note, the stem and progenitor cells in healthy human
110 epidermis already have high levels of endogenous replication stress due to their high
111 proliferation rates, and the resulting activation of DDR pathways directly couples replication
112 stress to polyploidisation and terminal differentiation as a homeostatic mechanism (39, 40).
113 This mechanism is mediated by G2 and mitotic checkpoints that determine the fate of
114 epidermal stem/progenitor cells towards differentiation or apoptosis (41-43). Importantly, the
115 same mechanism operates to eliminate pre-cancerous cells in the epidermis in response to
116 activation of oncogenic signalling (‘oncogene-induced differentiation’; (44)), such as

117 overexpression of MYC or Cyclin E (*CCNE1*) (42, 45), or inactivation of TP53 (43). The key cell
118 cycle regulator p21 (*CDKN1A*) is a transcriptional target of TP53, but squamous epithelial cells
119 (keratinocytes) also express a pool of p21 that is regulated in a TP53-independent fashion (41,
120 43). Interestingly, depletion of this TP53-independent pool of p21 was shown to alleviate the
121 differentiation response caused by knockdown of TP53, allowing DNA-damaged keratinocytes
122 to escape differentiation and continue to proliferate (41). Intriguingly, several studies have
123 reported that reduced p21 expression inversely correlates with cell proliferation and invasion
124 in HNSCC patient samples (46, 47), suggesting that suppression of p21 may be an important
125 step in human SCC progression similar to what was reported in mice (48). While YAP plays an
126 essential role in stimulating proliferation of human epidermal stem cells in response to tissue
127 injury (49, 50), overexpression of an oncogenic, hyperactive YAP variant in these cells was
128 found to induce rapid senescence (50). It is likely that this oncogene-induced senescence
129 mechanism is linked to YAP-driven transcription and the resulting replication stress, similar to
130 what was reported in neuronal progenitors upon YAP/TAZ activation (51).

131 How YAP/TAZ control oncogenic signalling in SCC at the molecular level, and how SCC cells
132 deal with YAP/TAZ hyperactivation-induced replication stress remains poorly understood.
133 Here, by characterising the YAP-controlled transcriptome and the protein interactome of
134 chromatin-associated YAP, we have identified transcriptional and non-transcriptional
135 mechanisms that underly YAP's oncogenic functions in SCC, including engagement of the DNA
136 replication and damage repair factor RIF1 to dampen replication stress.

137

138 **Results**

139 ***The protein interactome of chromatin-associated YAP in squamous cell carcinoma cells.***

140 To characterise the protein interactome of transcriptionally engaged, chromatin-associated
141 YAP in SCC cells, we chose SCC13 as a relevant cell model. SCC13 cells are a widely used human
142 cSCC cell line and are derived from the rapid recurrence of a cSCC (T2N0) in a patient's facial
143 epidermis following radiotherapy (52, 53). As is typical for cSCC, SCC13 cells carry an
144 inactivating mutation in *TP53* (p.Glu258Lys (c.772G>A) (54, 55). SCC13 are representative of a
145 subclass of cSCC with reduced expression of αE-catenin (49, 56), which likely explains the
146 constitutive nuclear localisation of YAP/TAZ in these cells and their strong YAP-dependency
147 (49). Like most cSCC cell lines, SCC13 require feeder layer support for optimal growth in culture
148 (52, 57).

149 Rapid immunoprecipitation mass spectrometry of endogenous protein (RIME) analysis (58)
150 was performed on two independent cultures of SCC13 cells and normal human epidermal
151 keratinocytes (NHK, strain Km), using a knockdown-validated YAP-specific antibody that does
152 not recognise TAZ (Supplementary Figs. 1A and 2D) and isotype-matched IgG as control. Low
153 passage cells were cultured on a mitotically inactivated fibroblast feeder layer to maintain the
154 stem cell state of NHKs characterised by predominantly nuclear localisation of YAP
155 (Supplementary Fig. 1B) (49, 59). YAP immunoprecipitation (IP) was performed on
156 formaldehyde-fixed chromatin fractions of SCC13 and NHK cells. IP efficiency was consistently
157 high across all YAP-RIME replicates, with high YAP peptide coverage (63-65%) detected by
158 mass spectrometry analysis (Supplementary Fig. 1C), and with zero spectral counts (MS/MS
159 events, total number of spectra associated to a single protein or protein group) for YAP in the
160 IgG-control IPs (Supplementary Dataset 1). Proteins detected by mass spectrometry in the YAP
161 IPs (Supplementary Dataset 1 – Table 1) were stringently filtered (see Materials and Methods,
162 and Supplementary Dataset 1 – Tables 2–7) to remove potential false positive hits and to
163 compile a list of high confidence interactors of chromatin-associated YAP in SCC13 and NHK

164 cells (Supplementary Dataset 1 – Tables 6, 7). YAP-RIME enabled identification of 48 high
165 confidence YAP-interacting proteins in SCC13 cells (Fig. 1A, Supplementary Dataset 1 – Table
166 6) and 15 high confidence YAP-interacting proteins in NHK cells (including the bait protein YAP
167 in both cases) (Supplementary Fig. 2A, Supplementary Dataset 1 – Table 7). Using the
168 'Compartments' database (https://compartments.jensenlab.org/Search), most identified
169 proteins had a high confidence score (≥4) for nuclear localization (Supplementary Dataset 1 –
170 Tables 6, 7). Moreover, significantly enriched gene ontology terms for molecular functions
171 (GO MF) and biological processes (GO BP) in both protein interactomes were all related to
172 processes occurring in the nucleus (Fig. 1B, Supplementary Fig. 2B). This confirms that, as
173 expected, the YAP-RIME predominantly identified protein interactions of YAP on the
174 chromatin.

175 STRING analysis was used to identify known interactions occurring between the YAP-
176 interacting proteins in SCC13 (Fig. 1A) and NHK (Supplementary Fig. 2A) cells, and proteins
177 were manually grouped by cellular function (60). Because our aim was to identify proteins
178 that facilitate YAP's functions in squamous cancers, we focused on the protein interactome of
179 chromatin-associated YAP in SCC13 cells. Among these YAP-interacting proteins were several
180 known regulators of YAP, including Neurofibromatosis type (NF2, also called Merlin) (61),
181 Angiomiotin-like 1 (AMOTL1), PPP1CB, one the catalytic subunits of protein phosphatase 1
182 (PP1) (62), and Prolyl 4-Hydroxylase subunit alpha 2 (P4HA2). The identification of NF2 in the
183 interactome of chromatin-bound YAP was, at first look, at odds with the established dogma
184 that the canonical Hippo signalling pathway operates in the cytoplasm. However, nuclear
185 localization of NF2 has been widely documented (63), and nucleocytoplasmic shuttling of NF2
186 has been implicated in YAP regulation (64-66). AMOTL1, a member of the Motin protein family
187 (67), was previously shown to enhance YAP stability and to help translocate YAP into the

188 nucleus (68, 69). P4HA2 was shown to hydroxylate YAP at multiple proline residues, with
189 implications in cell migration and invasion (70). Consistent with the results from a previous
190 study which used a similar YAP chromatin-IP/mass spectrometry approach (71), our YAP-RIME
191 also identified five subunits of the BAF-type SWI/SNF chromatin remodelling complex (72) in
192 the interactome of chromatin-associated YAP in SCC13 cells. These included the YAP binding
193 partner AT-rich interactive domain-containing protein 1A (ARID1A), and SWI/SNF-related
194 matrix-associated actin-dependent regulator of chromatin (SMARC) subfamily A member 4
195 (SMARCA4, also called BRG1), subfamily E member 1 (SMARCE1), subfamily D member 2
196 (SMARCD2), and subfamily C member 1 (SMARCC1) (Fig. 1A). Two key components of the
197 NuRD chromatin remodelling complex, Chromodomain-helicase-DNA-binding protein 4
198 (CHD4) and Metastasis Associated 1 Family Member 2 (MTA2), were also identified as
199 interactors of chromatin-bound YAP in SCC13 cells. Of note, the NuRD complex was previously
200 implicated in mediating co-repressor functions of YAP (73). While key components of the
201 general transcriptional machinery (POLR2A, POLR2B, GTF21, TOP1) were present in the SCC13
202 YAP interactome, TEAD TFs were notably absent (Fig. 1A). A closer inspection of our mass
203 spectrometry data revealed that TEADs, as well as other known YAP-interacting transcription
204 factors, such as JunB and TP63 (74, 75), had been identified but did not pass our stringent
205 bioinformatics filtering criteria (Supplementary Dataset 1 – Table 4). The overall poor
206 identification of TFs by our YAP-RIME was likely due to their insufficient crosslinking to the
207 DNA by formaldehyde alone, as previously observed for the highly dynamic transcription
208 factor NFκB (76).

209 To identify physiologically relevant interactions, the YAP-interacting proteins identified by
210 RIME in SCC13 were also compared to candidate positive and negative regulators of cell
211 proliferation and survival identified in a genome-wide RNA interference screen that had

212 previously been performed in the same cell lines (49). This revealed that 22 out of the 47 high
213 confidence YAP-interacting proteins in SCC13 cells were likely relevant for cell proliferation
214 and/or survival (Fig. 1A, Supplementary Dataset 1 – Table 8).
215
216 ***A fraction of chromatin-associated YAP interacts with RIF1.***

217 Our attention was drawn to RIF1, a key regulator of DNA replication timing and DDR (77-85).
218 An involvement of RIF1 in transcription regulation has been reported previously (86, 87). RIF1
219 was detected as a YAP-interacting protein in both the SCC13 and NHK YAP-RIME experiments
220 (Fig. 1A; Supplementary Fig. 2A) with a much stronger enrichment in the SCC13 cells
221 (Supplementary Fig. 2C, Supplementary Dataset 1 – Tables 6, 7). Of note, PPP1CB, one of the
222 three catalytic subunits of PP1—a key effector of RIF1 (77, 81, 84, 85), was also present in the
223 SCC13 YAP-RIME (Fig. 1A; Supplementary Dataset 1 – Table 6). Like YAP, RIF1 featured among
224 the positive regulators of cell proliferation and survival of SCC13 cells identified in a genome-
225 wide RNA interference screen (49)(Fig. 1A; Supplementary Dataset 1 – Table 8). As expected,
226 YAP and RIF1 were both localised in the nucleus of SCC13 cells (Fig. 1C) and were present in
227 chromatin fractions (Supplementary Fig. 2D), confirming their chromatin-association. To
228 biochemically validate the YAP-RIF1 interaction identified by RIME, co-IP experiments were
229 performed under native non-cross-linking conditions using a different YAP-specific antibody
230 that also does not detect TAZ (Supplementary Fig. 3A). Indeed, RIF1 could be
231 immunoprecipitated together with YAP from both, whole-cell detergent extracts and nuclei-
232 enriched fractions (Fig. 1D, E). Further validating our RIME results, CHD4 and ARID1A also co-
233 immunoprecipitated with YAP under native conditions. We also found that under these
234 conditions, TEAD transcription factors could be immunoprecipitated together with YAP (Fig.
235 1E). Of note, compared to the TEADs, smaller amounts of RIF1, ARID1A, and CHD4 co-

236 immunoprecipitated with YAP from nuclei-enriched fractions, possibly indicating weaker
237 interactions of these proteins with YAP. Indeed, significantly more RIF1 co-
238 immunoprecipitated with YAP under milder lysis conditions (Fig. 1D). In-situ proximity ligation
239 assays (PLA) confirmed YAP-RIF1 interactions in the nucleus of SCC13 cells (Fig. 1F). The YAP-
240 RIF1 PLA signal was significantly decreased upon YAP/TAZ knockdown. To achieve a sufficient
241 knockdown of both YAP and TAZ we combined our doxycycline-inducible YAP-targeting shRNAs
242 with an siRNA pool targeting YAP and TAZ (Fig. 1F, Supplementary Fig. 3B). Consistent with our
243 co-IP results, YAP was also found in very close proximity to TEAD1 in the nucleus of SCC13 cells
244 by PLA (Fig. 1G). The YAP-RIF1 PLA signal was completely absent when either both or one of
245 the two primary antibodies were omitted during the experiments (Supplementary Fig. 3C, D),
246 and was also largely absent from mitotic chromosomes (Supplementary Fig. 3E). To test if the
247 YAP-RIF1 interaction also occurred in other types of SCC, we used the lung SCC cell line HARA
248 (88). YAP and RIF1 co-expression in HARA cell nuclei was confirmed by immunofluorescence
249 microscopy (Supplementary Fig. 3F). Co-IP was performed with nuclei-enriched HARA cell
250 fractions treated with Benzonase nuclease to enzymatically digest DNA and RNA
251 (Supplementary Fig. 3G, H), demonstrating that YAP and RIF1 interact on the chromatin and
252 are not co-immunoprecipitated because of a DNA bridge between the two proteins. In
253 summary, our results show that RIF1 is a binding partner of chromatin-associated YAP in NHKs
254 and cutaneous and lung SCC cells.
255
256 ***YAP/TAZ-mediated oncogenic signalling controls the balance between proliferation and***
257 ***differentiation and contributes to replication stress in squamous cell carcinoma cells.***
258 In normal epidermal keratinocytes, but also in basal cell carcinoma (BCC) cells, YAP/TAZ control
259 the transcription of genes driving cell proliferation and survival through TEAD transcription

260 factors and suppress the expression of genes promoting terminal differentiation through
261 TEAD-independent mechanisms (89, 90). To test if YAP/TAZ execute similar transcriptional
262 programmes in cSCC, and to investigate a potential involvement of RIF1 in YAP/TAZ-mediated
263 transcriptional regulation, we performed bulk RNAseq analysis on samples of SCC13 cells with
264 acute (48 hours) siRNA-mediated knockdown of either YAP/TAZ or RIF1 (siY/T, siRIF1; Fig. 2A,
265 Fig. 3A). We were unable to robustly deplete TAZ(WWTR1) (Fig. 2A), but the TAZ-targeting
266 siRNA pool was able to block compensatory upregulation of TAZ in response to YAP
267 knockdown (Supplementary Fig. 3B) (49). DESeq2 analysis revealed a large number of
268 differentially expressed genes (DEGs) upon siY/T treatment (977 DEGs downregulated, 2,209
269 DEGs upregulated; $p<0.05$, FC>1.5; Supplementary Dataset 2 - Tables 1–3). Gene set
270 enrichment analysis (GSEA) revealed significant enrichment of pathways associated with cell
271 cycle regulation, DNA replication, and mitosis among the downregulated DEGs, and of
272 pathways associated with keratinization, cornification, extracellular matrix (ECM) remodelling,
273 and immunoregulation among the upregulated DEGs upon siY/T treatment (Fig. 2C;
274 Supplementary Fig. 4A, B; Supplementary Dataset 2 - Tables 4–6). DEGs downregulated upon
275 siY/T comprised both, genes known to be positively regulated by YAP/TAZ in cooperation with
276 TEADs (26), as well as genes known to be regulated by YAP/TAZ in cooperation with the Myb-
277 MuB (MMB) complex (91, 92) (Supplementary Fig. 4C; Supplementary Dataset 2 – Tables 10,
278 11). YAP/TAZ knockdown in SCC13 also led to increased terminal differentiation which was
279 evident from (i) enrichment of an epidermal terminal differentiation gene signature (93) in
280 the upregulated DEGs and of an epidermal progenitor cell signature (93) in the downregulated
281 DEGs (Supplementary Fig. 4D), and (ii), upregulation of genes belonging to the epidermal
282 differentiation complex (EDC) (94), as well as transcriptional regulators of terminal
283 differentiation (Fig. 2C; Supplementary Dataset 2 – Tables 13, 14). These data suggest that

284 YAP/TAZ regulate terminal differentiation indirectly by supressing the transcription of key
285 regulators of the terminal differentiation programme, and that this function is conserved
286 between normal keratinocytes and neoplastic keratinocytes of both BCC (90) and cSCC. In
287 accordance with the detected transcriptomic changes, we observed that cell proliferation was
288 impacted in SCC13 cells upon expression of doxycycline-inducible YAP-targeting shRNAs
289 (shYAP) (Fig. 2C). This was evident from reduced levels of Ser10-phosphorylated histone H3, a
290 marker of mitotic cells, and strong upregulation of p21 (Fig. 2D). Consistent with the reduced
291 expression of several key regulators of DNA replication (Supplementary Fig. 4C;
292 Supplementary Dataset 2 – Table 15), shYAP SCC13 cells arrested in G1 and progressed much
293 slower through S phase (Fig. 2E). Compromised cell cycle progression and increased terminal
294 differentiation led to reduced clonal growth of shYAP SCC13 cells (Fig. 2F).

295 Reduced activation of the replication stress checkpoint (phosphorylation of CHK1 on Ser317;
296 (34, 35)) was evident in SCC13 cells upon induction of shYAP (Fig. 2G), while depletion of
297 either YAP or TAZ in SCC13 cells reduced accumulation of replication stress-induced DNA
298 DSBs, marked by decreased γH2Ax expression (34, 39, 41, 43) (Fig. 2G). Furthermore, using
299 mRNA expression data from the DepMap project (https://depmap.org/portal/), we
300 discovered a strong correlation between the expression of a replication stress signature (36)
301 and an in-house generated SCC-specific YAP/TAZ activity signature comprising 10 YAP/TAZ
302 target genes (Supplementary Dataset 2 – Table 16) from our SCC13 RNAseq dataset in a panel
303 of 64 HNSCC cell lines (Supplementary Fig. 5A–D). Together, these findings indicated that
304 YAP/TAZ-driven oncogenic signalling contributed to the endogenous replication stress of SCC
305 cells.

306 Of note, reduced cell proliferation was reversible upon doxycycline withdrawal
307 (Supplementary Fig. 6), demonstrating that YAP knockdown slows down cell cycle progression,

308 but does not cause permanent growth arrest. The effects of shTAZ on SCC13 proliferation were
309 less dramatic (Fig. 2D, F). We conclude that, like in NHKs, YAP/TAZ regulate the balance
310 between proliferation and terminal differentiation also in cSCC cells, thereby promoting a
311 highly proliferative and undifferentiated cell state.

312 We next used the YAP/TAZ target gene expression signature derived from our RNA-seq data to
313 perform gene set variation analysis (GSVA; see materials and methods) on one of the largest
314 bulk RNA-seq datasets from patients with cSCC (237 patients) (95). This revealed that genes
315 that are positively regulated by YAP/TAZ in SCC13 cells are expressed significantly higher in
316 cSCC tumours (as well as their perilesional skin tissue) that have progressed to metastatic
317 disease, compared to those cSCC tumours that have not (Supplementary Fig. 7A). Genes that
318 were positively regulated by YAP/TAZ in SCC13 cells were also highly expressed in cSCC
319 metastases (Supplementary Fig. 7A). Conversely, genes that were negatively regulated by
320 YAP/TAZ in SCC13 cells displayed significantly reduced expression in cSCC metastases
321 (Supplementary Fig. 7B). This finding provides intriguing evidence for the involvement of
322 YAP/TAZ in the metastatic progression of human cSCC.

323

324 ***RIF1 is not directly involved in YAP/TAZ-controlled transcription.***

325 Compared to siY/T treatment, knockdown of RIF1 affected the expression of a smaller number
326 of genes (Fig. 3A). 165 DEGs (of which 33 are protein-coding) were downregulated, and 942
327 DEGs (of which 749 are protein-coding) were upregulated ($p<0.05$, FC>1.5; Fig. 3A,
328 Supplementary Dataset 2 - Tables 1–3). GSEA revealed that theses DEGs were predominantly
329 involved in cell cycle regulation, although the statistical significance of pathway enrichment
330 was generally quite low (Supplementary Fig. 8A–C; Supplementary Dataset 2 - Tables 7–9).
331 Interestingly, 710 out the 782 differentially expressed protein-encoding genes upon siRIF1

332 knockdown appeared to be co-regulated by YAP/TAZ, since the observed expression changes
333 were going into the same direction in both siRIF1 and siY/T experiments (Fig. 3B). However,
334 GSEA did not reveal any significantly enriched pathways (data not shown) among these
335 putative RIF1 and YAP/TAZ co-regulated genes. This is reminiscent of findings in mouse
336 embryonic stem cells, where limited gene expression changes in response to *Rif1* knockout
337 could neither be linked to any specific functions/pathways nor to the genome-wide
338 distribution of Rif1 on the chromatin (80). Instead, the gene expression changes in response
339 to *Rif1* knockout were suggested to be effects that are secondary to changes in DNA
340 replication timing (79, 80). Accordingly, an intriguing possibility is that the observed
341 expression changes of those genes that appear to be co-regulated by YAP/TAZ and RIF1 in
342 SCC13 cells are the consequence of altered replication timing (Fig. 6 and text below) and
343 changes to YAP/TAZ chromatin accessibility, and not of a direct involvement of RIF1 in YAP/TAZ-
344 regulated transcription.
345
346 ***YAP modulates RIF1 transcription and promotes RIF1 protein stability.***
347 Our RNAseq analysis revealed that *RIF1* mRNA expression was moderately downregulated in
348 response to siY/T knockdown (Fig. 2A), and a similar trend could be confirmed in independent
349 siY/T samples by RT-qPCR analysis (Fig. 3C). Accordingly, RIF1 protein expression was slightly
350 but reproducibly lower in siY/T compared to siNTC SCC13 cells (Fig. 3D) and was more strongly
351 reduced in shYAP cells with a more prominent depletion of YAP protein (Fig. 3E, F).
352 Interestingly, shTAZ had no impact on RIF1 protein levels (Fig. 3E), suggesting a specific
353 relationship between YAP and RIF1. Analysis of published RNAseq data of siY/T in N/TERT-2G
354 immortalized human keratinocytes (89) revealed that this relationship was conserved also in
355 NHKs (Fig. 3G). Moreover, we observed a significant correlation between *RIF1* mRNA

356 expression and single-sample enrichment scores of a generic Hippo/YAP/TAZ pathway gene
357 signature in a panel of 64 HNSCC cell lines using the DepMap portal
358 (https://depmap.org/portal/) (96) (Fig. 3H). An even stronger correlation was observed when
359 we used our in-house generated SCC-specific YAP activity signature (Supplementary Dataset
360 2 – Table 16, Supplementary Fig. 5C, F). Summarized, RIF1 expression closely correlates with
361 YAP/TAZ transcriptional activity in both normal and neoplastic human keratinocytes.

362 Combined siRNA-mediated knockdown of TEAD1, 3, and 4 (siTEAD1/3/4) in SCC13 cells
363 reduced RIF1 protein to levels similar to those observed in siY/T cells (Fig. 3I), indicating that
364 YAP modulates *RIF1* transcription through TEADs. Since our biochemical experiments had
365 revealed direct binding of YAP and RIF1 proteins, we also tested if this interaction additionally
366 stabilizes RIF1 protein. Indeed, by combining shYAP with cycloheximide treatment to stop
367 protein translation, we could reduce RIF1 protein expression in SCC13 cells to levels below
368 the detection limit of our chemiluminescence imaging system (Fig. 3J). Interestingly, YAP
369 protein levels remained stable during the treatment time course and were even upregulated
370 during the first 4 hours of cycloheximide treatment. This suggests that YAP protein
371 homeostasis is precisely fine-tuned in SCC cells. We conclude that YAP modulates *RIF1*
372 transcription trough TEADs, but additionally stabilizes RIF1 protein on the chromatin through
373 a direct interaction.

374

375 ***Increased association of YAP with RIF1 in response to replication stress.***

376 Our discovery of RIF1 as a YAP interaction partner in NHK and SCC cell lines raised the exciting
377 possibility that in normal and cancerous squamous epithelial tissues YAP could have dual,
378 transcriptional and non-transcriptional roles. In *Xenopus laevis* embryos, the YAP-RIF1
379 complex was previously shown to control the dynamics of DNA replication by limiting

380 replication origin firing (24). Using *Xenopus* egg extracts, a classical model for studying DNA
381 replication, Melendez Garcia et al. (24) showed that *Xenopus* YAP became recruited onto the
382 chromatin upon S phase induction, following the formation of the pre-replication complex
383 and in parallel with PCNA (proliferating cell nuclear antigen) loading (24). Here, we used a
384 double thymidine block to arrest human SCC13 cells at the G1/S phase boundary (83) and
385 assessed the levels of YAP on the chromatin upon S phase entry following thymidine washout.
386 We noticed an increase in the amount of chromatin-bound YAP as SCC13 cells where entering
387 S phase that correlated with the increased loading of PCNA (Fig. 4A). Consistent with the
388 reduced expression of key DNA replication regulators in siY/T cells (Supplementary Fig. 4C;
389 Supplementary Dataset 2 – Table 15) and the slowed S phase progression of shYAP cells (Fig.
390 2E), PCNA loading onto the chromatin was reduced in shYAP cells (Fig. 4A). Only a very limited
391 number of YAP-RIF1 PLA speckles overlapped with replication foci, marked by DNA
392 incorporation of EdU during a 1-hour pulse (Fig. 4B), suggesting that YAP is not associated
393 with nascent chromatin behind the replication fork. Moreover, only very few YAP-RIF1 PLA
394 speckles were present on the DNA of mitotic cells (Fig. 4C), consistent with the absence of
395 RIF1 from mitotic chromosomes (83, 97).

396 In addition to controlling origin firing and DNA replication timing, another key function of RIF1
397 is the protection of stalled replication forks from resection by nucleases in response to
398 replication stress and the promotion of replication restart (77, 78, 82, 98, 99). To test if YAP
399 might be recruited to either stalled or collapsed replication forks, we treated SCC13 cells with
400 4 mM hydroxyurea (HU) (100, 101) for periods of up to 24 hours. As shown in Fig. 4D, this
401 triggered strong activation of the replication stress checkpoint (phosphorylation of CHK1 on
402 Ser317; (34, 35)) and accumulation of DNA DSBs, marked by γH2Ax expression (39, 41, 43).
403 Persisting γH2Ax expression following washout of HU indicated accumulation of DNA damage

404 at stalled and subsequently inactivated replication forks upon 24 hours of HU treatment (100)
405 (Fig. 4D). While the YAP-RIF1 PLA signal remained unchanged upon short-term HU treatment,
406 it increased significantly after long-term (24 hours) HU treatment (Fig. 4E). Moreover, upon
407 long-term HU treatment, more YAP molecules were found in close vicinity of γH2Ax by in-situ
408 PLA (Fig. 4F), indicating that YAP associates with RIF1 preferentially near DNA DSBs at
409 insctivated replication forks. Summarized, these data provided evidence that in SCC cells, a
410 fraction of YAP is involved in RIF1-mediated DDR at replication forks.
411
412 ***RIF1 is highly expressed in several types of squamous cell carcinoma and upregulated during***
413 ***tumour progression.***
414 The strong effect of YAP depletion on the cell cycle-regulatory transcriptome (Fig. 2,
415 Supplementary Fig. 4) and the resulting cell cycle exit and commitment to terminal
416 differentiation (Fig. 2B–F) precluded a further in-depth analysis of non-transcriptional YAP
417 functions specific to DNA replication. Consequently, we focused on RIF1 itself, given its
418 regulation by YAP (Fig. 3) and the previously unknown function(s) of RIF1 in SCC.
419 We first assessed RIF1 protein expression levels in a panel of human cSCC cell lines, which
420 also included an isogenic cSCC progression series (102). Increased expression of RIF1 protein
421 was notable in all cSCC cell lines when compared to NHKs, including a cell line derived from a
422 pre-malignant cSCC precursor lesion (PM1) (102) (Fig. 5A). Consistent with our findings that
423 YAP controls RIF1 expression (Fig. 3), the protein levels of RIF1 were highest in SCC13 cells
424 featuring constitutively nuclear YAP (Supplementary Fig. 1B) (49) (as also indicated by a low
425 ratio of S127-YAP to total YAP, Fig. 5A). All cSCC lines in our panel, as well as the PM1 cells,
426 displayed higher levels of γH2Ax compared to NHKs, indicating elevated endogenous
427 replication stress (Fig. 5A).

428 To investigate if increased RIF1 expression was a general hallmark of cancers originating from
429 epidermal keratinocytes, we next quantified the nuclear abundance of RIF1 protein in a tissue
430 array comprising cSCCs of different differentiation grades, as well as different types of BCCs
431 (Fig. 5B, C). There were increased number of RIF1-expressing cells within the keratin-positive
432 tumour cell masses of both BCC and cSCC compared to normal skin epidermis, in particular
433 within the more aggressive tumour types of infiltrative BCC and poorly differentiated cSCC
434 (Fig. 5B, C). The pattern of RIF1 expression in cSCC correlated well with the known localisation
435 of cycling cells, which are located at the periphery in well-differentiated tumours, but diffusely
436 distributed throughout the tumour mass in moderately/poorly-differentiated tumours (103,
437 104). By examining publicly available immunohistochemistry data from the Human Protein
438 Atlas (https://www.proteinatlas.org/), we also observed increased numbers of RIF1-
439 expressing tumour cells in HNSCC and cervical SCC (CeSCC) (Supplementary Fig. 9A–C). To
440 obtain a pan-cancer overview of RIF1 protein expression levels, we used the UALCAN portal
441 (https://ualcan.path.uab.edu/) (105) to access protein expression data from the Clinical
442 Proteomic Tumour Analysis Consortium (CPTAC) (106). This revealed increased RIF1 protein
443 expression in several cancer types (Supplementary Fig. 9D). Importantly, in HNSCC, RIF1
444 protein expression increased with tumour grade (Fig. 5D). The UALCAN portal also allows
445 assessment of the impact of somatic alterations (small mutations or copy number alterations)
446 in several signalling pathways on the cancer proteome (105, 106). The CPTAC data include
447 somatic alterations in *NF2*/Merlin, *WWC1*, and *SAV1* as a proxy for Hippo pathway alterations
448 (106). WWC1 expression was previously shown to strongly correlate with YAP activity in
449 HNSCC (107), and knockout of the Hippo pathway scaffold proteins Sav1 or Mob1a/b in mice
450 caused rapid YAP-driven squamous carcinogenesis (28, 108, 109). *NF2* mutations have been
451 discovered in various types of SCC, with frequencies varying between 2.6% and 17%,

452 depending on study and cancer context (110-114). Of note, a distinct tumour subtype with
453 alterations in Hippo pathway genes exists in CeSCC that also displays increased expression of
454 YAP/TAZ target genes (110). Thus, in the context of human squamous cancers, somatic
455 alterations in *NF2*, *WWC1*, and *SAV1* can serve as reasonable indicators of Hippo pathway
456 activity status. We found that in both HNSCC (Fig. 5E) and LSCC (Supplementary Fig. 9E)
457 increased RIF1 protein expression predominantly correlated with somatic Hippo pathway
458 alterations in contrast to alterations in other signalling pathways, implying altered Hippo
459 pathway activity in the regulation of RIF1 expression. This agrees with our finding that RIF1 is
460 regulated by YAP at both the transcriptional and post-translational levels (Fig. 3).
461 Interestingly, in other cancer types, alterations in pathways other than Hippo signalling also
462 had a strong impact on increased tumour expression of RIF1 (Supplementary Fig. 9F, G).
463 Collectively, our multi-omics analysis confirmed a close relationship between Hippo/YAP/TAZ
464 signalling, replication stress, and RIF1 expression, and pointed towards a role of RIF1 in
465 squamous cell carcinogenesis.
466
467 ***Depletion of RIF1 causes increased origin firing in early S phase and accelerated S phase***
468 ***progression of squamous cell carcinoma cells.***
469 A highly conserved role of RIF1 is the genome-wide orchestration of DNA replication timing
470 (24, 79, 83, 84, 115). Although the precise mechanisms are still not fully understood, multiple
471 pieces of evidence point to a scenario where RIF1 serves as a molecular hub that co-regulates
472 spatiotemporal replication patterns and nuclear architecture. Through its abilities to bind
473 multiple molecules of DNA and to interact with the nuclear lamina, RIF1 organizes higher
474 order chromatin structure into zones of coordinated DNA replication (RIF1-associated
475 domains) (80, 83, 84, 115, 116). In addition, through its interaction with PP1, RIF1 was shown

476 to suppress the firing of late replicating origins within RIF1-associated domains by preventing
477 MCM subunit phosphorylation through Dbf4-dependent kinase (DDK; composed of Cdc7
478 kinase and its activator, Dbf4; MCM, minichromosome maintenance complex, core of the
479 replicative helicase containing six subunits MCM2-7), thereby antagonizing the activation of
480 the CMG (Cdc45–MCM–GINS) helicase complex (77, 81, 83, 85).

481 Consistent with a role of RIF1 in controlling S phase progression of SCC cells, we observed that
482 on release from a double thymidine block, shRIF1 SCC13 cells progressed more rapidly
483 through S phase (Fig. 6A). The phosphorylation levels of MCM2 and MCM4 proteins, targets
484 of the Cdc7 kinase (77, 83), were increased in RIF1-depleted SCC13 cells in a RIF1 dosage-
485 dependent manner (Fig. 6B), particularly in early S phase (Fig. 6C), indicating alterations in the
486 dynamics of origin firing (77, 81, 83, 85). Accordingly, chromatin loading of PCNA, which is
487 required for DNA replication after the action of Cdc7, was also increased during the early S
488 phase of shRIF1 SCC13 cells (Fig. 6C). Therefore, the faster progression of SCC13 cells through
489 S phase after RIF1 depletion likely reflects an increase in DNA replication initiation events in
490 early S phase (77, 83), suggestive of an altered replication timing programme. This could also
491 explain the changes in gene expression observed upon siRIF1 in SCC13 cells (Fig. 3A).

492

493 ***RIF1 protects against endogenous and exogenous replication stress in squamous cell***
494 ***carcinoma cells.***

495 Since a key function of RIF1 is the protection of stalled replication forks and the promotion of
496 replication restart (77, 78, 82, 98, 99), increased expression of RIF1 in SCC cells could therefore
497 indicate a role for RIF1 in enabling cells to deal with high levels of endogenous replication
498 stress. Indeed, there was a strong correlation between the expression of *RIF1* and a
499 replication stress signature (36) in HNSCC cell lines (Supplementary Fig. 5A, E). Knockdown of

500 RIF1 in SCC13 cells increased their endogenous replication stress, as evident from increased
501 levels of pS4/8-RPA32 (indicating accumulation of single stranded DNA at replication forks
502 and recruitment and activation of the replication stress kinases ATR/ATM/DNA-PK) as well as
503 increased levels of γH2Ax (indicating accumulation of DNA DSBs) (Fig. 7A). In contrast to the
504 strong activation of the replication stress checkpoint (phosphorylation of CHK1 on Ser317;
505 (34, 35)) observed upon HU treatment, the elevated endogenous replication stress in shRIF1
506 SCC13 cells did not translate into robust CHK1 activation (Fig. 7A). Consequently,
507 asynchronously proliferating shRIF1 cells displayed no dramatic alterations to their cell cycle
508 profiles (Fig. 7B). However, the accumulation of DNA damage in cultures of shRIF1 SCC13 cells
509 became more accentuated after a few passages, when cells had undergone multiple rounds
510 of cell division (Fig. 7C), resulting in reduced clonal colony growth (Fig. 7D). Together, our
511 results are thus consistent with a scenario where SCC cells depend on elevated RIF1
512 expression to deal with high levels of endogenous replication stress that are, at least in part,
513 controlled by YAP-driven oncogenic mechanisms.

514 Since we found that depletion of YAP reduced RIF1 protein levels (Fig. 3), we hypothesised
515 that shYAP SCC13 cells should therefore be more sensitive to exogenous replication stress
516 induced by treatment with HU (Fig. 7A). Indeed, we observed a synergistic effect of YAP
517 depletion and low doses of HU on SCC13 clonal colony growth (Fig. 7E, F).

518

519 **Discussion**

520 Our findings provide a novel insight into the oncogenic mechanisms of hyperactive YAP/TAZ
521 in SCC. While YAP/TAZ promote proliferation by regulating transcriptional programmes that
522 drive cell cycle progression, they also suppress commitment to terminal differentiation. Thus,
523 the functions of YAP/TAZ appear to be highly conserved within the epidermal lineage, as both

524 normal epidermal stem cells (49, 50, 89) and neoplastic keratinocytes in BCC (90) and cSCC
525 (this study) show strong dependency on YAP/TAZ signalling for cell proliferation. This suggests
526 that cancers originating from epidermal stem/progenitor cells 'hijack' the tissue regeneration-
527 promoting functions of YAP/TAZ to fuel their high rates of proliferation while remaining in an
528 undifferentiated cell state. The increased expression of genes that are positively regulated by
529 YAP/TAZ in both non-lesional and tumour tissue of human cSCCs that underwent metastatic
530 progression (Supplementary Fig. 7) provides strong support for this idea. Our RIME
531 experiments revealed that the transcriptional co-regulator functions of YAP/TAZ are likely
532 mediated by the BAF-type SWI/SNF and the NuRD chromatin remodelling complexes. Indeed,
533 in HNSCC cells, BAF-type SWI/SNF and YAP-TEAD complexes were shown to be co-dependent
534 for chromatin binding, whereby they create a positive-feedback mechanism to maintain open
535 chromatin for transcription (18). In contrast, recruitment of the NuRD complex (73) could be
536 involved in the observed co-repressor functions of YAP/TAZ.

537 We found that the cyclin-dependent kinase inhibitor p21/CDKN1A became strongly
538 upregulated in response to YAP depletion, suggesting that suppression of p21 is a key function
539 of YAP in squamous cancers. Of note, p21 was shown to act as an important brake to SCC
540 development (48, 117). Previous studies have also noted that keratinocytes express a pool of
541 p21 that is regulated in a TP53-independent fashion (41, 43). YAP/TAZ thus appear to serve as
542 an extra control layer for p21 expression in keratinocytes. In future work, it will be important
543 to establish if *CDKN1A* is direct transcriptional target of YAP-TEAD. A previous study which
544 employed a transgenic mouse model where cSCC development was driven by expression of
545 oncogenic *Kras*^{G12D} and knock-out of *Tp53* in epidermal stem cells (25), that simultaneous
546 activation of Kras^{G12D} and YAP/TAZ knock-down induces apoptosis. In our human cSCC cell line-
547 focused study we found that YAP/TAZ depletion has cytostatic- and differentiation-promoting,

548 rather than cytotoxic effects. It is worth noting that activating mutations in the *RAS* proto-
549 oncogenes are not very frequent in human cSCC (2), with some tumours (~10%) actually
550 showing copy number loss of *HRAS* (118). Induction of apoptosis in response to YAP/TAZ
551 depletion might thus be specific only to cSCCs expressing oncogenic RAS (25).

552 A major finding of this study was the identification of a complex functional relationship
553 between YAP and RIF1, whereby YAP modulates *RIF1* gene expression via TEAD TFs, but also
554 forms a complex with RIF1 on the chromatin. We found that the key functions of RIF1
555 (regulation of DNA replication dynamics (77, 79, 83, 115) and protection of replication forks
556 under replication stress (78, 82, 98, 99)) are conserved in squamous cancers. RIF1 enables SCC
557 cells to deal with their high levels of endogenous replication stress, since RIF1 depletion leads
558 to accumulation of DNA damage, which ultimately reduces clonal colony growth. Increased
559 formation of the YAP-RIF1 complex in response to HU treatment suggested a specific role of
560 YAP in enabling RIF1's functions at stalled and deactivated replication forks (82, 99). Indeed,
561 we found that YAP depletion and the concomitant reduction in RIF1 expression sensitised cSCC
562 cells to HU treatment. Of note, HU is sometimes used in chemoradiotherapy for HNSCC
563 patients (119). RIF1 protein is subject to proteolytic degradation (86, 120). We thus speculate
564 that the interaction with YAP on the chromatin stabilizes RIF1 and enables its proper functions
565 for DDR. This scenario is supported by our observation that the combination of YAP
566 knockdown and inhibition of protein synthesis caused a much stronger depletion of RIF1
567 protein than shYAP alone. Our findings thus provide evidence for a non-canonical role of YAP
568 in SCC, whereby it engages RIF1 to dampen the high levels of endogenous replication stress in
569 these cancers, which are—at least in part—caused by YAP's oncogenic functions itself. Since
570 normal human epidermal keratinocytes respond to expression of constitutively nuclear YAP
571 with oncogene-induced senescence (50), upregulation and stabilization of RIF1 expression in

572 cSCC cells through YAP-TEAD serves as an elegant mechanism whereby cancer cells with
573 hyperactivated YAP are able to escape senescence.
574
575 **Materials and Methods**
576 ***Human tissues***
577 All human tissue work was performed in the lab of Dr Beate Lichtenberger at the Medical
578 University of Vienna, Austria. Written informed patient consent was obtained before tissue
579 collection in accordance with the Declaration of Helsinki. The study was approved by the
580 Institutional Review Board under the ethical permits EK#1695/2021 and EK#1783/2020.
581
582 ***Cell culture***
583 All cell lines were routinely (quarterly test intervals) confirmed to be free of mycoplasma
584 infection using PCR LookOut® Mycoplasma PCR Detection Kit (Merck, UK).
585 Mouse 3T3 embryonic fibroblasts (subclone J2), originally established from random-bred
586 Swiss mice (121), were used to provide optimal clonal growth support to normal and
587 neoplastic human epidermal keratinocytes grown in co-culture (122). Stocks were kindly
588 provided by Prof Fiona Watt (Centre for Gene Therapy and Regenerative Medicine, King's
589 College London, UK; EMBL, Heidelberg, Germany; not authenticated), or were purchased from
590 Kerafast (Catalogue #EF3003). 3T3-J2 fibroblasts were routinely cultured in high-glucose
591 DMEM (Merck) supplemented with 10% (v/v) bovine serum (Fisher Scientific), 100 IU/mL
592 penicillin and 100 µg/mL streptomycin (Merck), and 2 mM L-glutamine (Merck) (complete
593 fibroblast medium) at 37°C, 5% CO2. Fibroblast cultures were not allowed to grow to
594 confluence and were not grown beyond passage 12 to prevent senescence or spontaneous

595 transformation. To prepare feeder cell layers, 3T3-J2 fibroblasts were treated for 3 hours with
596 4 µg/mL mitomycin C (Merck) at 37°C, 5% CO2, to irreversibly stall the cell cycle (123).

597 Stock cultures of primary normal human keratinocytes (NHKs, strain km) were obtained from
598 surgically discarded foreskin (49). SCC13 cells are a cell line established from a recurring
599 cutaneous SCC (cSCC) of facial epidermis and were obtained from Dr James Rheinwald
600 (Department of Dermatology, Harvard Skin Research Centre, USA), not authenticated (52). To
601 study the progression of human cSCC, we used four isogenic human cell lines that were
602 isolated from skin biopsies from a immune-suppressed patient at progressive disease stages:
603 PM1 cells were derived from a pre-malignant dysplastic lesion on the patient's head, MET1
604 was derived from a primary invasive cSCC growing on the patient's right hand, MET2 was
605 established from a rapid local recurrence after surgical removal of the primary tumour, and
606 MET4 was established from an axillary lymph node metastasis that developed from the
607 primary cSCC (102). The progression series cell lines were purchased from Ximbio (PM1
608 #153571, MET1 #153539, MET2 #153569, MET4 #153570), and were last re-authenticated in
609 Autumn of 2023. SCC-NR cells were isolated by Dr Nicholas Rabey at Addenbrooke's Hospital
610 (Cambridge, UK) from a portion of a surgically excised cutaneous SCC from the back of the
611 hand of an elderly male patient and were used in all experiments at passages 3 or 4 (49). All
612 other cell lines were used at passages 2–8. NHKs and cSCC cells were grown in FAD medium
613 (1 part high glucose DMEM GlutaMAX™ supplemented with pyruvate (Fisher Scientific) plus 3
614 parts Ham's F12 GlutaMAX™ (Fisher Scientific), supplemented with 1.8×10^{-4} M adenine
615 (Merck), 10% (v/v) foetal bovine serum (Fisher Scientific, batch-tested for optimal clonal
616 growth support), 5 µg/ml insulin (Merck), 0.5 µg/ml hydrocortisone (Merck), 10 ng/mL
617 epidermal growth factor (Peprotech), 8.5 ng/mL cholera toxin (Merck), 2 nM T3 supplement
618 (3,3',5-triiodo-l-thyronine sodium salt) (Merck), and 100 IU/mL penicillin and 100 µg/mL

619 streptomycin (Merck) on a feeder layer of mitotically inactivated 3T3-J2 cells, and grown at
620 37°C at 5% CO_2, as previously described (49).

621 HARA lung SCC cells (124) were purchased from the National Institutes of Biomedical
622 Innovation, Health, and Nutrition (NIBIOHN) JCRB Cell Bank, Japan (catalogue #JCRB1080.0),
623 and were re-authenticated in August 2024. HARA cells were cultured in complete RPMI
624 medium (10% (v/v) fetal bovine serum, 100 IU/mL penicillin and 100 µg/mL streptomycin
625 (Merck), and 2 mM L-glutamine (Merck).

626

627 ***Generation of stable shRNA-expressing cell lines***

628 SCC13 cells, cultured on feeder cells to ~70% confluence, were disaggregated in trypsin/EDTA
629 and cells (2.5×10^5) were seeded into 6-well cell culture plates (Corning™ Costar™, UK) and
630 cultured for 24 h in FAD medium. Medium was then changed to Opti-MEM (Fisher Scientific).
631 To generate stable SCC13 cell lines expressing RIF1-targeting shRNAs, SCC13 cells were
632 infected with MISSION® lentiviral particles (Merck, the sequences of the shRNAs can be found
633 in (Supplementary Table 1A) at a multiplicity of infection (MOI) of 2–3 in the presence of
634 5 µg/ml polybrene (Hexadimethrine bromide, Merck). For creating stable SCC13 cell lines
635 expressing YAP- or TAZ-targeting shRNAs, the SMARTvector™ inducible lentiviral platform was
636 used, which implements a microRNA-scaffolded Tet-On 3G bipartite induction system
637 (Horizon Discovery-Dharmacon™, the sequences of the shRNAs can be found in
638 Supplementary Table 1B). The lentiviral vector included a puromycin resistance element
639 (PuroR) for selection post-infection, as well as a 2A self-cleaving peptide which allowed for
640 PuroR and Tet-On 3G expression from a single mCMV promoter that was selected for
641 negligible basal expression and strong activation when induced (data not shown). A

642 doxycycline-inducible TRE3G promoter was driving expression of the shRNA as well as a
643 fluorescent turbo-RFP reporter. After 24 h incubation with viral particles, medium was
644 changed to FAD medium, and shRNA-expressing cells were selected for 7 days using
645 puromycin (2.5 µg/ml, Merck) in co-culture with puromycin-resistant 3T3-J2 fibroblasts
646 (kindly provided by Prof Fiona Watt, Centre for Gene Therapy and Regenerative Medicine,
647 King's College London, UK; EMBL, Heidelberg, Germany). For experiments using the stable
648 SCC13 cell lines with doxycycline inducible shRNAs, cells were incubated with FAD medium
649 supplemented with 5 µg/mL doxycycline (Tocris) for 48 hours before trypsinisation and
650 seeding for downstream experiments.
651
652 ***siRNA transfection***
653 24 hours after seeding, cells were transfected with 10-20 nM of ON-TARGET plus SMARTpool
654 siRNAs (Horizon Discovery, Supplementary Table 1C) using INTERFERin® transfection reagent
655 (Polyplus, VWR) in Opti-MEM (|Fisher Scientific) for 5 hours, then washed with PBS and grown
656 in FAD medium for up to 72 hours.
657
658 ***Colony Formation Assay***
659 1x10^3 cells per well were seeded in triplicate technical replicates into 6-well cell culture
660 plates (Corning™ Costar™, UK) without feeder cells and were cultured for 10-14 days with
661 frequent (every 2–3 days) media changes, then fixed in 4% PFA for 30 minutes at room
662 temperature. In case of treatment with hydroxyurea, different drug concentrations were
663 added 24 hours after seeding and fresh drug was added with each medium change. Colonies
664 were stained using crystal violet solution (2% (w/v) crystal violet (Merck, UK) dissolved in 20%
665 (v/v) methanol) for one hour at room temperature, and then washed extensively in deionised

666 water and air-dried. Colonies were either imaged using a transilluminator and cell phone
667 camera or were scanned using a flat-bed scanner. Quantification of culture area covered by
668 colonies were performed using ImageJ.
669
670 ***Cell synchronisation by double thymidine block***
671 Cells were seeded in FAD medium and treated with 2.5 mM thymidine (Merck, UK) for 24
672 hours at 37°C, 5% CO_2. Cells were then washed with FAD medium (without thymidine), fresh
673 FAD medium (without thymidine) was added, and cells were incubated for 15 hours before
674 the medium was supplemented again with 2.5 mM thymidine for a further 24 hours. Following
675 thymidine washout, cells were grown in FAD medium.
676
677 ***Cell cycle analysis by flow cytometry***
678 Prior to trypsinization, Click-iT™ EdU (Fisher Scientific, UK) was added to the cell culture
679 medium to a final concentration of 10 µM, and cells were incubated for 30 minutes at 37°C.
680 Trypsinized cells were then centrifuged at 500 x g for 3 minutes (RT), the supernatant was
681 removed, and the pellet resuspended in 3 mL PBS, followed by another centrifugation at 500
682 x g (RT) for 5 minutes. Pelleted cells were next resuspended in 100 µl 0.9% (w/v) NaCl and
683 added dropwise to 1.8 ml ice cold 70% (v/v) ethanol for fixation and stored at -20°C for a
684 minimum of 2 hours before being centrifuged again for 5 minutes at 400 x g (4°C). The cell
685 pellet was then resuspended in 0.5 ml PBS and transferred to a clean tube, and cells were
686 centrifuged for 5 minutes at 400 x g (4°C). This cell pellet was then resuspended in 100 µl Click-
687 iT™ cell reaction buffer (Fisher Scientific, UK) and incubated at RT in the dark for 30 minutes.
688 EdU-labelled cells were then centrifuged for 5 minutes at 400 x g (4°C), cell pellets were
689 resuspended in 500 µl 1% (w/v) BSA in PBS and centrifuged for 5 minutes at 400 x g (4°C), then

690 resuspended in 500 µl PBS. RNase (Merck) was added to a final concentration of 0.5 µg/ml
691 and the sample was incubated on a heat block at 37°C for 15 minutes. Propidium iodide
692 (Merck) was added to a final concentration of 20 µg/ml and the sample was incubated on ice
693 for 20 minutes in the dark before a minimum of 20,000 cells were analysed on a FACS Canto™
694 cell sorter (BBD Biosciences). Data were analysed using FCS Express™, De Novo Software
695 (version 7.14.0020).
696
697 ***Rapid immunoprecipitation mass spectrometry of endogenous proteins (RIME)***
698 NHK and SCC13 cells were seeded at clonal density (500,000 cells) into 15 cm dishes
699 containing a mitotically inhibited 3T3-J2 fibroblast feeder layer and cultured for 4 days. This
700 enabled the formation of small colonies with predominantly nuclear YAP/TAZ expression
701 (Supplementary Fig. 1B). Two independent cultures (=independent experiments, starting from
702 separate cell stocks) were grown for each cell type. Following removal of the feeder layer on
703 day 4 of culture, cells were grown in complete FAD medium (conditioned by mitotically
704 inhibited 3T3-J2 fibroblast cells) for a further 24 hours. Cells were fixed with 1% (v/v)
705 methanol-free formaldehyde for 8 min at RT and the fixation reaction was subsequently
706 rapidly quenched with 0.125 M glycine for 5 min. Fixed cells were gently scraped into ice-cold
707 washing buffer (0.5% (v/v) IGEPAL CA-630, 100 µm PMSF, in PBS, pH 7.4) and were washed
708 three times by centrifugation (800 x g, 10 minutes, 4°C) and resuspension. The final cell pellets
709 (containing between 2 x 10^7 and 7 x 10^7 cells) were stored at -80°C and shipped to Active Motif
710 on dry ice.

711 For each cell pellet, chromatin isolation and immunoprecipitation was performed in technical
712 replicates for YAP and IgG control. Control RIME was performed using isotype-matched IgG,
713 and for each independent experiment, the two replicate IgG control immunoprecipitations

714 were pooled for mass spectrometry analysis. Chromatin was isolated from formaldehyde-fixed
715 cell pellets by the addition of lysis buffer (custom, proprietary to Active Motif), followed by
716 cell disruption with a Dounce homogenizer (15 ml volume with tight-fitting pestle) to release
717 nuclei. Nuclei were sonicated on ice in ChIP buffer (custom, proprietary to Active Motif) using
718 an EpiShear Probe Sonicator (68% pulsed sonication: 30sec on/30sec off, 10 minutes total
719 sonication time) to lyse the cells and shear the DNA to an average fragment length of 300-500
720 bp. Genomic DNA for chromatin quantification was prepared by treating aliquots of chromatin
721 with RNase (Merck), proteinase K (Merck) and heat treatment (65°C overnight) for de-
722 crosslinking, followed by ethanol precipitation. Pellets were resuspended in 1/5 volume Tris-
723 EDTA buffer, and the DNA concentration was quantified on a NanoDrop 2000 (Fisher Scientific,
724 USA) spectrophotometer. An aliquot of sheared chromatin (150 ug) was precleared with
725 protein G agarose beads (Invitrogen). Chromatin immunoprecipitation was performed using
726 15 ug of purified rabbit polyclonal YAP-specific antibody (US Biologicals, Y1200-01D) or rabbit
727 IgG (control) and protein G magnetic beads (Active Motif). Immunoprecipitated chromatin-
728 protein complexes were washed extensively with RIPA buffer (1x, Active Motif) and then with
729 100 mM ammonium bicarbonate (Merck, USA). On-bead proteolytic digestion was performed
730 using trypsin (Worthington Biochemical, USA; 10 ng/µl). Protein digests were separated from
731 the beads using a magnetic rack, and digested peptide mixtures were desalted by solid-phase
732 separation using a C18 spin column (Harvard Apparatus, USA). The eluted peptides were
733 vacuum dried using a speedvac.

734 Digested peptides were reconstituted in 5% (v/v) acetonitrile and 0.1% (v/v) trifluoroacetic
735 acid and analyzed by LC-MS/MS on a Thermo Scientific Q Exactive Orbitrap Mass spectrometer
736 linked to Dionex Ultimate 3000 HPLC (Thermo Scientific, USA) and a nanospray Flex^{TM} ion
737 source. The digested and desalted peptides were loaded directly onto the separation column

738 (Waters BEH C18, 75 µm x 100 mm, 130Å 1.7u particle size). Peptides were eluted using a 120-
739 minute gradient with a flow rate of 323 nl/min. The gradient was formed using
740 increasing/decreasing concentrations of buffer B (0.1% formic acid in acetonitrile); (1)
741 increase to 5% (v/v) B over 12 min, (1) gradual increase to 25% (v/v) B until the 90 min mark,
742 (3) gradual increase to 95% (v/v) B for 5 min, (4) 95% (v/v) B for another 4 min, (5) gradual
743 decrease to 5% (v/v) B over 20 min. An MS survey scan was obtained for the m/z range 340-
744 1600; MS/MS spectra were acquired using a top 15 method, where the top 15 ions in the MS
745 spectra were subjected to HCD (High Energy Collisional Dissociation). An isolation mass
746 window of 1.6 m/z was set for precursor ion selection, and normalized collision energy of 27%
747 was used for fragmentation. A 20-second duration was used for the dynamic exclusion.

748 Tandem mass spectra were extracted and analyzed by PEAKS Studio (version X+,
749 Bioinformatics Solutions Inc., Canada). Charge state deconvolution and de-isotoping were not
750 performed. Reference databases consisted of the UniProtKB/Swiss-Prot database (version
751 180508; 71,771 curated entries) and the cRAP database of common laboratory contaminants
752 (www.thegpm.org/crap; 114 entries). Databases were searched with a mass tolerance of 0.02
753 Da for fragment ions in MS/MS mode, and a parent ion tolerance of 10 PPM in MS mode. Post-
754 translational protein modifications allowed were methionine oxidation, asparagine and
755 glutamine deamidation, which were searched as variable modifications.

756 PEAKS Studio software built-in decoy sequencing and FDR determination was used to validate
757 MS/MS-based peptides. PEAKS Studio uses the “Decoy Fused Method” when calculating FDR
758 where the default cut-off is set to -10logP > 20 to ensure high-quality peptide spectrum
759 matches and to increase confidence in the proteins list obtained. Protein identifications were
760 accepted if they could pass the -10logP of > 20 and contained at least 1 identified unique

761 peptide. FDR for peptide spectrum matches was set at <1%. Proteins that contained similar
762 peptides and could not be differentiated based on MS/MS analysis alone were grouped to
763 satisfy the principles of parsimony. Proteins sharing significant peptide evidence were
764 grouped into protein groups.
765
766 ***RIME proteomics data analysis***
767 The following filtering criteria were applied to the raw proteomics data obtained from PEAKS
768 studio for each cell type (Supplementary Dataset 1). (1) Identified proteins with <2 unique
769 peptides, an average spectral count >2 in the IgG immunoprecipitation controls for
770 experiments 1 and 2, or a spectral count of <4 in any of the four YAP RIME technical replicates
771 were removed from further analysis. (2) Proteins matched to commonly identified IgG
772 contaminant proteins (data downloaded from the contaminant repository for affinity
773 purification (CRAPome, Crapome.org, accessed November 2019)) and to mitochondrial
774 proteins were excluded from further analysis. (3) Proteins displaying a fold change <4 of mean
775 spectral counts in YAP immunoprecipitations vs spectral counts in the respective IgG control
776 immunoprecipitation in any of the two independent experiments were removed to eliminate
777 low confidence hits that were not considerably more represented in the YAP
778 immunoprecipitation than the IgG immunoprecipitation. High confidence YAP-interacting
779 proteins were further screened for potential physiological significance by filtering against lists
780 of candidate genes positively and negatively regulating clonal growth of NHK and SCC-13 cells
781 (Walko et al., 2017). Interaction networks were created using Cytoscape version 3.9.1 and
782 using the Cytoscape STRING app version 1.7.1, and manually curated into functional groups
783 using input from Gene Ontology Enrichment Analysis performed using gprofiler
784 (https://biit.cs.ut.ee/gprofiler/gost) functional profiling tool with electronic GO annotations

785 unselected (Reimand et al., 2019) and visualised using EnrichmentMap (Cytoscape app
786 version: 3.3.4) in Cytoscape (version:3.9.1).
787
788 ***Immunofluorescence Microscopy***
789 Cells were seeded onto acid-washed and UV-sterilized glass coverslips coated with rat tail
790 collagen I (10 µg/ml; Fisher Scientific, UK) and fixed using 4% (v/v) paraformaldehyde (PFA)
791 for 30 minutes at RT. Immunostaining was performed in a PBS-humidified chamber. Cells were
792 permeabilised with 0.1% (v/v) Triton-X100 (Merck, UK) for 25 minutes then blocked in 10%
793 (v/v) BSA (Merck, UK) + 0.1% (v/v) Triton-X100. Primary antibodies (Supplementary Table 2)
794 were diluted in antibody diluent buffer (2% (v/v) BSA + 0.1% (v/v) Triton-X100) and incubated
795 overnight at 4°C. Coverslips were washed thoroughly with PBS, secondary antibodies
796 (Supplementary Table 2), diluted in antibody diluent, were added, and the samples incubated
797 for 1 hour at RT in the dark, then washed multiple times with PBS and once with MilliQ water.
798 Coverslips were mounted onto glass microscope slides using ProLong Gold™ anti-fade
799 mounting medium with DAPI (Fisher Scientific, UK,) or alternatively, incubated with 2 µg/ml
800 Hoechst 33342 (Fisher Scientific, UK) in PBS for 5 minutes, washed once with PBS, and
801 mounted with ProLong Gold™ anti-fade glass mounting medium without DAPI (Fisher
802 Scientific, UK). For confocal microscopy, images were acquired using a ZEISS LSM 880 laser
803 scanning confocal microscope using 40x/1.3 Oil DIC UV-IR M27 or 63x/1.4 Oil DIC UV-IR M27
804 objectives at 16 Bit depth, 0.5 µm optical Sections for Z-stacks, and 2048x2048 pixel
805 resolution. Images were processed using ImageJ (https://imagej.nih.gov/ij/) or ZEN blue
806 (Zeiss) with maximal orthogonal projection of Z-stacks. Quantification was performed using
807 CellProfiler (version 4.0.7). Immunofluorescence images in Supplementary Figure 1B were
808 obtained on a ZOE® Fluorescent Cell Imager (Bio Rad) using standard setup (20x objective)

809 and digital zoom. Minimal processing (changes in brightness and contrast) was applied equally
810 across entire images and applied equally to controls.
811
812 **Quantification of RIF1 expression in human tissues**
813 Immunofluorescence staining was performed on 4 µm human FFPE sections according to
814 standard protocols. Antigen retrieval was conducted in Dako Target Retrieval Solution, pH 9.0
815 (Agilent Technologies, Santa Clara, California, USA), and 3% (w/v) BSA in PBS containing 0.05%
816 (v/v) Tween 20 (PBS-T) was used for blocking. Primary antibodies against Keratin 14 (chicken
817 pAb (Poly9060), BioLegend Cat# 906004, RRID:AB_2616962; 1:250) and RIF1 (rabbit mAb
818 (D2F2M), Cell Signalling Technology Cat# 95558, RRID:AB_2800249; 1:50) were diluted in 1%
819 (w/v) BSA in PBS-T and incubated overnight. Fluorescently labelled donkey anti-chicken (IgY
820 (H+L) highly cross adsorbed, Alexa Fluor™ 594, Fisher Scientific, catalogue # A78951, RRID
821 AB_2921073; 1:500,) and donkey anti-rabbit (IgG (H+L) highly cross-adsorbed secondary
822 antibody, Alexa Fluor™ 488, Fisher Scientific, catalogue # A-21206, RRID AB_2535792; 1:500,)
823 secondary antibodies were incubated for 90 minutes at ambient temperature. DAPI was used
824 for nuclear counter-staining. Images were captured using the Vectra Polaris™ imaging system,
825 and image analysis was conducted with the HALO® image analysis platform v3.6.4134. The
826 HighPlex FL v4.2.14 plugin was employed for image analysis, with signal intensity thresholds
827 set for the Opal620 (AF594) channel to differentiate positive from negative cells. The
828 DenseNet V2 (Halo AI) classifier was trained and applied to differentiate between tumour and
829 stroma regions. Depending on the size of the tissue, between 2-13 regions of interest with an
830 area of 1 mm^2, representing the tumour were analyzed. Data analysis was performed using
831 GraphPad Prism version 8.0.0 for Windows (GraphPad Software, San Diego, California USA,
832 www.graphpad.com).

833 Additional images of human squamous cell carcinoma samples were obtained by datamining
834 the www.proteinatlas.org database (125, 126).
835
836 ***Proximity Ligation Assay***
837 Cells were fixed and permeabilised as described above. Coverslips were blocked in Proximity
838 Ligation Assay (Duolink®, Sigma) blocking buffer, and primary antibodies (Supplementary
839 Table 2), diluted in Duolink® antibody diluent, were added overnight. Proximity ligation assay
840 reactions were performed as per the manufacturer's instructions. Coverslips were mounted
841 onto glass slides using Duolink® PLA mounting medium with DAPI and sealed with clear nail
842 polish. Images were acquired on a Zeiss LSM-880 confocal microscope using a 40x/1.3 Oil DIC
843 UV-IR M27 objective. All images belonging to the same experimental repeat were acquired in
844 one imaging session at 16-Bit depth using a Z-stack (0.5 µm slice interval) and a 2048x2048
845 pixels dimension. Images were analysed on ZEN blue version 3.3.89.0000 and processed using
846 a maximal frontal orthogonal projection including all Z-stack slices. Background fluorescence
847 was removed using the same parameters for each image belonging to the same image set (=
848 experimental repeat). Image quantifications were performed using CellProfiler version 4.0.7.
849 Nuclei were defined as parent objects using the 'IdentifyPrimaryObjects' module based on
850 DAPI fluorescence signal and intensity of PLA signal per nucleus was quantified within the
851 defined nuclear area using the 'MeasureIntensity' module. To account for differences in YAP-
852 RIF1 and YAP-TEAD fluorescence signal intensities between different experimental repeats
853 (Figure 1), mean nuclear PLA signal fluorescence intensity in shYAP/TAZ cells was normalized
854 to that in shNTC cells (24). A one sample two-tailed t test was then used to test for statistical
855 significance (24). Statistical significance between the mean PLA signal intensities in the shNTC

856 and shY/T cell populations (assessed by Mann-Whitney test) was high ($p<0.0001$) for each
857 individual experiment (not shown).
858
859 ***Preparation of protein extracts for immunoblotting***
860 RIPA buffer (1x) (Cell Signalling Technologies) or Cell Lysis buffer (1x; Cell Signalling
861 Technologies, #9803; for co-immunoprecipitation experiments), supplemented with protease
862 inhibitors (cOmplete™ ULTRA, EDTA-free, Merck, UK) and phosphatase inhibitors (PhosStop,
863 Merck, UK), was added to cell culture plates and cells were lysed on ice for 15 minutes. Cell
864 remnants were then scraped into the lysis buffer, the lysate was transferred into a tube and
865 sonicated in an ice bath using an MSE Soniprep 150 plus sonicator at 12 Amp for 15 minutes
866 with shaking. Lysates were centrifuged at 16,000 x g for 10 minutes (4°C). For co-
867 immunoprecipitation experiments, sample sonication was not performed. The supernatant
868 was collected, and BCA assay was performed to measure protein concentration using Pierce
869 BCA Protein Assay Kit (Thermo Fisher, UK).
870
871 ***Preparation of chromatin-bound protein fractions***
872 Chromatin fractions were prepared as described (77). Briefly, cytoskeleton buffer (300 mM
873 sucrose, 3 mM $MgCl_2$, 100 mM NaCl, 0.5% (v/v) Triton X-100, 10 mM HEPES (pH 7.4))
874 supplemented with protease inhibitors (cOmplete™ ULTRA Tablets, EDTA-free, Merck, UK) and
875 phosphatase inhibitors (PhosStop, Merck, UK) was added to cells growing in cell culture
876 dishes, and these were incubated on ice for 5 minutes. Cells were then scraped into the buffer
877 and the extract was transferred to a microcentrifuge tube and incubated on ice for further 10
878 minutes. Samples were then centrifuged at 500 x g for 5 minutes at 4°C, and the supernatant
879 was removed and discarded. Chromatin pellets were washed twice in cytoskeleton buffer

880 without Triton-X100 and resuspended in 50 µl RIPA buffer (Cell Signalling Technologies, UK)
881 containing protease and phosphatase inhibitors, and incubated on ice for 5 minutes. 50 units
882 Benzonase® Nuclease (Merck, UK) and $MgCl_2$ (Sigma, UK, final concentration: 3 mM) were
883 added, and the chromatin fraction was incubated on ice for 20 minutes until it had visibly
884 reduced viscosity. The chromatin fraction was then centrifuged at 16,000 x g for 10 minutes
885 at 4°C, and the supernatant was recovered for immunoblotting analysis.
886
887 ***Co-immunoprecipitation from nuclei-enriched fractions***
888 Cells were grown to ~70% confluency and were washed twice with ice-cold PBS before
889 incubation on ice for 15 minutes with nuclear extraction buffer (50 mM KCl, 2 mM $MgCl_2$, 1
890 mM EDTA, 1 mM DTT, 0.1% (v/v) IGEPAL CA-630, 10 mM HEPES (pH 7.4)), supplemented with
891 protease inhibitors (cOmplete™ ULTRA, EDTA-free, Merck, UK) and phosphatase inhibitors
892 (PhosStop, Merck, UK)). Cell remnants were then scraped into the buffer, the suspension was
893 collected into pre-cooled microcentrifuge tubes, vortexed for 10 seconds, and centrifuged at
894 750 x g for 5 minutes (4°C) to pellet nuclei. The cytoplasmic fraction was removed and the
895 nuclear pellet was washed once in ice-cold PBS, resuspended in ice-cold nuclear lysis buffer
896 (450 mM NaCl, 0.1 mM EDTA, 3 mM $MgCl_2$, 0.1% Triton X-100, 1% (v/v) IGEPAL CA-630, 1 mM
897 DTT, 20 mM HEPES (pH 7.4)) supplemented with protease inhibitors (cOmplete™ ULTRA, EDTA-
898 free, Merck, UK) and phosphatase inhibitors (PhosStop, Merck, UK), transferred to a clean pre-
899 cooled micro-centrifuge tube, and incubated on ice for 15 minutes. Chromatin was then
900 sheared either by passaging 10 times through a 27G needle attached to a 1 ml syringe or by
901 the addition of Benzonase® Nuclease (Merck, UK). Needle-sheared nuclear fractions were
902 centrifuged at 13,000 x g for 10 minutes (4°C) and the supernatant was diluted (1:3) to a final
903 concentration of 150 mM NaCl using nuclear lysis buffer without NaCl. For Benzonase®-

904 treatment of nuclear fractions, chromatin suspension in nuclear lysis buffer was similarly
905 adjusted to 150 mM NaCl using nuclear lysis buffer. Benzonase® was then added, and the
906 chromatin suspension was incubated on ice for 15 minutes with intermittent vortexing. EDTA
907 was added to a 1 mM final concentration and samples were centrifuged at 13,000 x g for 10
908 minutes (4°C).

909 BCA assay was performed to measure protein concentration, and agarose gel electrophoresis
910 of DNA was used to validate the Benzonase digest. To this end, a 1% (w/v) agarose (Sigma, UK)
911 gel was prepared using 1x Tris-acetate-EDTA buffer (Fisher Scientific, UK) and GelRed® Nucleic
912 Acid Stain (Merck, UK). 10 µl of sample was incubated with 1 µl proteinase K for 1 hour at 65C
913 and then diluted with TriTrack DNA loading dye (Fisher Scientific, UK) and run for 1-2 hours at
914 100V in parallel with GeneRuler1 kb Plus DNA Ladder (Thermo Fisher, UK). Gels were imaged
915 using a Syngene Gel Doc system.

916 Nuclear protein samples (containing 2 mg/ml protein) were incubated with 0.07 ug anti-YAP
917 (D8H1X, Lot 4, Cell Signalling Technology) antibody or 0.07 ug of isotype-matched IgG control
918 antibody (Supplementary Table 2) and DTT (1 mM) in micro-centrifuge tubes overnight at 4°C
919 with constant rotation. Protein G Dynabeads™ (Thermo Fisher, UK) were washed four times in
920 PBS supplemented with 0.05% (v/v) Tween-20 (PBS-T, IP wash buffer) using a DynaMag™
921 magnetic rack (Thermo Fisher, UK), transferred to a new tube and washed once in IP wash
922 buffer. Protein G Dynabeads were then resuspended in 50 µL IP-buffer and added to IP
923 reactions, which were then incubated with the beads for 4 hours at 4°C with constant rotation.
924 To pellet the beads, samples were then placed on the DynaMag™ magnetic rack, the
925 supernatant was removed, bead-bound protein complexes were washed 3 times in PBS-T,
926 transferred to a fresh micro-centrifuge tube, resuspended in 20 µl 50 mM glycine (pH 2.8) and

927 10 µl 3x Laemmli buffer (BioRad, UK) + β-mercaptoethanol (elution buffer), and incubated for
928 10 minutes at 95°C. Beads were removed using the DynaMag™ magnetic rack and the eluted
929 proteins were analysed by SDS-PAGE (alongside 10 ug (1%) of input lysate) and
930 immunoblotting.
931
932 ***Immunoblotting analysis***
933 Protein samples were denatured and reduced in Laemmli buffer (BioRad, UK) containing 10%
934 (v/v) β-mercaptoethanol for 5 minutes at 95°C and loaded onto precast 4-20% or 4-15%
935 polyacrylamide mini-PROTEAN Tris-Glycine eXtended (TGX) gels (BioRad, UK). Proteins were
936 transferred onto either 0.2 µm pore-size Nitrocellulose membranes or methanol-activated
937 0.45 µm pore-size PVDF membranes (BioRad, USA), using either the Trans-Blot Turbo Transfer
938 System (BioRad, UK) or tank (wet) transfer depending on protein molecular mass. Large
939 proteins were transferred by wet transfer in wet transfer buffer (3.05 g/l Tris-base, 14.4 g/l
940 glycine) either overnight at 25V (4°C) or for 60 minutes with extensive cooling in wet transfer
941 buffer containing 20% (v/v) methanol at 300 mA. Membranes were blocked in 5% (w/v) BSA
942 dissolved in Tris-buffered saline (TBS) containing 0.1% (v/v) Tween 20 (TBS-T)(=blocking
943 buffer) for 1 hour at RT and primary antibodies (Supplementary Table 2), diluted in blocking
944 buffer, were incubated with the membranes overnight at 4°C with agitation. Membranes were
945 washed three times for 10 minutes with TBS-T and then incubated with secondary horseradish
946 peroxidase (HRP)-conjugated antibodies. Clarity western ECL substrate reagent (BioRad, UK)
947 was used to image immunoblots using a Fusion Solo chemiluminescence imager (Vilber
948 Lourmat, UK). Where possible, over-saturated images were avoided and exposures within the
949 dynamic range were selected. Band intensities were quantified based on pixel volume of the
950 bands using Fusion software (Vilber Lourmat, UK) or Image software (Bio Rad).

951

952 ***RNA preparation and next generation sequencing***

953 RNA was extracted from cells using the RNeasy Plus Mini kit (Qiagen, UK) and the QIAshredder
954 shredding system (Qiagen, UK) as per the manufacturer's instructions. RNA yield and purity
955 were analysed using the Quant-iT™ Qubit RNA BR Assay Kit (Thermo Fisher, UK) in Qubit™
956 Assay Tubes (Thermo Fisher, UK) on a Qubit 4 Fluorometer (Thermo Fisher, UK). RNA
957 sequencing was outsourced to Novogene Ltd. (UK). Messenger RNA was purified from total
958 RNA by poly-A enrichment method using poly-T oligo-attached magnetic beads. RNA library
959 preparation was performed using the Novogene in-house kit NGS RNA Library Prep Set
960 (PT042) for the preparation of a 250~300 bp insert cDNA library (unstranded). The library was
961 checked with Qubit and real-time PCR for quantification and bioanalyzer for size distribution
962 detection. Paired end PE150 sequencing was performed on Novaseq6000 short-read
963 sequencing machine (6Gb raw data per sample) platform. Base calling was performed by
964 Novogene using RTA (Real Time Analysis) software. All samples had a Phred score >30.

965

966 ***RNA sequencing data analysis***

967 Paired reads were aligned to Ensembl GRCh38.105 2.7.4a (127) using bowtie2 (v2.4.4)(128)
968 default settings, sorted and indexed with Samtools (v1.2)(129), and unstranded exonic read
969 pairs were counted using FeatureCounts (v2.0.7)(130) using a slightly modified Ensembl gtf
970 with 'chr' prefix nomenclature. DESeq2 (v1.44.0)(131) was used in R (v4.4.2) to assess features
971 with >10 reads across conditions and differential expression of transcripts with a fold change
972 >1.5 and FDR <0.05. All other results were given the value 0 and genes with no differential
973 expression were removed from the final data frame for visualisation purposes only.

974

975 ***Pathway analysis***

976 Gene Set Enrichment Analysis (132) was performed in R, using clusterProfiler (v4.12.6)(133)
977 on all genes annotated with Entrez IDs using AnnotationDbi (v1.66.0) and org.Hs.eg.db.Hs
978 (v3.19.1) packages. GO Biological Processes (134, 135), Hallmark (136) and Reactome (137)
979 pathway gene sets were downloaded from the Molecular Signature Database
980 (https://www.gsea-msigdb.org/gsea/msigdb) using msigdbr (v7.5.1). Specific sets of genes
981 defining progenitor cell populations, early differentiation and late (terminal) differentiation
982 have been experimentally validated using organotypic models (93). 'set.seed' in R (v4.4.2) was
983 set to '1234' and Benjamini-Hochberg correction (adjusted p-value <0.05) was used for
984 multiple comparison corrections.

985

986 ***Gene Set Variation Analysis***

987 A more stringent p-value threshold ($<1\times10^{-8}$) was applied to the SCC13 siYAP/TAZ RNA-
988 seq dataset to reduce the gene set size to <500, as recommended for robust gene set
989 variation analysis (GSVA) (138). This yielded 486 upregulated and 250 downregulated
990 DEGs in siYAP/TAZ compared to siNTC SCC13 cells. GSVA was performed using the GSVA
991 function (GSVA R package v1.52.3) with default settings. The input comprised the selected
992 SCC13 RNA-seq gene sets and an expression matrix from 237 cSCC patients with known clinical
993 outcome (95), covering primary cSCC (metastatic and non-metastatic), perilesional normal
994 skin and metastasis where available. GSVA enrichment scores were calculated for each
995 sample, and boxplots were used to visualize differential pathway activity across tissue types.
996 T-tests were applied to assess significant differences in enrichment scores between groups.

997

998

999 ***RT-qPCR***

1000 mRNA was converted to cDNA (including the removal of genomic DNA) using the QuantiTect
1001 Reverse Transcription Kit (Qiagen, UK) as per the manufacturers' instructions. For the
1002 Comparative C_T method, qPCR reactions were set up using 50 ng cDNA, 10 µL 2x TaqMan™
1003 Fast Advanced Master Mix (Applied Biosystems™, Fisher Scientific, UK), 1 µL 20x TaqMan™
1004 Gene Expression Assay (FAM) (Fisher Scientific, UK) (Supplementary Table 1D) and nuclease-
1005 free water. Reactions were performed in technical triplicates in MicroAmp® Fast 96-Well
1006 reaction plates (Applied Biosystems™, Fisher Scientific, UK)) and run on a StepOnePlus™ Real-
1007 Time PCR System (Fisher Scientific, UK) for 40 cycles; 20 seconds at 95°C, 1 second at 95°C, 20
1008 seconds at 60°C. Relative gene expression was analysed by the $2^{(-\Delta\Delta C_T)}$ method. GAPDH was
1009 used as housekeeping gene for normalization.

1010

1011 ***Reproducibility of experiments***

1012 RIME was performed on two independent cell cultures for each cell type, starting from freshly
1013 frozen cell stocks. For each fixed cell pellet prepared from the independent cell cultures,
1014 chromatin isolation and immunoprecipitation were then performed in technical replicates for
1015 YAP and IgG control. Control RIME was performed using isotype-matched IgG, and for each
1016 independent experiment, the two replicate IgG control immunoprecipitations were pooled for
1017 mass spectrometry analysis. For RNA-seq analysis, two independent cell cultures, starting
1018 from freshly frozen cell stocks were separately transfected with siRNA SMARTpools. For co-
1019 immunoprecipitations two to three independent experiments were performed with similar
1020 results. For immunostainings of cells, representative images from one out of three
1021 experiments are shown. Western blots are representative of at least two independent
1022 experiments. Cell cycle analysis was performed on two to four independent experiments. For

clonal growth assays at least three independent experiments were performed with three technical replicates per condition. RT-qPCR analysis was performed on three independent experiments with three technical replicates.

Statistical analysis and data presentation

Statistical analyses were performed with GraphPad Prism software (version 10.3) or R (v7.5.1). No statistical method was used to predetermine sample size. Statistical tests used to determine p-values are specified in Figure Legends. Sample size is indicated in Figure Legends, Data sets with sufficient *n* numbers were first analysed for normal distribution. In cases where the data were not found to be normally distributed, they were subsequently analysed using appropriate non-parametric tests (specified in Figure Legends), provided that the variance was comparable between the groups analysed. In some figures, superplots (139) were used to communicate both the cell-level variability and the experimental reproducibility. The investigators analysing the data were not blind to the identity of the samples. Further R (v7.5.1) data manipulation packages included genefilter (v1.86.0), dplyr (v1.1.4), tibble (v3.2.1), reshape2 (v1.4.4), plyr (v1.8.9), gage (v2.54.0), gageData (v2.42.0), and rrvgo (v1.16.0), and data were visualised in R using gplots (v3.2.0), ggplot2 (v3.5.1), viridis (v0.6.5), DOSE (v3.30.5), pheatmap (v1.0.12), RColorBrewer (v1.1-3), eulerr (7.0.2), and ggrepel (v0.9.6) packages.

References

1. Dotto GP, Rustgi AK. Squamous Cell Cancers: A Unified Perspective on Biology and Genetics. Cancer Cell. 2016;29(5):622-37.
2. Winge MCG, Kellman LN, Guo K, Tang JY, Swetter SM, Aasi SZ, et al. Advances in cutaneous squamous cell carcinoma. Nat Rev Cancer. 2023;23(7):430-49.
3. Johnson DE, Burtness B, Leemans CR, Lui VWY, Bauman JE, Grandis JR. Head and neck squamous cell carcinoma. Nat Rev Dis Primers. 2020;6(1):92.

4. Sanchez-Danes A, Blanpain C. Deciphering the cells of origin of squamous cell carcinomas. Nat Rev Cancer. 2018;18(9):549-61.
5. Flora P, Ezhkova E. Regulatory mechanisms governing epidermal stem cell function during development and homeostasis. Development. 2020;147(22).
6. Blanpain C, Fuchs E. Epidermal homeostasis: a balancing act of stem cells in the skin. Nat Rev Mol Cell Biol. 2009;10(3):207-17.
7. Yanofsky VR, Mercer SE, Phelps RG. Histopathological variants of cutaneous squamous cell carcinoma: a review. J Skin Cancer. 2011;2011:210813.
8. Lau SCM, Pan Y, Velcheti V, Wong KK. Squamous cell lung cancer: Current landscape and future therapeutic options. Cancer Cell. 2022;40(11):1279-93.
9. Hou S, Zhou S, Qin Z, Yang L, Han X, Yao S, et al. Evidence, Mechanism, and Clinical Relevance of the Transdifferentiation from Lung Adenocarcinoma to Squamous Cell Carcinoma. Am J Pathol. 2017;187(5):954-62.
10. Ratushny V, Gober MD, Hick R, Ridky TW, Seykora JT. From keratinocyte to cancer: the pathogenesis and modeling of cutaneous squamous cell carcinoma. J Clin Invest. 2012;122(2):464-72.
11. Bradner JE, Hnisz D, Young RA. Transcriptional Addiction in Cancer. Cell. 2017;168(4):629-43.
12. Franklin JM, Wu Z, Guan KL. Insights into recent findings and clinical application of YAP and TAZ in cancer. Nat Rev Cancer. 2023;23(8):512-25.
13. Piccolo S, Panciera T, Contessotto P, Cordenonsi M. YAP/TAZ as master regulators in cancer: modulation, function and therapeutic approaches. Nat Cancer. 2023;4(1):9-26.
14. Howard A, Bojko J, Flynn B, Bowen S, Jungwirth U, Walko G. Targeting the Hippo/YAP/TAZ signalling pathway: Novel opportunities for therapeutic interventions into skin cancers. Exp Dermatol. 2022;31(10):1477-99.
15. Maehama T, Nishio M, Otani J, Mak TW, Suzuki A. The role of Hippo-YAP signaling in squamous cell carcinomas. Cancer Sci. 2021;112(1):51-60.
16. Battilana G, Zanconato F, Piccolo S. Mechanisms of YAP/TAZ transcriptional control. Cell Stress. 2021;5(11):167-72.
17. Zanconato F, Battilana G, Forcato M, Filippi L, Azzolin L, Manfrin A, et al. Transcriptional addiction in cancer cells is mediated by YAP/TAZ through BRD4. Nat Med. 2018;24(10):1599-610.
18. Chang CY, Shipony Z, Lin SG, Kuo A, Xiong X, Loh KM, et al. Increased ACTL6A occupancy within mSWI/SNF chromatin remodelers drives human squamous cell carcinoma. Mol Cell. 2021;81(24):4964-78 e8.
19. Dey A, Varelas X, Guan KL. Targeting the Hippo pathway in cancer, fibrosis, wound healing and regenerative medicine. Nat Rev Drug Discov. 2020;19(7):480-94.
20. Hillmer RE, Link BA. The Roles of Hippo Signaling Transducers Yap and Taz in Chromatin Remodeling. Cells. 2019;8(5).
21. Zhang X, Tang JZ, Vergara IA, Zhang Y, Szeto P, Yang L, et al. Somatic Hypermutation of the YAP Oncogene in a Human Cutaneous Melanoma. Molecular cancer research : MCR. 2019;17(7):1435-49.
22. Bui DA, Lee W, White AE, Harper JW, Schackmann RC, Overholtzer M, et al. Cytokinesis involves a nontranscriptional function of the Hippo pathway effector YAP. Sci Signal. 2016;9(417):ra23.
23. Chow SE, Hsu CC, Yang CT, Meir YJ. YAP co-localizes with the mitotic spindle and midbody to safeguard mitotic division in lung-cancer cells. FEBS J. 2023;290(24):5704-19.
24. Melendez Garcia R, Haccard O, Chesneau A, Narassimprakash H, Roger J, Perron M, et al. A non-transcriptional function of Yap regulates the DNA replication program in Xenopus laevis. Elife. 2022;11.
25. Debaugnies M, Sanchez-Danes A, Rorive S, Raphael M, Liagre M, Parent MA, et al. YAP and TAZ are essential for basal and squamous cell carcinoma initiation. EMBO Rep. 2018.

1101 26. Zanconato F, Forcato M, Battilana G, Azzolin L, Quaranta E, Bodega B, et al. Genome-wide
1102 association between YAP/TAZ/TEAD and AP-1 at enhancers drives oncogenic growth. Nat Cell
1103 Biol. 2015;17(9):1218-27.
1104 27. Vincent-Mistiaen Z, Elbediwy A, Vanyai H, Cotton J, Stamp G, Nye E, et al. YAP drives
1105 cutaneous squamous cell carcinoma formation and progression. Elife. 2018;7.
1106 28. Omori H, Nishio M, Masuda M, Miyachi Y, Ueda F, Nakano T, et al. YAP1 is a potent driver
1107 of the onset and progression of oral squamous cell carcinoma. Sci Adv. 2020;6(12):eaay3324.
1108 29. Elbediwy A, Vincent-Mistiaen ZI, Spencer-Dene B, Stone RK, Boeing S, Wculek SK, et al.
1109 Integrin signalling regulates YAP and TAZ to control skin homeostasis. Development.
1110 2016;143(10):1674-87.
1111 30. Hanahan D, Weinberg RA. Hallmarks of cancer: the next generation. Cell.
1112 2011;144(5):646-74.
1113 31. da Costa A, Chowdhury D, Shapiro GI, D'Andrea AD, Konstantinopoulos PA. Targeting
1114 replication stress in cancer therapy. Nat Rev Drug Discov. 2023;22(1):38-58.
1115 32. Gaillard H, Garcia-Muse T, Aguilera A. Replication stress and cancer. Nat Rev Cancer.
1116 2015;15(5):276-89.
1117 33. Bowry A, Kelly RDW, Petermann E. Hypertranscription and replication stress in cancer.
1118 Trends Cancer. 2021;7(9):863-77.
1119 34. Liu S, Opiyo SO, Manthey K, Glanzer JG, Ashley AK, Amerin C, et al. Distinct roles for DNA-
1120 PK, ATM and ATR in RPA phosphorylation and checkpoint activation in response to replication
1121 stress. Nucleic Acids Res. 2012;40(21):10780-94.
1122 35. Ashley AK, Shrivastav M, Nie J, Amerin C, Troksa K, Glanzer JG, et al. DNA-PK
1123 phosphorylation of RPA32 Ser4/Ser8 regulates replication stress checkpoint activation, fork
1124 restart, homologous recombination and mitotic catastrophe. DNA Repair (Amst). 2014;21:131-9.
1125 36. Takahashi N, Kim S, Schultz CW, Rajapakse VN, Zhang Y, Redon CE, et al. Replication
1126 stress defines distinct molecular subtypes across cancers. Cancer Res Commun. 2022;2(6):503-
1127 17.
1128 37. Burrell RA, McClelland SE, Endesfelder D, Groth P, Weller MC, Shaikh N, et al. Replication
1129 stress links structural and numerical cancer chromosomal instability. Nature.
1130 2013;494(7438):492-6.
1131 38. Bartkova J, Rezaei N, Liontos M, Karakaidos P, Kletsas D, Issaeva N, et al. Oncogene-
1132 induced senescence is part of the tumorigenesis barrier imposed by DNA damage checkpoints.
1133 Nature. 2006;444(7119):633-7.
1134 39. Molinuevo R, Freije A, Contreras L, Sanz JR, Gandarillas A. The DNA damage response
1135 links human squamous proliferation with differentiation. J Cell Biol. 2020;219(11).
1136 40. Contreras L, Garcia-Gaipo L, Casar B, Gandarillas A. DNA damage signalling histone
1137 H2AX is required for tumour growth. Cell Death Discov. 2024;10(1):99.
1138 41. de Pedro I, Galan-Vidal J, Freije A, de Diego E, Gandarillas A. p21CIP1 controls the
1139 squamous differentiation response to replication stress. Oncogene. 2021;40(1):152-62.
1140 42. Freije A, Ceballos L, Coisy M, Barnes L, Rosa M, De Diego E, et al. Cyclin E drives human
1141 keratinocyte growth into differentiation. Oncogene. 2012;31(50):5180-92.
1142 43. Freije A, Molinuevo R, Ceballos L, Cagigas M, Alonso-Lecue P, Rodriguez R, et al.
1143 Inactivation of p53 in Human Keratinocytes Leads to Squamous Differentiation and Shedding via
1144 Replication Stress and Mitotic Slippage. Cell Rep. 2014;9(4):1349-60.
1145 44. Gandarillas A. The mysterious human epidermal cell cycle, or an oncogene-induced
1146 differentiation checkpoint. Cell Cycle. 2012;11(24):4507-16.
1147 45. Gandarillas A, Davies D, Blanchard JM. Normal and c-Myc-promoted human keratinocyte
1148 differentiation both occur via a novel cell cycle involving cellular growth and endoreplication.
1149 Oncogene. 2000;19(29):3278-89.

46. Li Y, Li B, Xu B, Han B, Xia H, Chen QM, et al. Expression of p53, p21(CIP1/WAF1) and eIF4E in the adjacent tissues of oral squamous cell carcinoma: establishing the molecular boundary and a cancer progression model. Int J Oral Sci. 2015;7(3):161-8.
47. Xie X, Clausen OP, Boysen M. Prognostic significance of p21WAF1/CIP1 expression in tongue squamous cell carcinomas. Arch Otolaryngol Head Neck Surg. 2002;128(8):897-902.
48. Topley GI, Okuyama R, Gonzales JG, Conti C, Dotto GP. p21(WAF1/Cip1) functions as a suppressor of malignant skin tumor formation and a determinant of keratinocyte stem-cell potential. Proc Natl Acad Sci U S A. 1999;96(16):9089-94.
49. Walko G, Woodhouse S, Pisco AO, Rognoni E, Liakath-Ali K, Lichtenberger BM, et al. A genome-wide screen identifies YAP/WBP2 interplay conferring growth advantage on human epidermal stem cells. Nat Commun. 2017;8:14744.
50. De Rosa L, Secone Seconetti A, De Santis G, Pellacani G, Hirsch T, Rothoeft T, et al. Laminin 332-Dependent YAP Dysregulation Depletes Epidermal Stem Cells in Junctional Epidermolysis Bullosa. Cell Rep. 2019;27(7):2036-49 e6.
51. Lavado A, Park JY, Pare J, Finkelstein D, Pan H, Xu B, et al. The Hippo Pathway Prevents YAP/TAZ-Driven Hypertranscription and Controls Neural Progenitor Number. Dev Cell. 2018;47(5):576-91 e8.
52. Rheinwald JG, Beckett MA. Tumorigenic keratinocyte lines requiring anchorage and fibroblast support cultured from human squamous cell carcinomas. Cancer Res. 1981;41(5):1657-63.
53. Weichselbaum R, Dahlberg W, Little JB, Ervin TJ, Miller D, Hellman S, et al. Cellular X-ray repair parameters of early passage squamous cell carcinoma lines derived from patients with known responses to radiotherapy. Br J Cancer. 1984;49(5):595-601.
54. Burns JE, Baird MC, Clark LJ, Burns PA, Edington K, Chapman C, et al. Gene mutations and increased levels of p53 protein in human squamous cell carcinomas and their cell lines. Br J Cancer. 1993;67(6):1274-84.
55. Nappi A, Miro C, Pezone A, Tramontano A, Di Cicco E, Sagliocchi S, et al. Loss of p53 activates thyroid hormone via type 2 deiodinase and enhances DNA damage. Nat Commun. 2023;14(1):1244.
56. Schlegelmilch K, Mohseni M, Kirak O, Pruszak J, Rodriguez JR, Zhou D, et al. Yap1 acts downstream of alpha-catenin to control epidermal proliferation. Cell. 2011;144(5):782-95.
57. Hassan S, Purdie KJ, Wang J, Harwood CA, Proby CM, Pourreyron C, et al. A Unique Panel of Patient-Derived Cutaneous Squamous Cell Carcinoma Cell Lines Provides a Preclinical Pathway for Therapeutic Testing. Int J Mol Sci. 2019;20(14).
58. Mohammed H, Taylor C, Brown GD, Papachristou EK, Carroll JS, D'Santos CS. Rapid immunoprecipitation mass spectrometry of endogenous proteins (RIME) for analysis of chromatin complexes. Nat Protoc. 2016;11(2):316-26.
59. De Rosa L, Secone Seconetti A, De Santis G, Pellacani G, Hirsch T, Rothoeft T, et al. Laminin 332-Dependent YAP Dysregulation Depletes Epidermal Stem Cells in Junctional Epidermolysis Bullosa. Cell Reports. 2019;27(7):2036-49.e6.
60. Szklarczyk D, Gable AL, Lyon D, Junge A, Wyder S, Huerta-Cepas J, et al. STRING v11: protein–protein association networks with increased coverage, supporting functional discovery in genome-wide experimental datasets. Nucleic acids research. 2019;47(D1):D607-D13.
61. Zhang N, Bai H, David KK, Dong J, Zheng Y, Cai J, et al. The Merlin/NF2 tumor suppressor functions through the YAP oncoprotein to regulate tissue homeostasis in mammals. Dev Cell. 2010;19(1):27-38.
62. Wang P, Bai Y, Song B, Wang Y, Liu D, Lai Y, et al. PP1A-mediated dephosphorylation positively regulates YAP2 activity. PLoS One. 2011;6(9):e24288.
63. Beltrami S, Kim R, Gordon J. Neurofibromatosis type 2 protein, NF2: an uncoventional cell cycle regulator. Anticancer Res. 2013;33(1):1-11.

64. Furukawa KT, Yamashita K, Sakurai N, Ohno S. The Epithelial Circumferential Actin Belt Regulates YAP/TAZ through Nucleocytoplasmic Shuttling of Merlin. Cell Rep. 2017;20(6):1435-47.
65. Moleirinho S, Hoxha S, Mandati V, Curtale G, Troutman S, Ehmer U, et al. Regulation of localization and function of the transcriptional co-activator YAP by angiomotin. Elife. 2017;6.
66. Li W, Cooper J, Zhou L, Yang C, Erdjument-Bromage H, Zagzag D, et al. Merlin/NF2 loss-driven tumorigenesis linked to CRL4(DCAF1)-mediated inhibition of the hippo pathway kinases Lats1 and 2 in the nucleus. Cancer Cell. 2014;26(1):48-60.
67. Amirifar P, Kissil J. The role of Motin family proteins in tumorigenesis-an update. Oncogene. 2023;42(16):1265-71.
68. Ragni CV, Diguet N, Le Garrec JF, Novotova M, Resende TP, Pop S, et al. Amotl1 mediates sequestration of the Hippo effector Yap1 downstream of Fat4 to restrict heart growth. Nat Commun. 2017;8:14582.
69. Zhou Y, Zhang J, Li H, Huang T, Wong CC, Wu F, et al. AMOTL1 enhances YAP1 stability and promotes YAP1-driven gastric oncogenesis. Oncogene. 2020;39(22):4375-89.
70. Zhu M, Peng R, Liang X, Lan Z, Tang M, Hou P, et al. P4HA2-induced prolyl hydroxylation suppresses YAP1-mediated prostate cancer cell migration, invasion, and metastasis. Oncogene. 2021;40(41):6049-56.
71. Chang L, Azzolin L, Di Biagio D, Zanconato F, Battilana G, Lucon Xiccato R, et al. The SWI/SNF complex is a mechanoregulated inhibitor of YAP and TAZ. Nature. 2018;563(7730):265-9.
72. Mittal P, Roberts CWM. The SWI/SNF complex in cancer - biology, biomarkers and therapy. Nat Rev Clin Oncol. 2020;17(7):435-48.
73. Kim M, Kim T, Johnson RL, Lim DS. Transcriptional co-repressor function of the hippo pathway transducers YAP and TAZ. Cell Rep. 2015;11(2):270-82.
74. He L, Pratt H, Gao M, Wei F, Weng Z, Struhl K. YAP and TAZ are transcriptional co-activators of AP-1 proteins and STAT3 during breast cellular transformation. Elife. 2021;10.
75. Ning B, Tilston-Lunel AM, Simonetti J, Hicks-Berthet J, Matschulat A, Pfefferkorn R, et al. Convergence of YAP/TAZ, TEAD and TP63 activity is associated with bronchial premalignant severity and progression. J Exp Clin Cancer Res. 2023;42(1):116.
76. Nowak DE, Tian B, Brasier AR. Two-step cross-linking method for identification of NF-kappaB gene network by chromatin immunoprecipitation. Biotechniques. 2005;39(5):715-25.
77. Alver RC, Chadha GS, Gillespie PJ, Blow JJ. Reversal of DDK-Mediated MCM Phosphorylation by Rif1-PP1 Regulates Replication Initiation and Replisome Stability Independently of ATR/Chk1. Cell Rep. 2017;18(10):2508-20.
78. Buonomo SB, Wu Y, Ferguson D, de Lange T. Mammalian Rif1 contributes to replication stress survival and homology-directed repair. J Cell Biol. 2009;187(3):385-98.
79. Cornacchia D, Dileep V, Quivy JP, Foti R, Tili F, Santarella-Mellwig R, et al. Mouse Rif1 is a key regulator of the replication-timing programme in mammalian cells. EMBO J. 2012;31(18):3678-90.
80. Foti R, Gnan S, Cornacchia D, Dileep V, Bulut-Karslioglu A, Diehl S, et al. Nuclear Architecture Organized by Rif1 Underpins the Replication-Timing Program. Mol Cell. 2016;61(2):260-73.
81. Hiraga SI, Ly T, Garzon J, Horejsi Z, Ohkubo YN, Endo A, et al. Human RIF1 and protein phosphatase 1 stimulate DNA replication origin licensing but suppress origin activation. EMBO Rep. 2017;18(3):403-19.
82. Mukherjee C, Tripathi V, Manolika EM, Heijink AM, Ricci G, Merzouk S, et al. RIF1 promotes replication fork protection and efficient restart to maintain genome stability. Nat Commun. 2019;10(1):3287.
83. Yamazaki S, Ishii A, Kanoh Y, Oda M, Nishito Y, Masai H. Rif1 regulates the replication timing domains on the human genome. EMBO J. 2012;31(18):3667-77.

84. Gnan S, Flyamer IM, Klein KN, Castelli E, Rapp A, Maiser A, et al. Nuclear organisation and replication timing are coupled through RIF1-PP1 interaction. Nat Commun. 2021;12(1):2910.
85. Moiseeva TN, Yin Y, Calderon MJ, Qian C, Schamus-Haynes S, Sugitani N, et al. An ATR and CHK1 kinase signaling mechanism that limits origin firing during unperturbed DNA replication. Proc Natl Acad Sci U S A. 2019;116(27):13374-83.
86. Yoshizawa-Sugata N, Yamazaki S, Mita-Yoshida K, Ono T, Nishito Y, Masai H. Loss of full-length DNA replication regulator Rif1 in two-cell embryos is associated with zygotic transcriptional activation. J Biol Chem. 2021;297(6):101367.
87. Liu C, Yu P, Ren Z, Yao F, Wang L, Hu G, et al. Rif1 Regulates Self-Renewal and Impedes Mesendodermal Differentiation of Mouse Embryonic Stem Cells. Stem Cell Rev Rep. 2023;19(5):1540-53.
88. Liu Y, Guo B, Aguilera-Jimenez E, Chu VS, Zhou J, Wu Z, et al. Chromatin Looping Shapes KLF5-Dependent Transcriptional Programs in Human Epithelial Cancers. Cancer Res. 2020;80(24):5464-77.
89. Yuan Y, Park J, Feng A, Awasthi P, Wang Z, Chen Q, et al. YAP1/TAZ-TEAD transcriptional networks maintain skin homeostasis by regulating cell proliferation and limiting KLF4 activity. Nat Commun. 2020;11(1):1472.
90. Yuan Y, Salinas Parra N, Chen Q, Iglesias-Bartolome R. Oncogenic Hedgehog-smoothened signaling depends on YAP1-TAZ/TEAD transcription to restrain differentiation in basal cell carcinoma. J Invest Dermatol. 2021.
91. Pattschull G, Walz S, Grundl M, Schwab M, Ruhl E, Baluapuri A, et al. The Myb-MuvB Complex Is Required for YAP-Dependent Transcription of Mitotic Genes. Cell Rep. 2019;27(12):3533-46 e7.
92. Jessen M, Gertzmann D, Liss F, Zenk F, Bahner L, Schoffler V, et al. Inhibition of the YAP-MMB interaction and targeting NEK2 as potential therapeutic strategies for YAP-driven cancers. Oncogene. 2024;43(8):578-93.
93. Lopez-Pajares V, Qu K, Zhang J, Webster DE, Barajas BC, Siprashvili Z, et al. A LncRNA-MAF:MAFB transcription factor network regulates epidermal differentiation. Dev Cell. 2015;32(6):693-706.
94. Kypriotou M, Huber M, Hohl D. The human epidermal differentiation complex: cornified envelope precursors, S100 proteins and the 'fused genes' family. Exp Dermatol. 2012;21(9):643-9.
95. Wang J, Harwood CA, Bailey E, Bewicke-Copley F, Anene CA, Thomson J, et al. Transcriptomic analysis of cutaneous squamous cell carcinoma reveals a multigene prognostic signature associated with metastasis. J Am Acad Dermatol. 2023;89(6):1159-66.
96. Dempster JM, Pacini C, Pantel S, Behan FM, Green T, Krill-Burger J, et al. Agreement between two large pan-cancer CRISPR-Cas9 gene dependency data sets. Nat Commun. 2019;10(1):5817.
97. Atemin A, Ivanova A, Kanev PB, Uzunova S, Nedelcheva-Veleva M, Stoynov S. Dynamics of Replication-Associated Protein Levels through the Cell Cycle. Int J Mol Sci. 2024;25(15).
98. Lebdy R, Patouillard J, Larroque M, Urbach S, Abou Merhi R, Larroque C, et al. The organizer of chromatin topology RIF1 ensures cellular resilience to DNA replication stress. Life Sci Alliance. 2023;6(4).
99. Garzon J, Ursich S, Lopes M, Hiraga SI, Donaldson AD. Human RIF1-Protein Phosphatase 1 Prevents Degradation and Breakage of Nascent DNA on Replication Stalling. Cell Rep. 2019;27(9):2558-66 e4.
100. Petermann E, Orta ML, Issaeva N, Schultz N, Helleday T. Hydroxyurea-stalled replication forks become progressively inactivated and require two different RAD51-mediated pathways for restart and repair. Mol Cell. 2010;37(4):492-502.

101. Dungrawala H, Rose KL, Bhat KP, Mohni KN, Glick GG, Couch FB, et al. The Replication Checkpoint Prevents Two Types of Fork Collapse without Regulating Replisome Stability. Mol Cell. 2015;59(6):998-1010.
102. Proby CM, Purdie KJ, Sexton CJ, Purkis P, Navsaria HA, Stables JN, et al. Spontaneous keratinocyte cell lines representing early and advanced stages of malignant transformation of the epidermis. Exp Dermatol. 2000;9(2):104-17.
103. Al-Hazmi N, Alhazzazi T, Williams G, Stoeber K, Al-Dabbagh R. DNA replication licensing factor MCM2, geminin, and Ki67 define proliferative state and are linked with survival in oral squamous cell carcinoma. Eur J Oral Sci. 2018;126(3):186-96.
104. Stojkovic-Filipovic J, Brasanac D, Bosic M, Boricic N, Lekic B. Expression of Minichromosome Maintenance Proteins in Actinic Keratosis and Squamous Cell Carcinoma. Appl Immunohistochem Mol Morphol. 2018;26(3):165-72.
105. Chandrashekar DS, Karthikeyan SK, Korla PK, Patel H, Shovon AR, Athar M, et al. UALCAN: An update to the integrated cancer data analysis platform. Neoplasia. 2022;25:18-27.
106. Zhang Y, Chen F, Chandrashekar DS, Varambally S, Creighton CJ. Proteogenomic characterization of 2002 human cancers reveals pan-cancer molecular subtypes and associated pathways. Nat Commun. 2022;13(1):2669.
107. Saladi SV, Ross K, Karaayvaz M, Tata PR, Mou H, Rajagopal J, et al. ACTL6A Is Co-Amplified with p63 in Squamous Cell Carcinoma to Drive YAP Activation, Regenerative Proliferation, and Poor Prognosis. Cancer Cell. 2017;31(1):35-49.
108. Nishio M, Hamada K, Kawahara K, Sasaki M, Noguchi F, Chiba S, et al. Cancer susceptibility and embryonic lethality in Mob1a/1b double-mutant mice. J Clin Invest. 2012;122(12):4505-18.
109. Lee JH, Kim TS, Yang TH, Koo BK, Oh SP, Lee KP, et al. A crucial role of WW45 in developing epithelial tissues in the mouse. EMBO J. 2008;27(8):1231-42.
110. Chakravarthy A, Reddin I, Henderson S, Dong C, Kirkwood N, Jeyakumar M, et al. Integrated analysis of cervical squamous cell carcinoma cohorts from three continents reveals conserved subtypes of prognostic significance. Nat Commun. 2022;13(1):5818.
111. Ghias K, Rehmani SS, Razzak SA, Madhani S, Azim MK, Ahmed R, et al. Mutational landscape of head and neck squamous cell carcinomas in a South Asian population. Genet Mol Biol. 2019;4242(3):526-42.
112. Winer D, Alsaad KO, Bray P, Smith R, Ghazarian D. Early onset cutaneous squamous cell carcinoma associated with neurofibromatosis type 2 (NF2). Eur J Dermatol. 2006;16(4):448-9.
113. Li YY, Hanna GJ, Laga AC, Haddad RI, Lorch JH, Hammerman PS. Genomic analysis of metastatic cutaneous squamous cell carcinoma. Clin Cancer Res. 2015;21(6):1447-56.
114. Shin E, Kim J. The potential role of YAP in head and neck squamous cell carcinoma. Exp Mol Med. 2020;52(8):1264-74.
115. Klein KN, Zhao PA, Lyu X, Sasaki T, Bartlett DA, Singh AM, et al. Replication timing maintains the global epigenetic state in human cells. Science. 2021;372(6540):371-8.
116. Moriyama K, Yoshizawa-Sugata N, Masai H. Oligomer formation and G-quadruplex binding by purified murine Rif1 protein, a key organizer of higher-order chromatin architecture. J Biol Chem. 2018;293(10):3607-24.
117. Cardinali M, Jakus J, Shah S, Ensley JF, Robbins KC, Yeudall WA. p21(WAF1/Cip1) retards the growth of human squamous cell carcinomas in vivo. Oral Oncol. 1998;34(3):211-8.
118. Inman GJ, Wang J, Nagano A, Alexandrov LB, Purdie KJ, Taylor RG, et al. The genomic landscape of cutaneous SCC reveals drivers and a novel azathioprine associated mutational signature. Nat Commun. 2018;9(1):3667.
119. Li Q, Tie Y, Alu A, Ma X, Shi H. Targeted therapy for head and neck cancer: signaling pathways and clinical studies. Signal Transduct Target Ther. 2023;8(1):31.
120. Wang H, Zhao A, Chen L, Zhong X, Liao J, Gao M, et al. Human RIF1 encodes an anti-apoptotic factor required for DNA repair. Carcinogenesis. 2009;30(8):1314-9.

121. Todaro GJ, Lazar GK, Green H. The initiation of cell division in a contact-inhibited mammalian cell line. J Cell Physiol. 1965;66(3):325-33.
122. Rheinwald JG, Green H. Serial cultivation of strains of human epidermal keratinocytes: the formation of keratinizing colonies from single cells. Cell. 1975;6(3):331-43.
123. Rheinwald JG. Serial cultivation of normal human epidermal keratinocytes. Methods Cell Biol. 1980;21A:229-54.
124. Ichinose Y, Iguchi H, Ohta M, Katakami H. Establishment of lung cancer cell line producing parathyroid hormone-related protein. Cancer Lett. 1993;74(1-2):119-24.
125. Uhlen M, Fagerberg L, Hallstrom BM, Lindskog C, Oksvold P, Mardinoglu A, et al. Proteomics. Tissue-based map of the human proteome. Science. 2015;347(6220):1260419.
126. Ponten F, Jirstrom K, Uhlen M. The Human Protein Atlas--a tool for pathology. J Pathol. 2008;216(4):387-93.
127. Harrison PW, Amode MR, Austine-Orimoloye O, Azov AG, Barba M, Barnes I, et al. Ensembl 2024. Nucleic Acids Res. 2024;52(D1):D891-D9.
128. Langmead B, Salzberg SL. Fast gapped-read alignment with Bowtie 2. Nat Methods. 2012;9(4):357-9.
129. Li H, Handsaker B, Wysoker A, Fennell T, Ruan J, Homer N, et al. The Sequence Alignment/Map format and SAMtools. Bioinformatics. 2009;25(16):2078-9.
130. Liao Y, Smyth GK, Shi W. featureCounts: an efficient general purpose program for assigning sequence reads to genomic features. Bioinformatics. 2014;30(7):923-30.
131. Love MI, Huber W, Anders S. Moderated estimation of fold change and dispersion for RNA-seq data with DESeq2. Genome Biol. 2014;15(12):550.
132. Subramanian A, Tamayo P, Mootha VK, Mukherjee S, Ebert BL, Gillette MA, et al. Gene set enrichment analysis: a knowledge-based approach for interpreting genome-wide expression profiles. Proc Natl Acad Sci U S A. 2005;102(43):15545-50.
133. Xu S, Hu E, Cai Y, Xie Z, Luo X, Zhan L, et al. Using clusterProfiler to characterize multiomics data. Nat Protoc. 2024;19(11):3292-320.
134. Gene Ontology C, Aleksander SA, Balhoff J, Carbon S, Cherry JM, Drabkin HJ, et al. The Gene Ontology knowledgebase in 2023. Genetics. 2023;224(1).
135. Ashburner M, Ball CA, Blake JA, Botstein D, Butler H, Cherry JM, et al. Gene ontology: tool for the unification of biology. The Gene Ontology Consortium. Nat Genet. 2000;25(1):25-9.
136. Liberzon A, Birger C, Thorvaldsdottir H, Ghandi M, Mesirov JP, Tamayo P. The Molecular Signatures Database (MSigDB) hallmark gene set collection. Cell Syst. 2015;1(6):417-25.
137. Milacic M, Beavers D, Conley P, Gong C, Gillespie M, Griss J, et al. The Reactome Pathway Knowledgebase 2024. Nucleic Acids Res. 2024;52(D1):D672-D8.
138. Hanzelmann S, Castelo R, Guinney J. GSVA: gene set variation analysis for microarray and RNA-seq data. BMC Bioinformatics. 2013;14:7.
139. Lord SJ, Velle KB, Mullins RD, Fritz-Laylin LK. SuperPlots: Communicating reproducibility and variability in cell biology. J Cell Biol. 2020;219(6).
140. Negri VA, Logtenberg MEW, Renz LM, Oules B, Walko G, Watt FM. Delta-like 1-mediated cis-inhibition of Jagged1/2 signalling inhibits differentiation of human epidermal cells in culture. Sci Rep. 2019;9(1):10825.

Figure legends

Figure 1. RIME identifies RIF1 as an interactor of chromatin-associated YAP in squamous cell carcinoma cells.

1396 (**A**) Interaction network of YAP protein interactors identified by RIME in SCC13 cells. Oval
1397 nodes indicate proteins that were previously identified as candidate regulators of SCC13 cell
1398 proliferation and/or survival in a genome wide RNA-interference (RNAi) screen (hit: 'Yes')(49),
1399 while rectangular shaped nodes indicate proteins that were not identified in the RNAi screen
1400 (hit: 'No'). Red connecting lines (edges) show previously identified YAP interactions according
1401 to the STRING Homo sapiens database, and nodes with red borders indicate known YAP
1402 interactors (manually curated from STRING and literature search); dashed red lines show
1403 manually curated known YAP interactions that were not yet present in the STRING database.
1404 Proteins were manually grouped based on function (gene names displayed, generated in
1405 Cytoscape 3.9.1 using STRING app 1.7.1). (**B**) Gene ontology terms ('molecular functions' and
1406 'biological process') enriched within the high-confidence YAP-interacting proteins identified
1407 by RIME. (**C**) Confocal fluorescence images (z-projections) of YAP (green) and RIF1 (red)
1408 nuclear localisation in SCC13 cells. DNA was counterstained with Hoechst dye DAPI (blue).
1409 Scale bar, 10 µm. (**D**, **E**) Immunoblotting analysis of YAP and IgG-control immunoprecipitates
1410 and respective inputs from SCC13 (D) whole cell extracts and (E) and nuclei-enriched fractions
1411 using the indicated antibodies. Blots from one representative experiment out of two (D) and
1412 three (E) are shown. (**F**, **G**) Representative confocal microscopy images (z-projections) and
1413 image quantifications of (F) YAP-RIF1 and (G) YAP-TEAD1 in-situ PLA in control (siNTC/shNTC)
1414 and YAP/TAZ knockdown (siYAP&TAZ/shYAP) cells (PLA signal, green; DNA (DAPI) blue; n >250
1415 cells (YAP-RIF1), n >500 cells (YAP-TEAD1) per condition in n-3 independent experiments).
1416 Scale bars, 5 µm. Datapoints show fold decrease in mean nuclear PLA signal intensity in
1417 siYAP&TAZ/shYAP cells compared to siNTC/shNTC cells. Lines show means from all three
1418 experiments, error bars show SD. Exact p-values are shown, one sample two-tailed *t* test.
1419

1420 ***Figure 2. YAP/TAZ-mediated oncogenic transcriptional programmes control the balance***
1421 ***between proliferation and differentiation in squamous cell carcinoma.***
1422 (**A**,) Significantly enriched or depleted RNAs in siYAP/TAZ SCC13 cells identified by RNA-Seq
1423 analysis using DESeq2. Volcano plot shows statistical significance (-log 10 (p-value)) versus
1424 relative RNA abundance (log2 -fold change) in siYAP/TAZ compared to siNTC cells. The vertical
1425 dotted grey lines identify the log2-fold change cut-off (0.58, 1.5-fold change). The horizontal
1426 grey dotted lines identify the cut-off for statistical significance ($p<0.05$). (**B**) Heatmaps show
1427 the log2-fold change of selected genes relating to cell cycle control, the epidermal
1428 differentiation complex, and transcriptional regulators of terminal differentiation. Black colour
1429 indicates that the gene is not differentially regulated in the pairwise comparison. (**C**)
1430 Photograph shows lack of medium acidification by doxycycline-induced shYAP SCC13 cells
1431 compared to shNTC cells during a 4-day culture period indicative of decreased proliferation.
1432 (**D**) Immunoblot analysis of SCC13 cells expressing doxycycline-induced shYAP, shTAZ, or
1433 shNTC, using the indicated antibodies. Actin and cyclophilin B (CBP) were used as loading
1434 controls. (**E**) Cell cycle analysis by propidium iodide (PI) labelling of asynchronous populations
1435 of shNTC and shYAP SCC13 cells (grey profiles) and of cells synchronised at the G1/S boundary
1436 by double thymidine block (dTb) at indicated time points. Note that the doxycycline treatment
1437 required for induction of shRNA expression slightly reduces cell proliferation (compare with
1438 Fig. 6A). One out of n=2 independent experiments is shown. (**F**) Colony formation assays were
1439 quantified by measuring the percentage of well area occupied by colonies. Bars show the
1440 means from n=3 independent experiments (performed with 3 technical replicates), individual
1441 data points show the means from each experiment, error bars show SD. Exact p-values are
1442 shown, RM one way ANOVA with Geisser-Greenhouse correction and Dunnett's multiple

1443 comparison test. (**G**) Immunoblot analysis of shNTC, shYAP, and shTAZ SCC13 cells using the
1444 indicated antibodies. Tubulin was used as loading control.
1445
1446 ***Figure 3. YAP modulates RIF1 transcription and promotes RIF1 protein stability.***
1447 (**A**,) Significantly enriched or depleted RNAs in siRIF1 SCC13 cells identified by RNA-Seq
1448 analysis using DESeq2. Volcano plot shows statistical significance (-log 10 (p-value)) versus
1449 relative RNA abundance (log2 -fold change) in siRIF1 compared to siNTC cells. The vertical
1450 dotted grey lines identify the log2-fold change cut-off (0.58, 1.5-fold change). The horizontal
1451 grey dotted lines identify the cut-off for statistical significance ($p<0.05$). (**B**) Scatter plot shows
1452 correlations between the 710 genes that were found to be differentially expressed in both
1453 siYAP/TAZ and siRIF1 SCC13 cell datasets. (**C**) qRT-PCR analysis of *RIF1* mRNA expression in
1454 SCC13 cells transfected with an siRNA SMARTpool targeting YAP/TAZ (siY/T) or siNTC. Data
1455 shown are from n=3 independent experiments performed with three technical replicates.
1456 Individual data points represent the mean fold change in mRNA abundance (normalized to
1457 GAPDH) compared to siNTC in each experiment. Bars represent the means from all
1458 experiments, error bars represent SD. Exact p-values are shown, paired *t* test. (**D**, **E**)
1459 Immunoblot analysis of SCC13 cells transfected with (D) an siRNA SMARTpool targeting
1460 YAP/TAZ (siY/T) or an siNTC SMARTpool or (E) expressing doxycycline-induced shYAP, shTAZ or
1461 shNTC, using the indicated antibodies. Tubulin or cyclophilin B (CBP) were used as loading
1462 controls. In (D) numbers below lanes represent protein ratios relative to an arbitrary level of
1463 1.0 set for siNTC. (**F**) Quantification of RIF1 protein expression as shown in (E). Individual data
1464 points show fold change in RIF1 protein levels (normalised to tubulin) in shYAP compared to
1465 shNTC in n=3 different experiments, bars show the mean, error bars show SD. (**G**) Log2-fold
1466 change in *YAP1* and *RIF1* mRNA abundances (based on RNA-seq analysis performed in (89)) in

1467 N/TERT-2G immortalised NHKs transfected with YAP/TAZ-targeting siRNAs (siY/T) compared
1468 N/TERT-2G cells transfected with siNTC. (**H**) Correlation analysis between the single sample
1469 GSEA scores for the MSigDB GO:Hippo_Signalling gene set and *RIF1* mRNA expression levels
1470 (batch corrected, 24Q2 release) in a panel of 64 HNSCC cell lines. Spearman correlation
1471 coefficient and statistical significance are indicated. (**I**) Immunoblot analysis and quantification
1472 of RIF1 protein levels in SCC13 cells transfected with siRNA SMARTpools targeting TEAD1,
1473 TEAD3, TEAD4, or YAP/TAZ (siY/T), or an siNTC SMARTpool. Cyclophilin B (CBP) was used as
1474 loading control. Quantification of RIF1 protein expression was done as in (F). (**J**) Immunoblot
1475 analysis, using the indicated antibodies, of SCC13 cells expressing a doxycycline-induced shYAP
1476 or a shNTC, treated for the indicated times with cycloheximide (CHX, 100 µg/ml). Cyclophilin
1477 B (CBP) was used as loading control.
1478
1479 ***Figure 4. Increased association of YAP with RIF1 in response to replication stress.***
1480 (**A**) Immunoblot analysis of chromatin fractions from SCC13 cells expressing a doxycycline-
1481 induced shYAP or shNTC, using the indicated antibodies. Cells were synchronised at the G1/S
1482 boundary by double thymidine block (dTB) and released into the S phase. Samples were taken
1483 at the indicated timepoints. Histone H3 (HH3) was used as loading control. Blots from one
1484 representative experiment out of two are shown. (**B**, **C**) Representative confocal microscopy
1485 images of (B) z-projection and (C); orthogonal projection of YAP-RIF1 in-situ PLA in SCC13 cells
1486 (PLA signal, green; DNA (DAPI) blue). In (B) cells were labelled with a 1-hour EdU pulse prior
1487 to fixation (EdU signal, red). Arrows in (C) indicate cells completing mitosis. Scale bars, 5 µm.
1488 (**D**) Immunoblot analysis of SCC13 control cells and cells exposed to 4 mM hydroxyurea (HU)
1489 for 24 hours, using the indicated antibodies. Washout, medium removal and replacement with
1490 fresh medium. Tubulin and cyclophilin B (CBP) were used as loading controls. (**E**, **F**) Image

1491 quantifications of (E) YAP-RIF1 and (F) YAP-γH2AX in-situ PLA in SCC13 cells treated with 4 mM
1492 HU for the indicated times. >200 cells were measured per experimental condition in n=3
1493 independent experiments. Superplots show nuclear PLA signal intensity per cell (grey
1494 datapoints), mean nuclear PLA signal intensity of the respective cell populations in each of
1495 n=3 experiments (black datapoints), and mean nuclear PLA signal intensity from all three
1496 experiments (lines). Error bars show SD from all three experiments. Exact p-values are shown.
1497 (E) Brown-Forsythe and Welsh ANOVA test with Dunett's multiple comparison test, (F)
1498 unpaired *t* test.
1499
1500 ***Figure 5. Increased expression of RIF1 in squamous cell carcinoma.***
1501 (**A**) Immunoblot analysis of normal human epidermal keratinocytes (NHKs), keratinocytes
1502 isolated from a pre-malignant dysplastic skin lesion (PM1), various cell lines isolated from
1503 primary cutaneous SCCs (cSCC; SCC13, SCC-NR, MET1), a recurrent cSCC (MET2), and a lymph
1504 node metastasis (MET4), using the indicated antibodies. Actin was used as loading control. (**B**,
1505 **C**) Quantification (B) and representative images (C) of RIF1 expression in healthy adult human
1506 skin (HS), nodular (Nod) and (Inf) infiltrative basal cell carcinoma (BCC), and well-differentiated
1507 (WD) and poorly differentiated (PD) cSCC. Tissue sections were immunolabelled with
1508 antibodies against RIF1 (green), and keratin 14 (Krt14, blue) to identify normal and neoplastic
1509 epidermal keratinocytes. White dotted line demarcates dermal–epidermal boundary in HS.
1510 Scale bar, 50 µm. Superplots in (B) show percentage of RIF1-positive keratinocytes in different
1511 areas of the same tumour (coloured symbols), mean percentage of RIF1-positive keratinocytes
1512 in 3–5 different patient samples (black datapoints), and mean percentage of RIF1-positive
1513 keratinocytes in each sample group (lines). Error bars show SD from each sample group.
1514 *$p < 0.05$, Brown-Forsythe and Welsh ANOVA test with Dunett's multiple comparison test. (**D**,

1515 **E**) RIF1 protein expression in HNSCC samples from the Clinical Proteomic Tumour Analysis
1516 Consortium (CPTAC), stratified according to (D) tumour stage, or (E) presence of alterations
1517 in the Hippo pathway or other signalling pathways. Jitter plots (overlayed onto box plots) show
1518 Z-values (standard deviations from the median across samples for the given sample type) from
1519 individual samples. Box plots indicate the median (middle line), 25th percentile (bottom line),
1520 75th percentile (top line), and minimum and maximum (whiskers). Log2 spectral count ratio
1521 values from CPTAC were first normalized within each sample profile, then normalized across
1522 samples. Graphs were downloaded from the UALCAN database
1523 (https://ualcan.path.uab.edu/). (D) $p < 0.05$ for all pairwise comparisons, ANOVA test with
1524 Dunett's multiple comparison test. In (E) exact p-values are shown.
1525
1526 ***Figure 6. Depletion of RIF1 in squamous cell carcinoma cells affect DNA replication dynamics.***
1527 (**A**) Cell cycle analysis by PI labelling of asynchronous populations of shNTC and shRIF1 (shRIF1-
1528 017, see (B)) SCC13 cells (grey profiles) and of cells synchronised at the G1/S boundary by
1529 double thymidine block (dTb) and released into S-phase (T=hours post thymidine release,
1530 coloured profiles). One of n=2 experiments is shown. (**B**, **C**) Immunoblot analysis of (B) cell
1531 extracts and (C) chromatin fractions from shNTC and shRIF1 SCC13 cells, using the indicated
1532 antibodies. In (C) cells were synchronised at the G1/S boundary by double thymidine block
1533 (dTB) and released into the S phase. Samples were taken at the indicated timepoints. Note
1534 that DDK-induced phosphorylation of MCM4 results in a band shift. Cyclophilin B (CPB),
1535 tubulin, and histone H3 (HH3) were used as loading controls. shRIF1-017 was used in
1536 experiments shown in (A, C).
1537
1538 ***Figure 7. RIF1 protects against endogenous and exogenous replication stress.***

1539 (**A**) Immunoblott analysis of cell extracts from SCC13 cells expressing shNTC or different
1540 shRIF1, using the indicated antibodies. Cyclophilin B (CPB), and tubulin were used as loading
1541 controls. Cells treated for 24 hours with 4 mM HU served as positive controls for severe
1542 replication stress. The position of the RPA32 band is indicated with an arrow. (**B**)
1543 Representative cell cycle profile (PI labelling following a 30-minute EdU pulse) of
1544 unsynchronised shNTC and shRIF1 SCC13 cells. Gates used for quantification and percentages
1545 of cells in different cell cycle phases are indicated. One out of n=4 independent experiments
1546 is shown. (**C**) Immunoblot analysis of cell extracts from SCC13 cells expressing shNTC or
1547 different shRIF1, using the indicated antibodies. Tubulin was used as loading control. (**D**)
1548 Representative images of colony formation efficiency of shNTC and shRIF1 SCC13 cells. Cells
1549 in triplicate wells were stained with crystal violet. Colony formation assays were quantified by
1550 measuring the percentage of well area occupied by colonies. Bars show the means from n=3
1551 independent experiments (performed with 3 technical replicates), individual data points show
1552 the means from each experiment, error bars show SD. Exact p-values are shown, RM one way
1553 ANOVA with Geisser-Greenhouse correction and Dunnett's multiple comparison test. (**E, F**)
1554 Synergism of YAP depletion (shYAP) and HU treatment on clonal colony growth was quantified
1555 by measuring the percentage of well area occupied by colonies after 10 days in culture. In (F)
1556 values have been normalized to controls (no HU treatment) for shYPA and shNTC. Bars show
1557 the means from n=3 independent experiments (performed with 3 technical replicates),
1558 individual data points show the means from each experiment, error bars show SD. p-values
1559 are shown for multiple comparisons, RM two-way ANOVA with Geisser-Greenhouse
1560 correction (matched values both stacked and spread across rows) and Šidak's multiple
1561 comparison test. *p<0.05, **p<0.01, ***p<0.001. Sources of variation in (E): HU
1562 concentration, p=0.04; shRNA, p=0.002; HU concentration x shRNA, p<0.001. Sources of

1563 variation in (F): HU concentration, p=0.008; shRNA, p=0.02; HU concentration x shRNA,
1564 p=0.007.
1565
1566 ***Supplementary Figure 1. Validation of YAP antibody and cell culture conditions for RIME.***
1567 (**A**) Immunoblot analysis of cell extracts from SCC13 cells expressing a non-targeting control
1568 shRNA (shNTC), two different shRNAs targeting YAP (shYAP-1, shYAP-2), or two different
1569 shRNAs targeting TAZ (shTAZ-1, shTAZ-2) using the indicated antibodies. Note that the rabbit
1570 anti-human YAP antibody used for RIME (Y1200-01D, US Biologicals) did not recognize TAZ.
1571 Tubulin was used as loading control. (**B**) Representative wide-field microscopy images of
1572 YAP/TAZ (monoclonal anti-YAP/TAZ antibody, clone 63.7, Santa Cruz) nuclear localisation in
1573 NHK and SCC13 cells prior to RIME experiments. F-actin was counterstained with phalloidin.
1574 Scale bar, 100 µm. (**C**) Coverage of bait protein YAP across both experiments and all technical
1575 replicates. Regions shown in blue represent peptides detected by mass spectrometry. Km5 =
1576 NHK cells, strain km, passage 5.
1577
1578 ***Supplementary Figure 2. RIME identifies RIF1 as an interactor of chromatin-associated YAP***
1579 ***in normal human keratinocytes.***
1580 (**A**) Interaction network of YAP protein interactors identified by RIME in NHKs. Red connecting
1581 lines (edges) show previously identified YAP interactions according to the STRING Homo
1582 sapiens database, and nodes with red borders indicate known YAP interactors (manually
1583 curated from STRING and literature search); dashed red lines show manually curated known
1584 YAP interactions that were not yet present in the STRING database. Proteins were manually
1585 grouped based on function (gene names displayed, generated in Cytoscape 3.9.1 using STRING
1586 app 1.7.1). (**B**) Gene ontology terms ('molecular functions' and 'biological process') enriched

1587 within the high-confidence YAP-interacting proteins identified by RIME in NHKs. (**C**) Mean
1588 spectral counts (total number of identified peptide spectra per protein) for YAP and RIF1 in
1589 the YAP-RIME from the two independently performed experiments in SCC13 and NHK cells.
1590 (**D**) Immunoblot analysis of chromatin fractions from NHK and SCC13 cells, using the indicated
1591 antibodies. Similar amounts of total chromatin-associated proteins were loaded on SDS-PAGE,
1592 as validated by Coomassie staining.
1593
1594 ***Supplementary Figure 3. Validation of YAP/TAZ knockdown efficiency and antibody***
1595 ***specificity for in-situ PLA experiments, and confirmation of YAP-RIF1 interaction in HARA***
1596 ***lung squamous cell carcinoma cells.***
1597 (**A**) Immunoblott analysis of YAP (rabbit monoclonal anti-YAP antibody; D8H1X, Cell Signalling))
1598 and IgG-control immunoprecipitates and respective inputs from SCC13 cell extracts using the
1599 indicated antibodies. (**B**) Immunoblot analysis of lysates from cells used in in-situ PLA
1600 experiments shown in Fig. 1F and 1G. To achieve the strongest YAP/TAZ depletion possible,
1601 SCC13 cells expressing inducible shNTC or shYAP were treated with doxycycline for 72 hours
1602 and were in parallel also transfected with non-targeting control or YAP/TAZ-targeting siRNA
1603 SMARTpools, respectively. Tubulin was used as loading control. (**C**, **D**) Representative confocal
1604 microscopy images (z-projections) of in-situ PLA (PLA signal, green; DNA (DAPI)) blue) in cells
1605 labelled with (C) no primary antibodies or (D) only one of the two primary antibodies. Scale
1606 bars, 5 µm. (**E**) Representative confocal microscopy images (z-projections) of YAP-RIF1 in-situ
1607 PLA (PLA signal, green; DNA (DAPI)) blue in miotic cells. Scale bars, 5 µm. (**F**) Confocal
1608 fluorescence image (z-projection) of YAP (green) and RIF1 (red) nuclear localisation in HARA
1609 cells. DNA was counterstained with Hoechst dye (DAPI, blue). Scale bar, 10 µm. (**G**)
1610 Immunoblot analysis of YAP and IgG-control immunoprecipitates and respective inputs from

1611 HARA cell nuclei-enriched fractions (treated with Benzonase® nuclease) using the indicated
1612 antibodies. (**H**) Agarose gel electrophoresis of DNA extracts from Benzonase®-treated and
1613 untreated HARA cells shows efficient DNA degradation upon Benzonase® treatment. Left lane:
1614 Thermo Scientific™ GeneRuler 1 kb Plus DNA Ladder (Fisher, UK).
1615
1616 ***Supplementary Figure 4. Gene set enrichment analysis in differentially expressed genes***
1617 ***upon YAP/TAZ knockdown in SCC13 cells.***
1618 (**A**, **B**) Bubble plots show results of gene set enrichment analysis (GSEA) on RNA-seq data from
1619 siYAP/TAZ SCC13 cells. The top 10 downregulated (suppressed) or upregulated (activated)
1620 pathways in siYAP/TAZ SCC13 cells are shown. (**C**) Heatmaps show the log2-fold change of
1621 selected genes representing high confidence YAP/TAZ-TEAD target genes, YAP-MMB target
1622 genes, and genes directly involved in DNA replication, in the indicated pairwise comparisons.
1623 Black colour indicates that the gene is not differentially regulated in that pairwise comparison.
1624 (**D**) GSEA showing enrichment of epidermal late differentiation (upper panel) and progenitor
1625 cell (lower panel) signatures (93) among the differentially expressed genes in siYAP/TAZ (siY/T)
1626 versus siNTC SCC13 cells.
1627
1628 ***Supplementary Figure 5. Correlation analysis of YAP/TAZ target genes, replication stress-***
1629 ***associated genes, and RIF1 in HNSCC cell lines.***
1630 (**A**–**C**) Correlation heatmaps of the indicated genes (mean mRNA expression) distinguished by
1631 (A, C) 64 HNSCC or (B) 5 cSCC cell lines. Graphs were exported from the DepMap portal. (**D**–
1632 **F**) Correlation analysis between the expression of replication stress-associated genes and (D)
1633 YAP/TAZ target genes or (E) *RIF1* mRNA expression levels (expression public 24Q2 release),
1634 and (F) correlation of YAP/TAZ target genes and *RIF1* mRNA expression levels in a panel of 64

HNSCC cell lines. Spearman correlation coefficient and statistical significance are indicated. Data were accessed using the DepMap portal (https://depmap.org/portal/).

Supplementary Figure 6. Cell cycle withdrawal and terminal differentiation commitment of SCC cells upon conditional YAP depletion are reversible.

Phase contrast images show morphological appearance of shNTC and shYAP SCC13 cells growing in the presence of doxycycline (dox), and at the indicated timepoint after doxycycline withdrawal. Note reduced density, impaired colony formation, and elongated and flattened shape (indicative of terminal differentiation (140)) of shYAP cells in the presence of doxycycline, and rapid recovery of normal cell morphology and growth behaviour upon doxycycline withdrawal leading to re-expression of YAP.

Supplementary Figure 7. Involvement of YAP/TAZ target genes in human cSCC progression.

Boxplots show the distribution of Gene Set Variation Analysis (GSVA) scores for differentially expressed genes (DEGs) that were (**A**) downregulated or (**B**) upregulated in siYAP/TAZ SCC13 cells across different cSCC patient samples (95). Norm_no_met / tum_no_met: perilesional normal skin and primary cSCC tissue from patients with no metastasis over 3 years; norm_with_met / tum_with_met: perilesional normal skin and primary cSCC tissue from patients with metastasis during 3 years follow-up; met: tissue from metastasis. Pairwise comparisons between sample groups were conducted using a *t* test. The p-values from these comparisons are indicated above the boxplots with brackets linking the compared groups. The significance levels are denoted as follows: *: p <= 0.05; **: p <= 0.01; ***: p <= 0.001; ****: p <= 0.0001.

1659 ***Supplementary Figure 8. Gene set enrichment analysis in differentially expressed genes***
1660 ***upon RIF1 knockdown in SCC13 cells.***
1661 (**A**–**C**) Bubble plots show results of gene set enrichment analysis (GSEA) on RNA-seq data from
1662 siRIF1 SCC13 cells. The top 10 downregulated (suppressed) or upregulated (activated)
1663 pathways in siRIF1 SCC13 cells are shown.
1664
1665 ***Supplementary Figure 9. RIF1 expression in different types of squamous cancers.***
1666 (**A**–**C**) Representative RIF1 immunohistochemistry (anti-RIF1 rabbit polyclonal antibody
1667 HPA036887, Atlas Antibodies) of normal tissue and squamous cell carcinoma tissue from (A)
1668 skin, (B) oral cavity and (C) cervix, exported from the Human Protein Atlas database. NS,
1669 normal skin; cSCC-IS, cutaneous squamous cell carcinoma in-situ; WD cSCC, well differentiated
1670 cSCC; PD cSCC, poorly differentiated cSCC; NOM, normal oral mucosa; WD OSCC, well
1671 differentiated oral SCC; PD, poorly differentiated oral SCC; NC, normal cervix; CeSCC, cervical
1672 SCC. (**D**) RIF1 protein expression across different cancers, with tumour and normal samples,
1673 from the Clinical Proteomic Tumour Analysis Consortium (CPTAC). Box plots indicate median
1674 Z-values (middle line), 25th percentile (bottom line), 75th percentile (top line), and minimum
1675 and maximum (whiskers). Log2 spectral count ratio values from CPTAC were first normalized
1676 within each sample profile, then normalized across samples. Graphs were downloaded from
1677 the UALCAN database (https://ualcan.path.uab.edu/). BRCA, breast cancer (18 normal and
1678 125 tumour samples); COAD, colon adenocarcinoma (100 normal and 97 tumour samples);
1679 OV, ovarian serous cystadenocarcinoma (25 normal and 100 tumour samples); KIRC, kidney
1680 renal clear cell carcinoma (84 normal and 110 tumour samples); UCEC, uterine corpus
1681 endometrial carcinoma (31 normal and 100 tumour samples); LUAD, lung adenocarcinoma
1682 (111 normal and 111 tumour samples); PAAD, pancreatic adenocarcinoma (74 normal and

1683 137 tumour samples); HNSCC, head and neck squamous cell carcinoma (71 normal and 108
1684 tumour samples); GBM, glioblastoma multiforme (10 normal and 99 tumour samples); LIHC,
1685 liver hepatocellular carcinoma (165 normal and 165 tumour samples). (**E**–**G**) RIF1 protein
1686 expression in (E) lung SCC, (F) GMB, and (G) OV samples from the Clinical Proteomic Tumour
1687 Analysis Consortium (CPTAC), stratified according to presence of alterations in the Hippo
1688 pathway or other signalling pathways. Jitter plots (overlayed onto box plots) show Z-values
1689 (standard deviations from the median across samples for the given sample type) from
1690 individual samples. Box plots indicate the median (middle line), 25th percentile (bottom line),
1691 75th percentile (top line), and minimum and maximum (whiskers). Log2 spectral count ratio
1692 values from CPTAC were first normalized within each sample profile, then normalized across
1693 samples. Graphs were downloaded from the UALCAN database
1694 (https://ualcan.path.uab.edu/). Exact p-values are shown.

1695

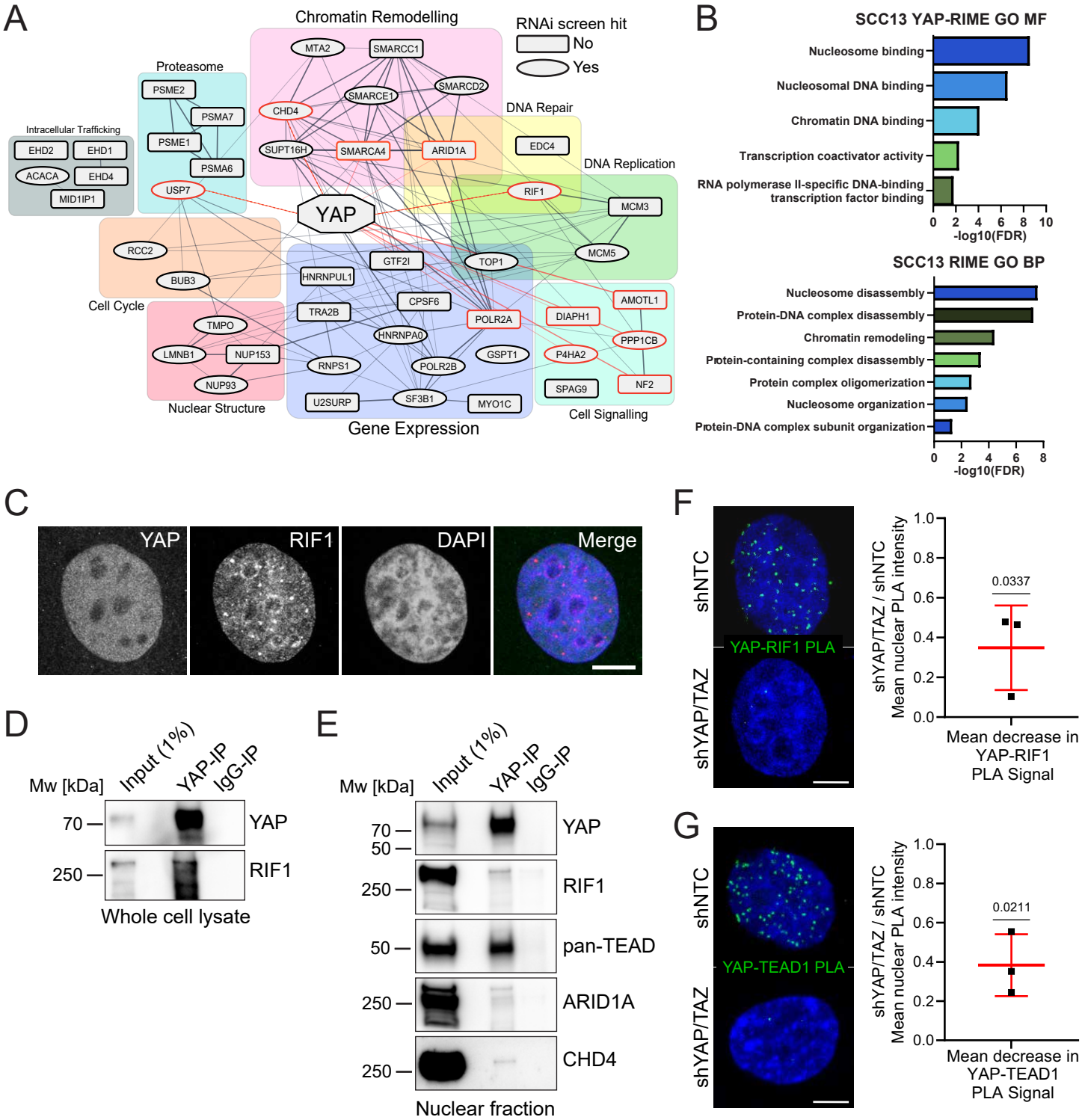

Figure 1_Bojko et al.

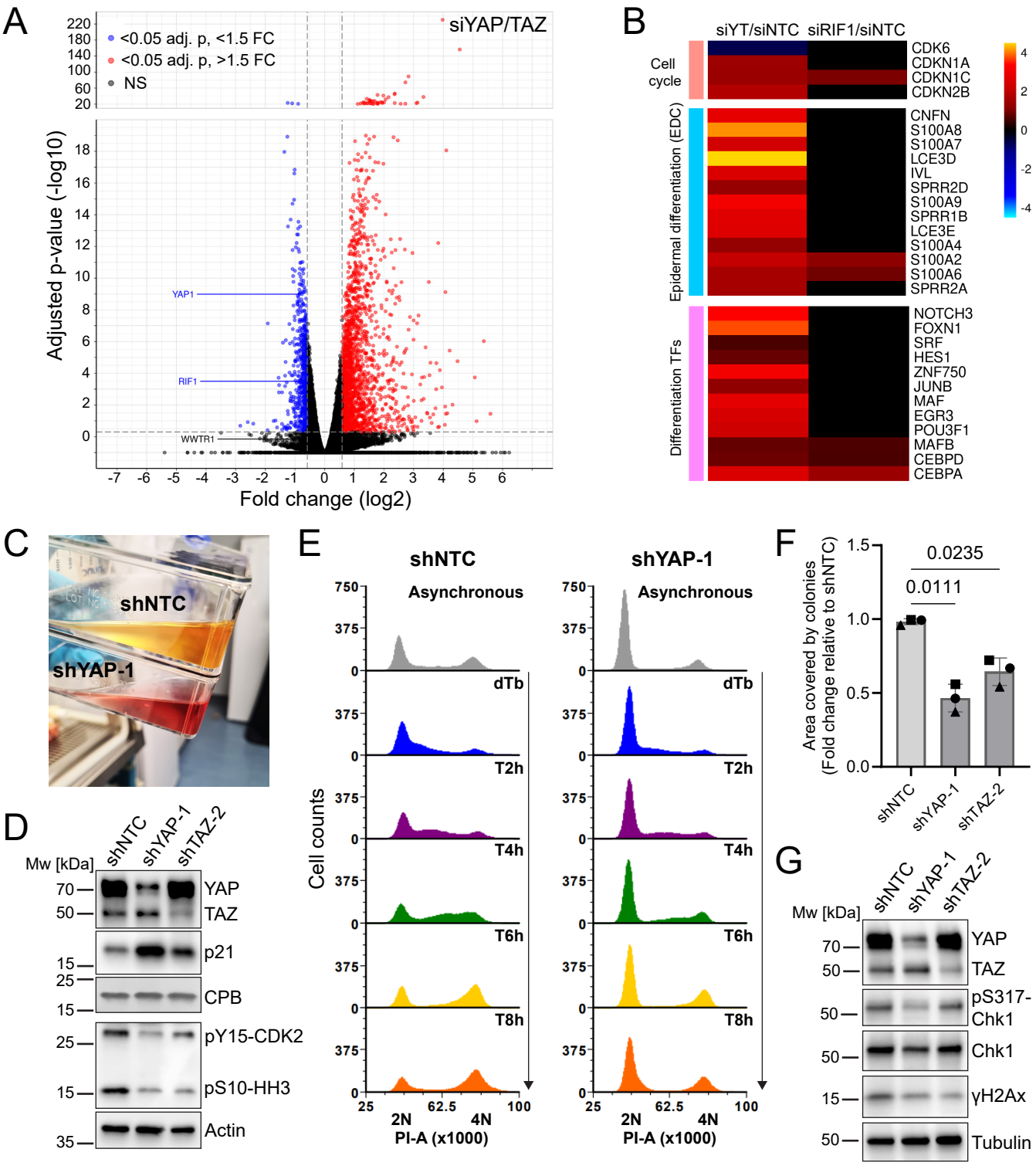

Figure 2_Bojko et al.

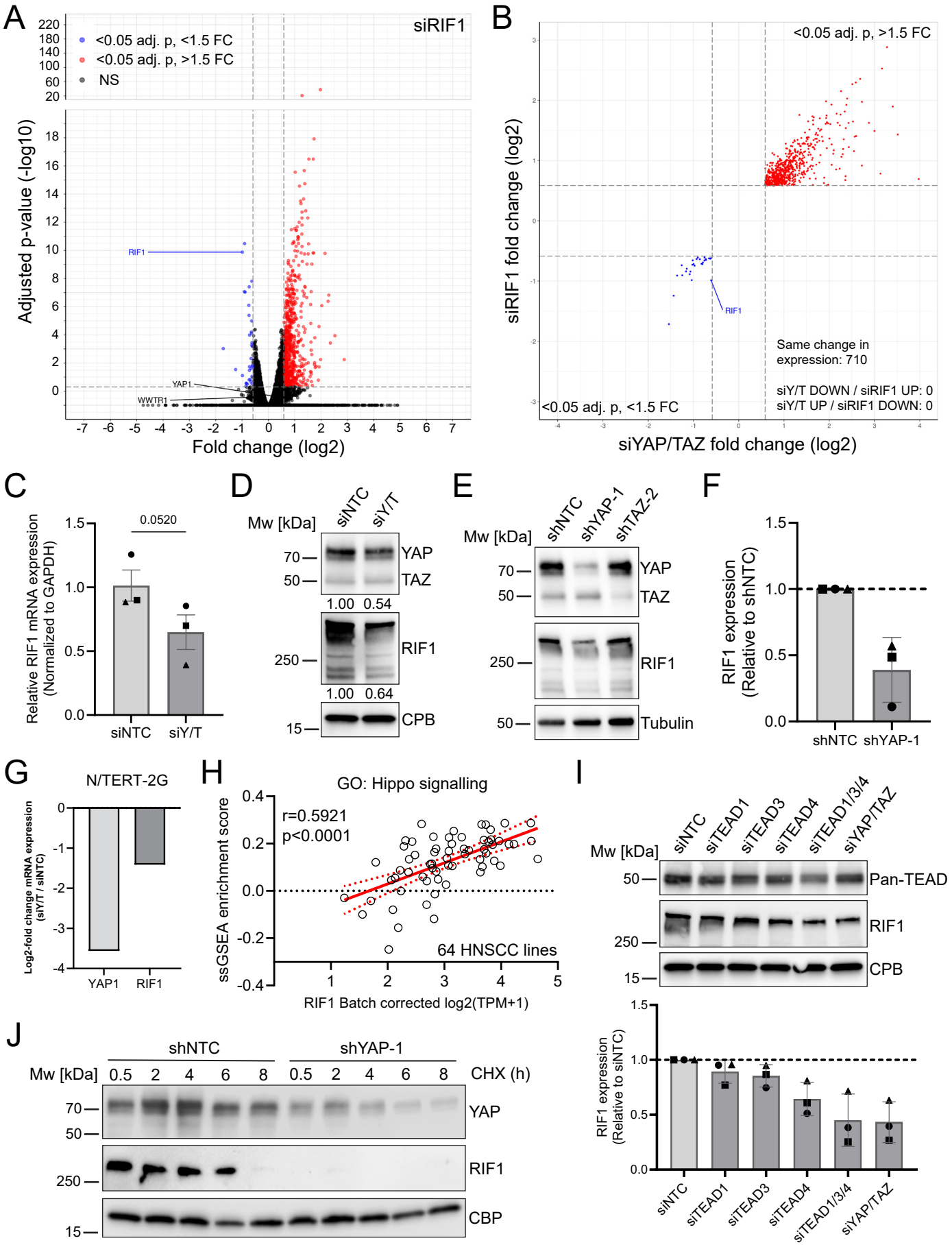

Figure 3_Bojko et al.

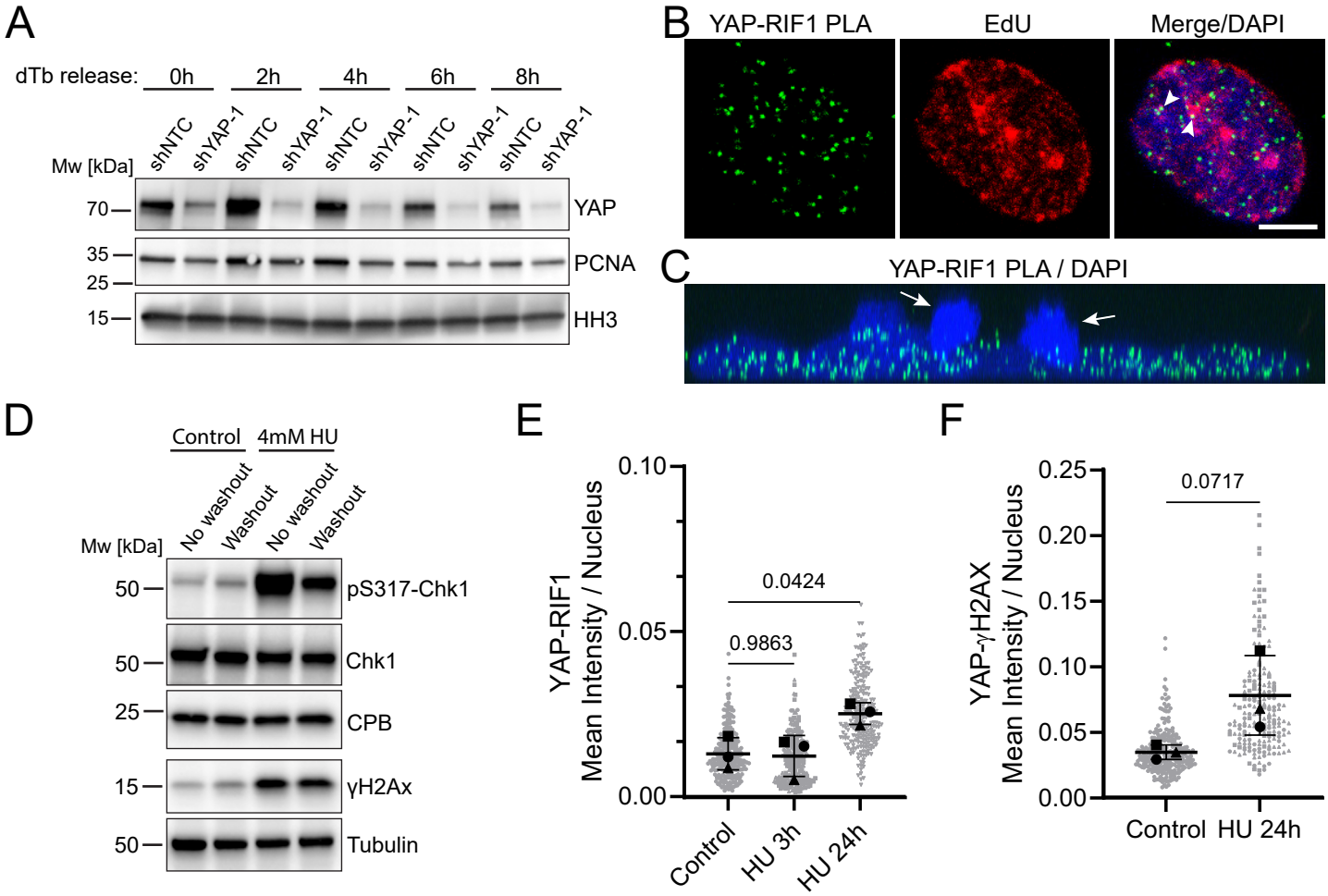

Figure 4_Bojko et al.

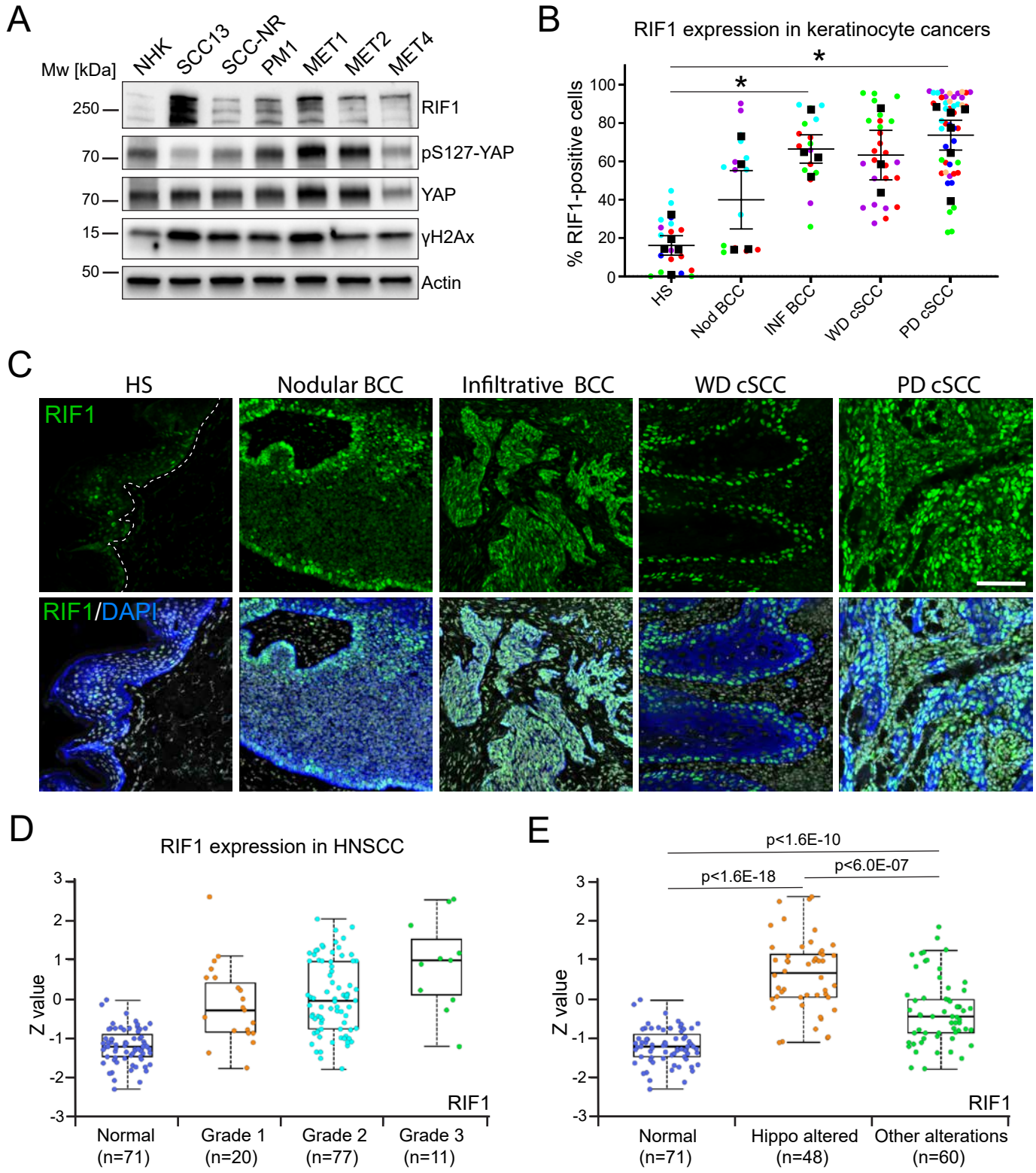

Figure 5_Bojko et al.

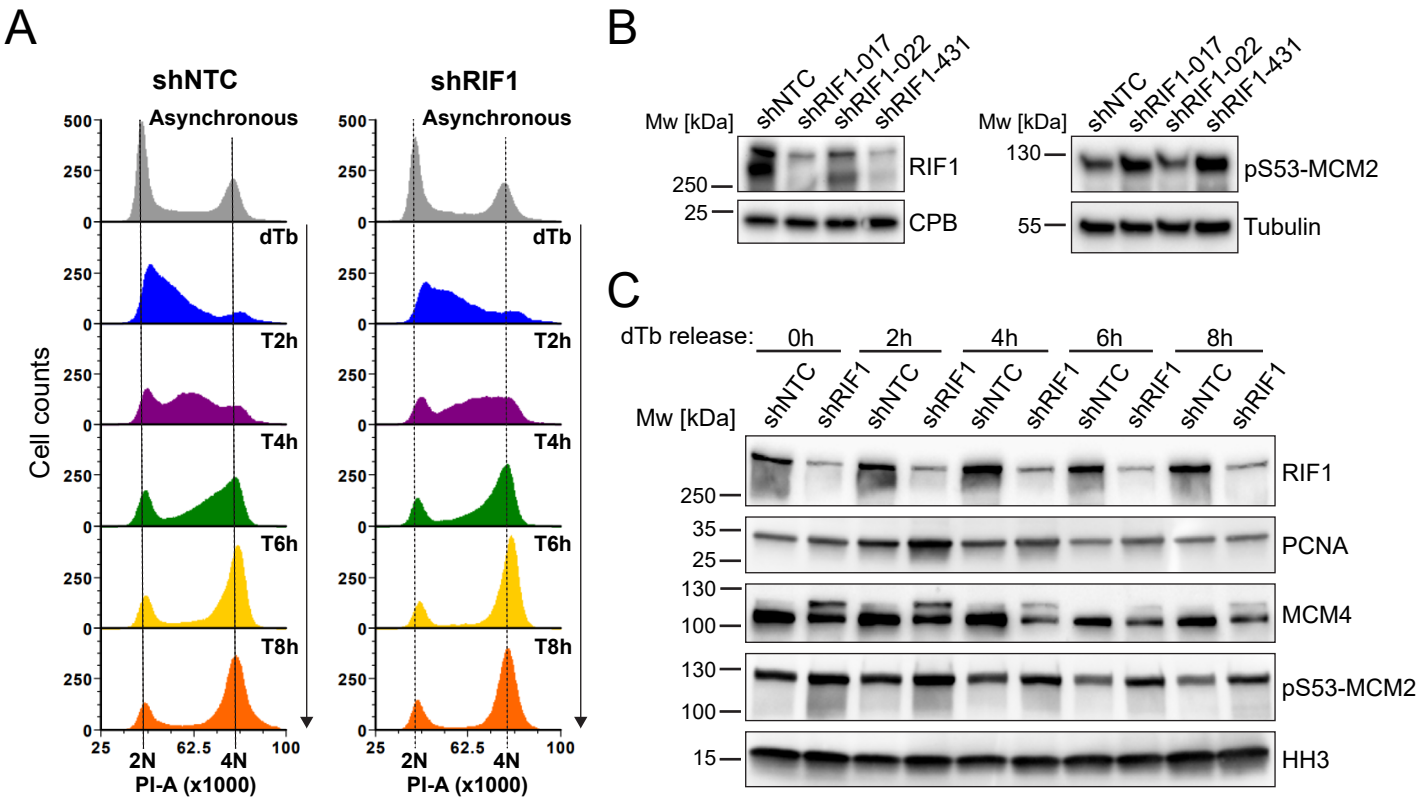

Figure 6_Bojko et al.

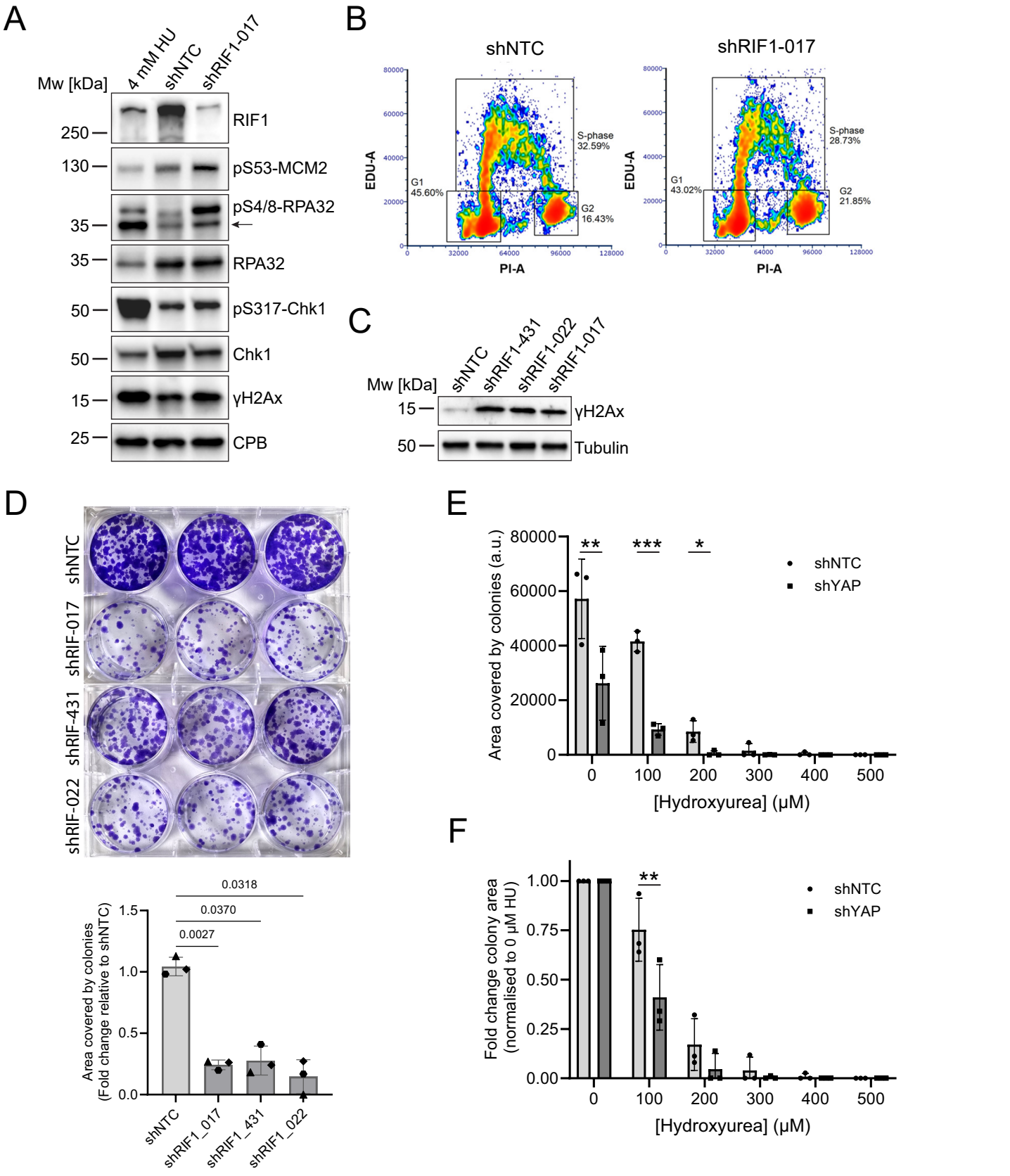

Figure 7_Bojko et al.

A

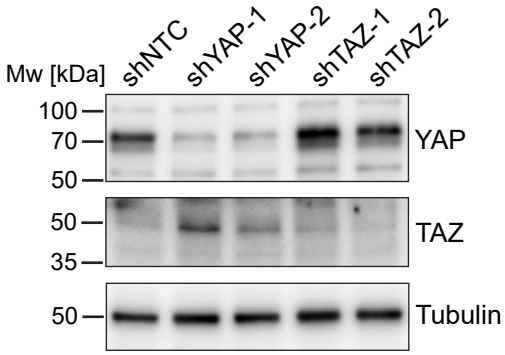

B

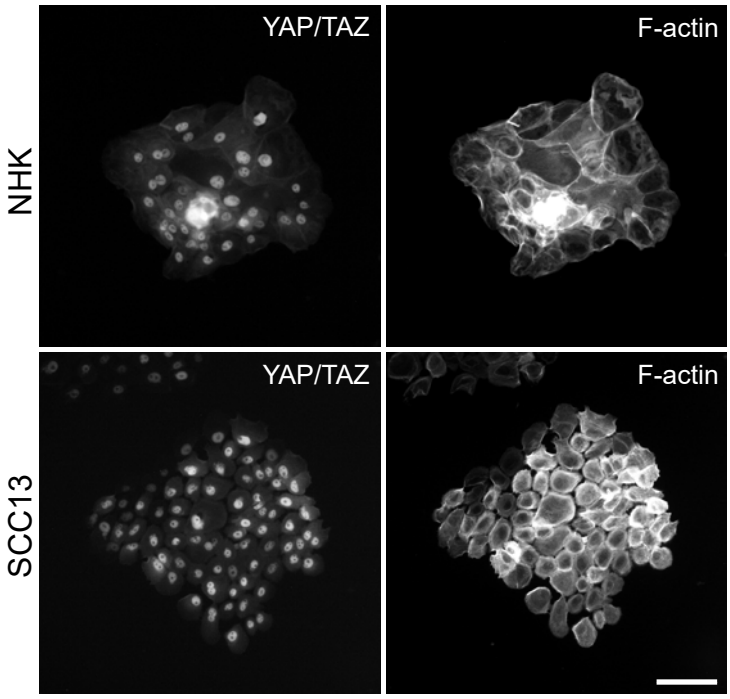

C

Accession	Description	Coverage	#Spec	Sample
P46937	Transcriptional coactivator YAP1...	60%	40	1Km5_Exp1_R1
P46937	Transcriptional coactivator YAP1...	60%	31	1Km5_Exp1_R2
P46937	Transcriptional coactivator YAP1...	63%	52	2SCC13_Exp1_R1
P46937	Transcriptional coactivator YAP1...	63%	48	2SCC13_Exp1_R2
P46937	Transcriptional coactivator YAP1...	60%	38	3Km5_Exp2_R1
P46937	Transcriptional coactivator YAP1...	65%	49	3Km5_Exp2_R2
P46937	Transcriptional coactivator YAP1...	65%	51	4SCC13_Exp2_R1
P46937	Transcriptional coactivator YAP1...	63%	48	4SCC13_Exp2_R2

Figure S1_Bojko et al.

A

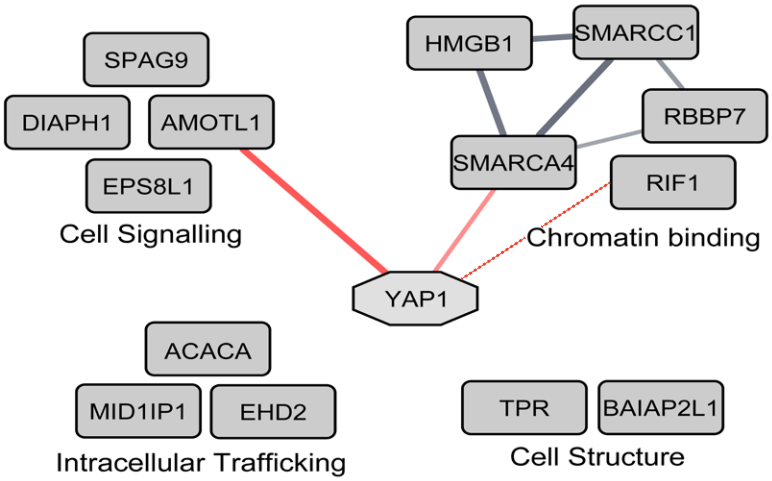

B

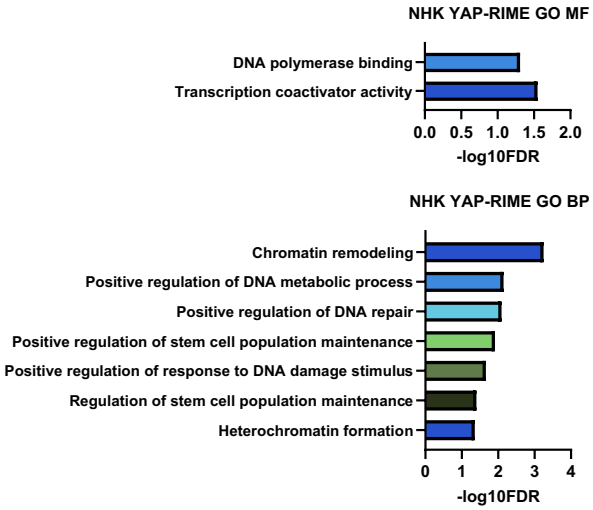

C

	YAP-IP_EXP1_mean spectral counts	YAP-IP_EXP2_mean spectral counts
SCC13	72.5	47.5
NHK	15.5	17

D

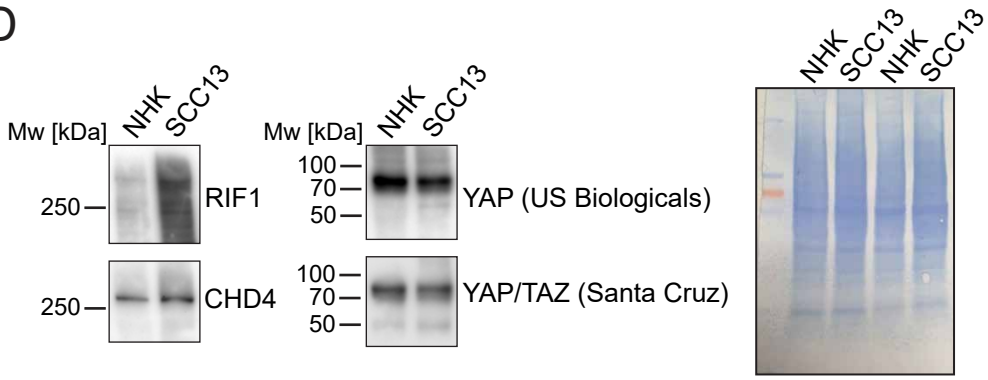

Figure S2_Bojko et al.

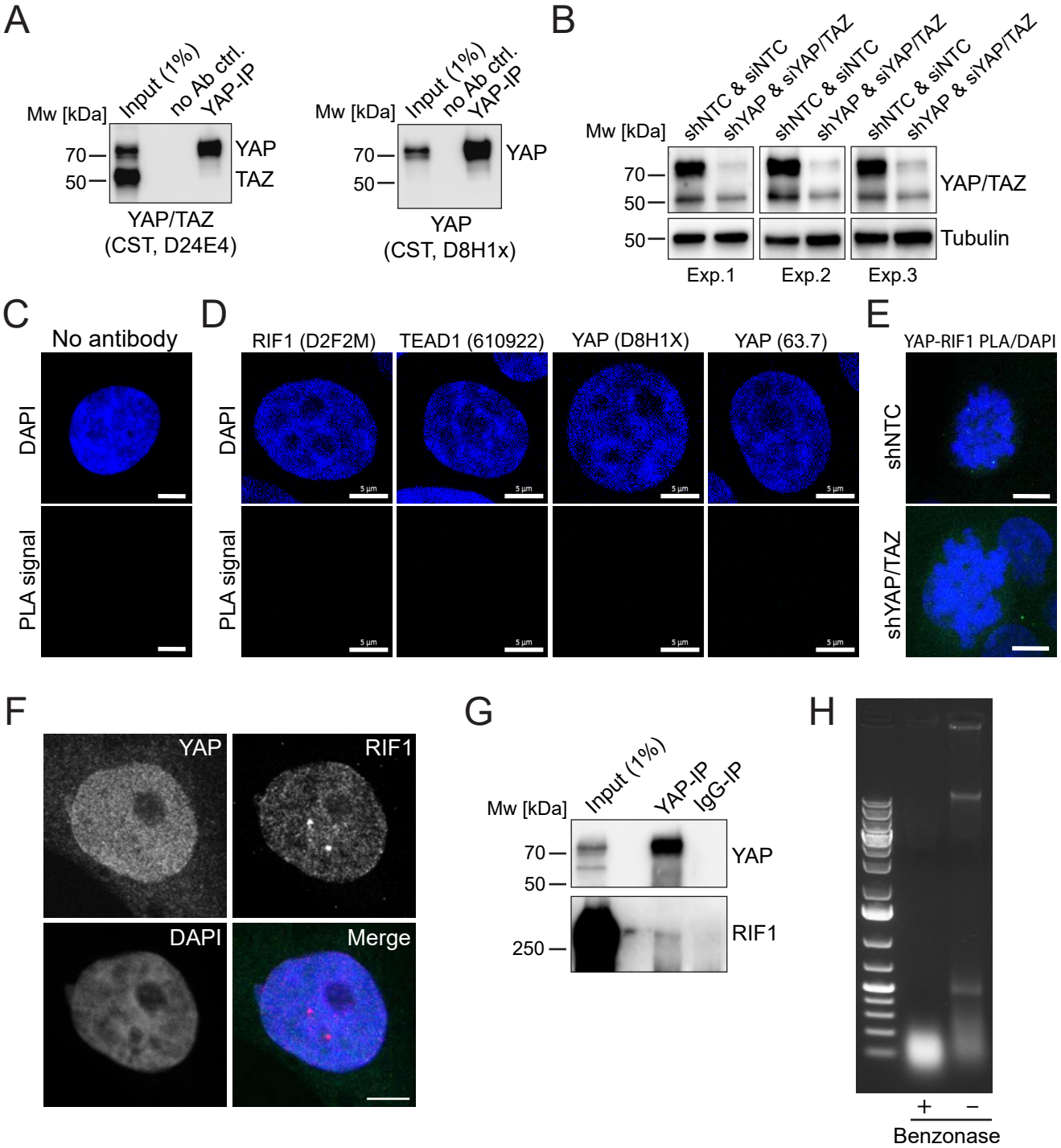

Figure S3_Bojko et al.

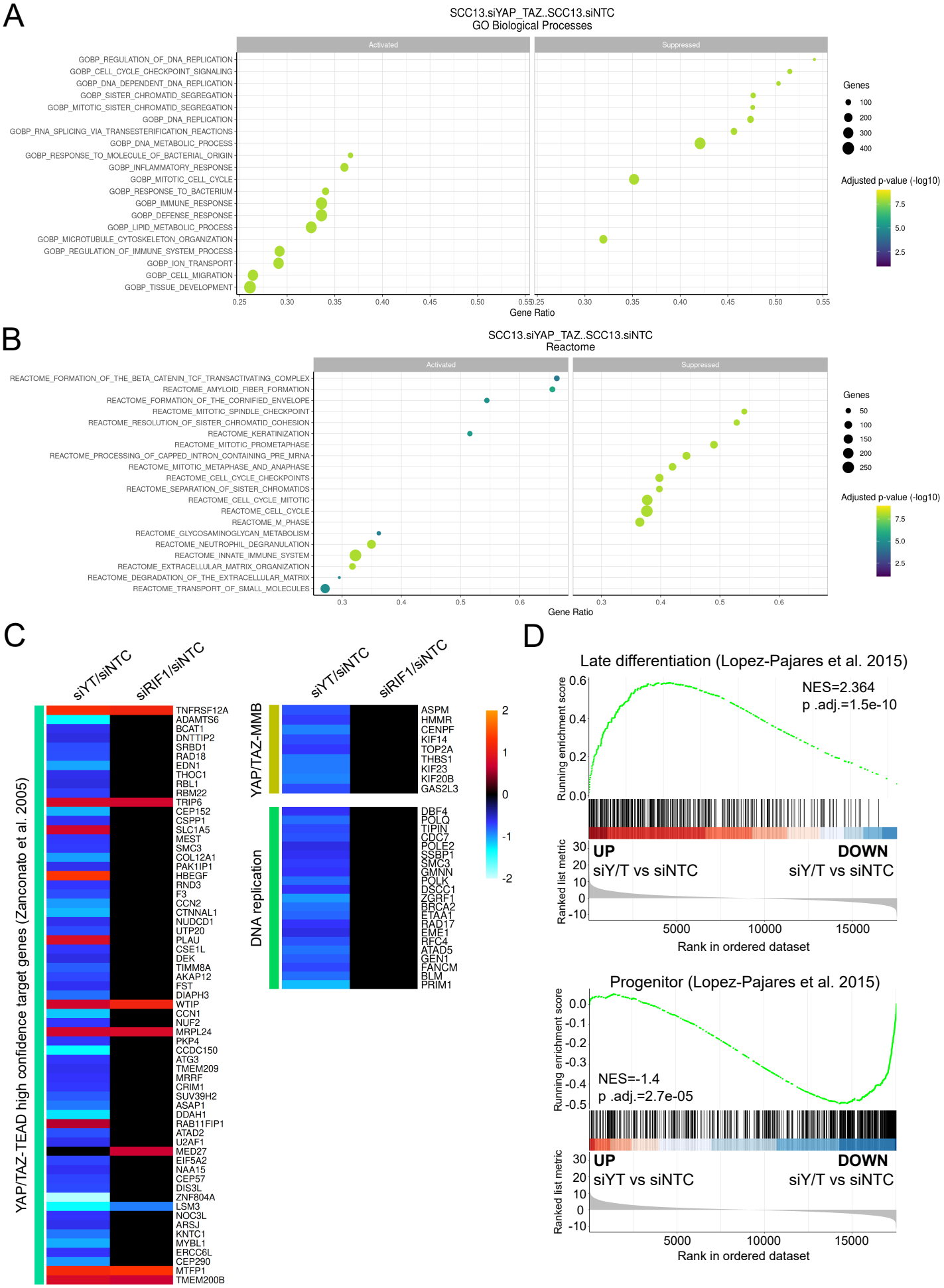

Figure S4_Bojko et al.

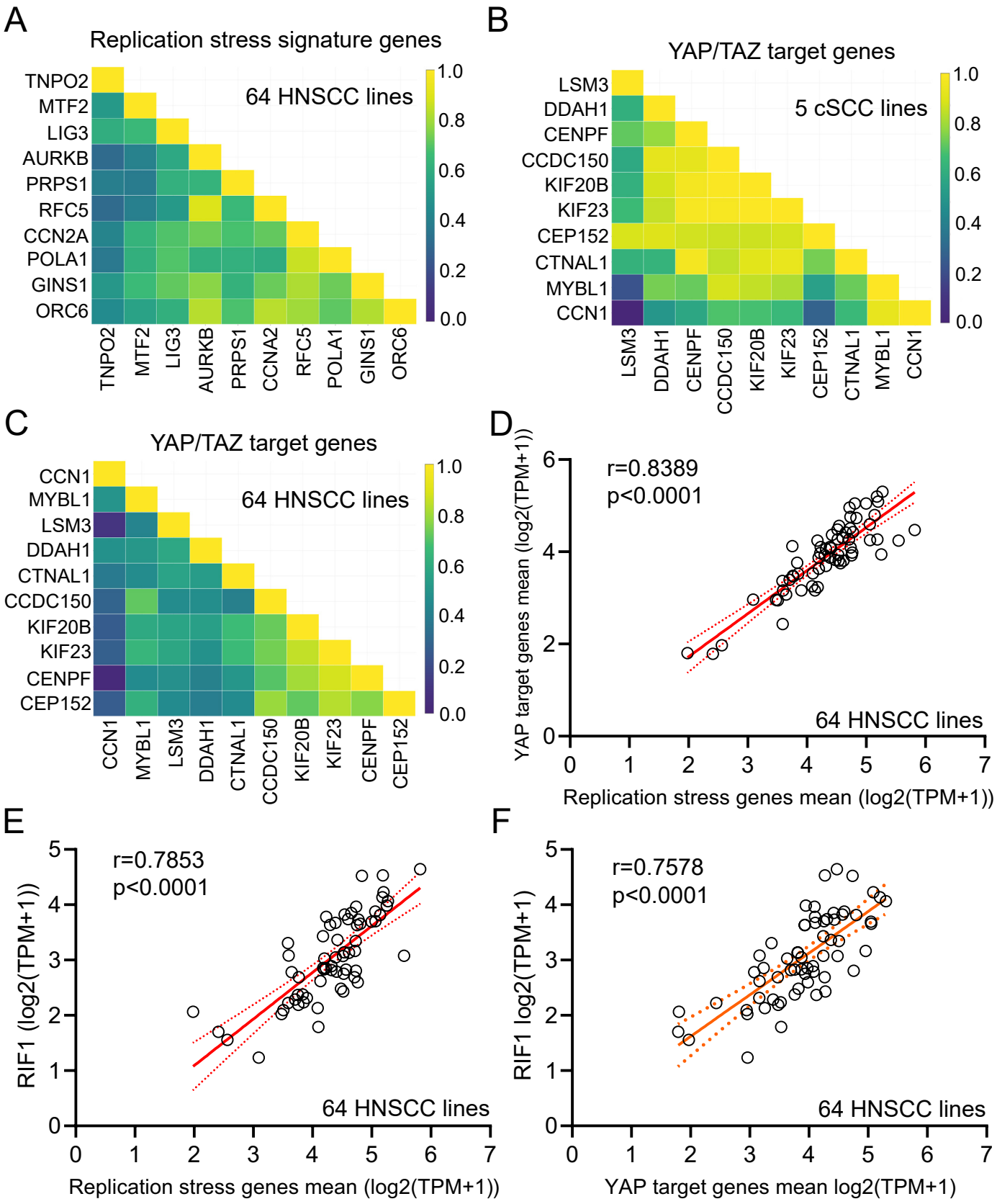

Figure S5_Bojko et al.

A

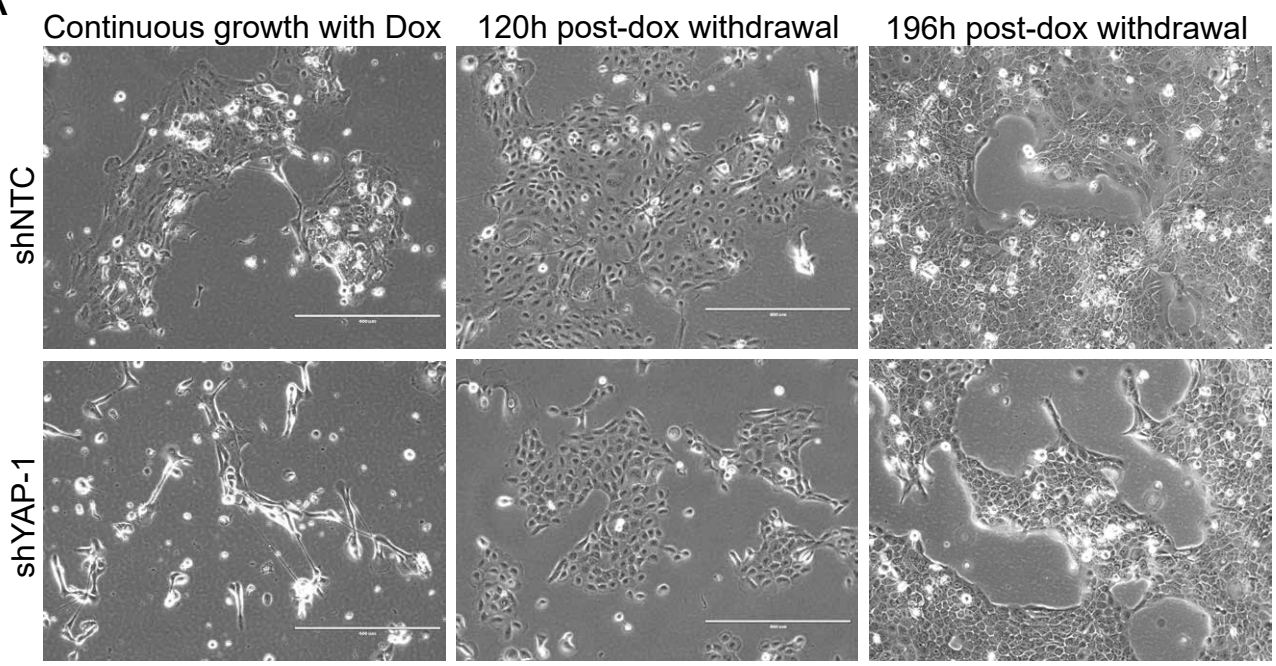

Figure S6_Bojko et al.

A

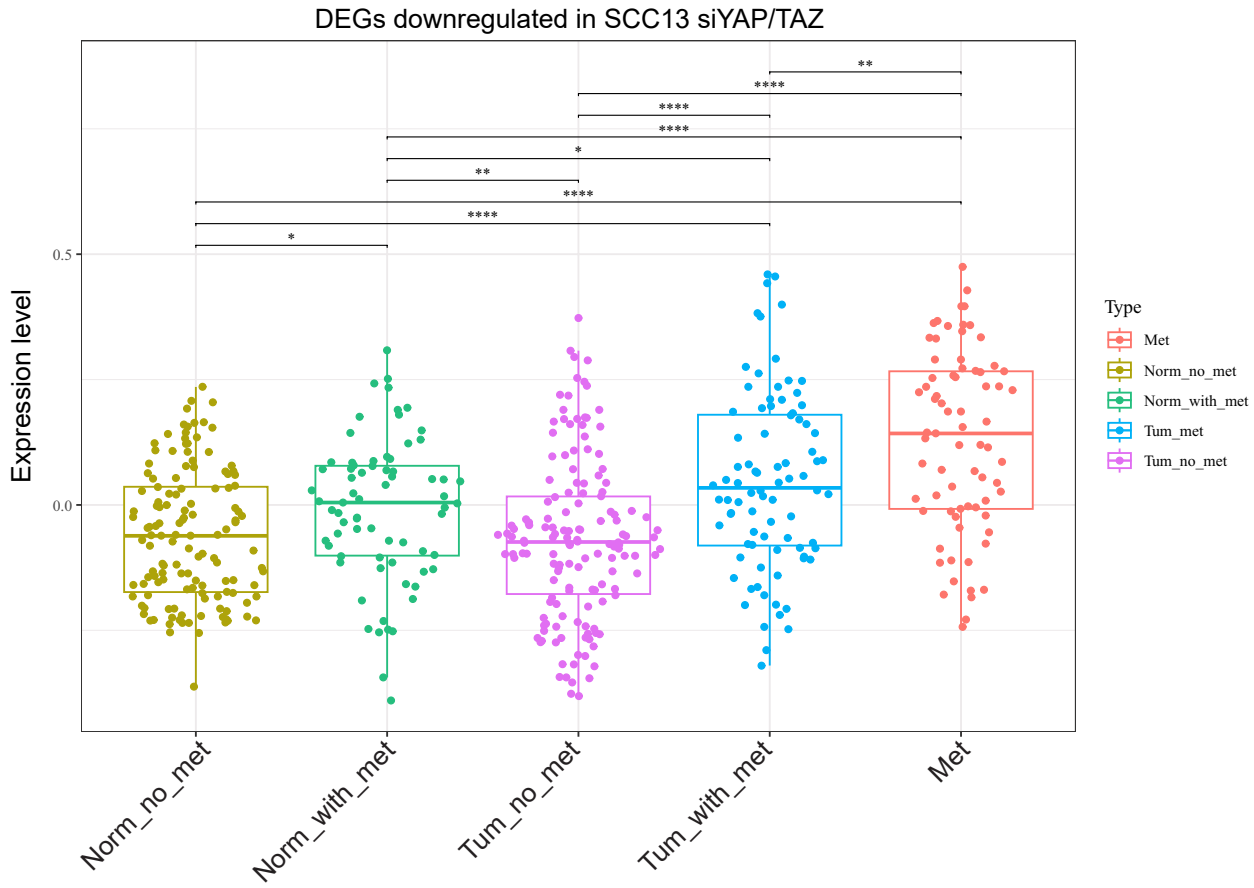

B

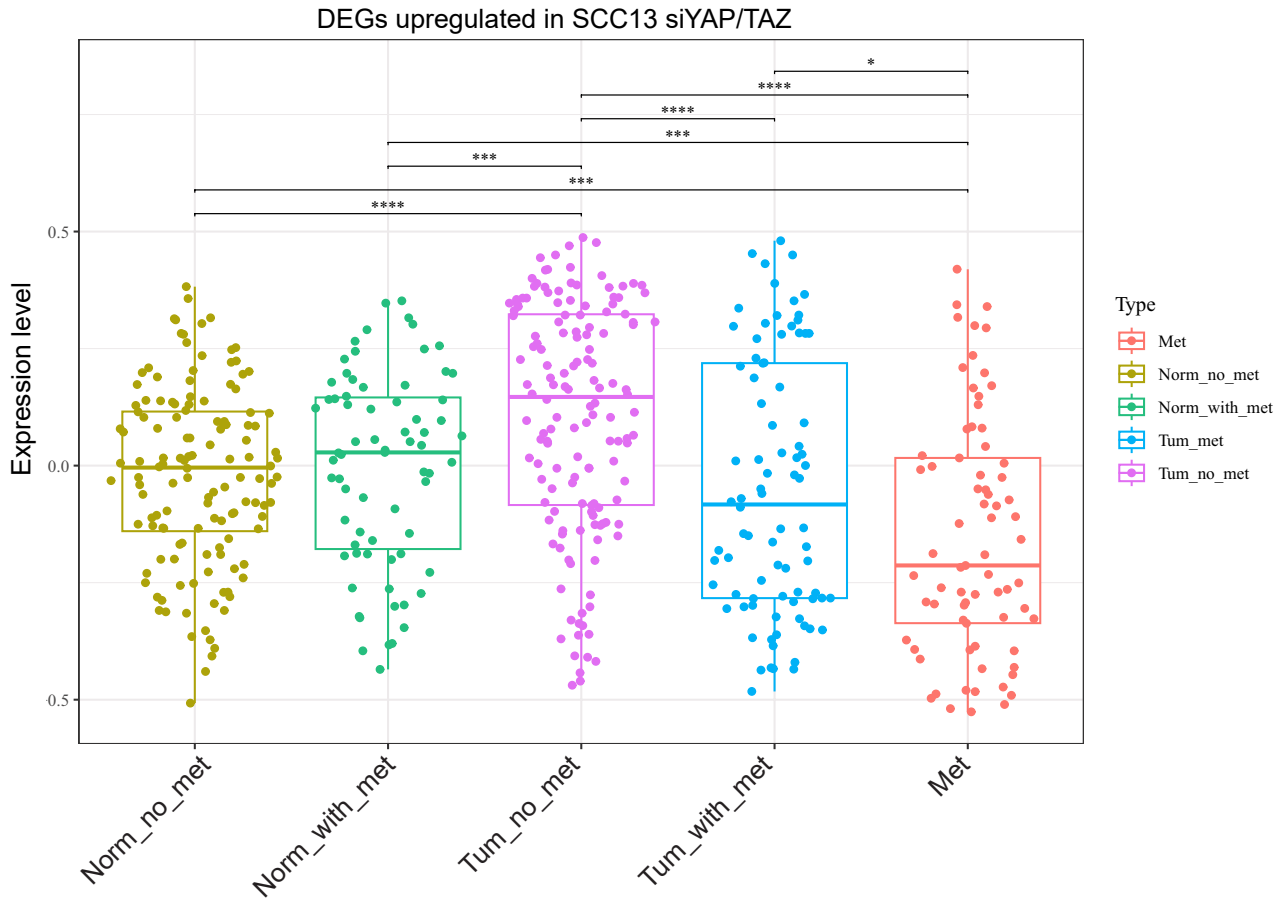

Figure S7_Bojko et al.

A

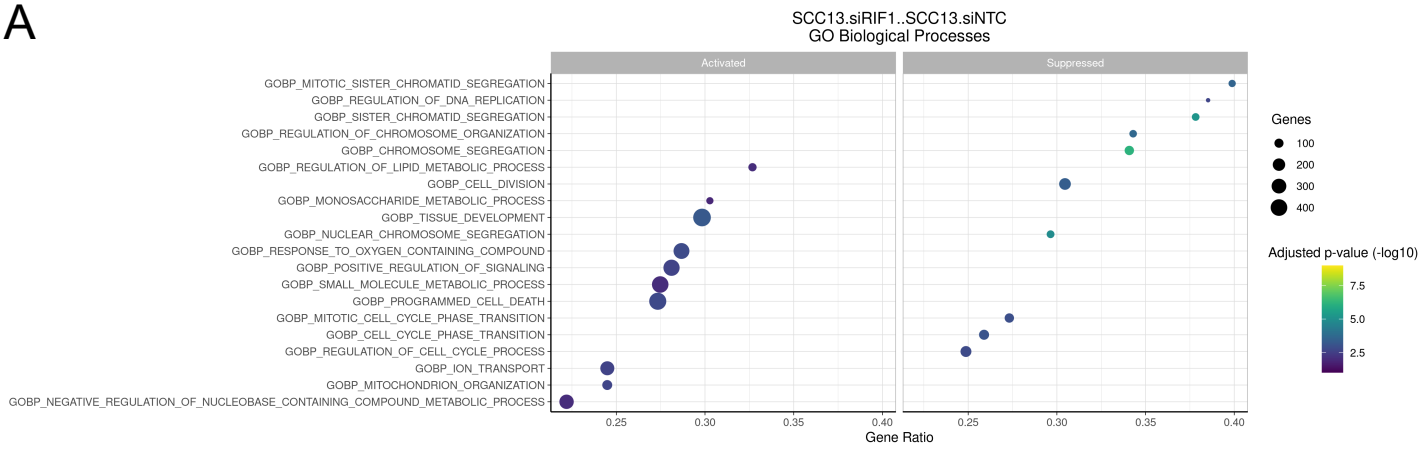

B

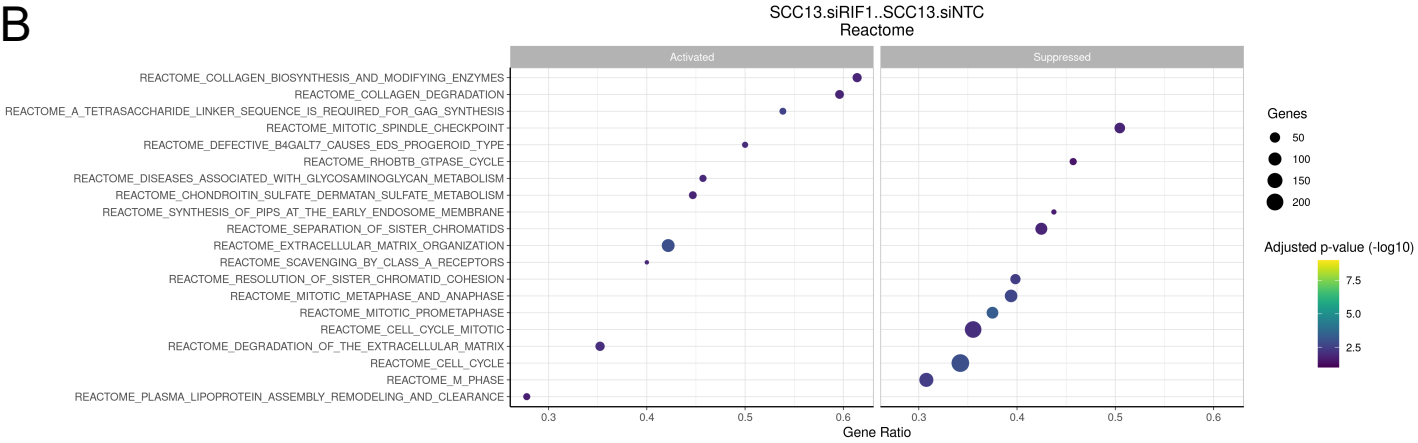

C

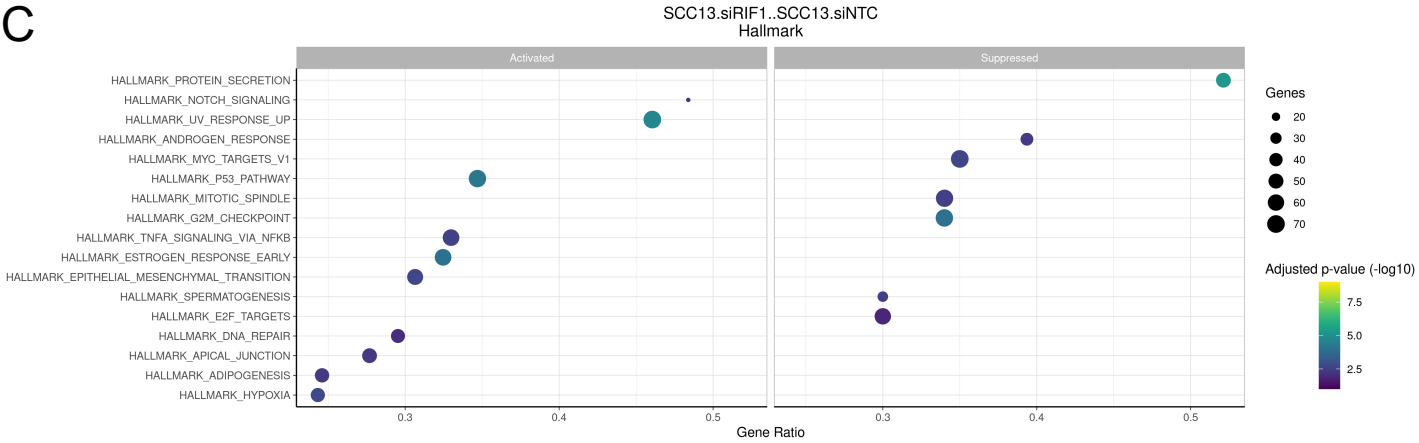

Figure S8_Bojko et al.

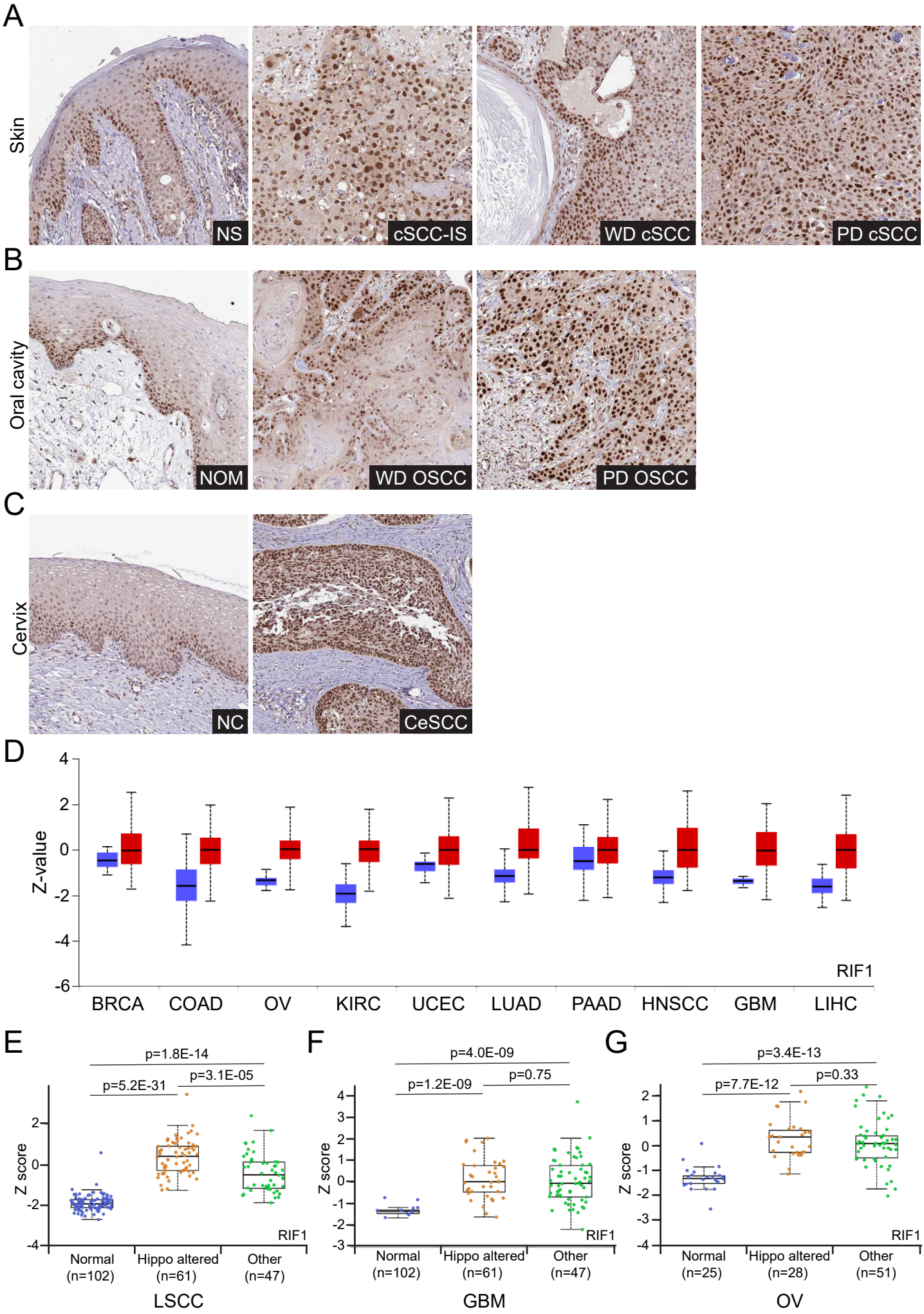

Figure S9_Bojko et al.